

2016-01-01

A Spatially Variant Metamaterial Design Process for Transformation Electromagnetic Devices

Eric Alan Berry

University of Texas at El Paso, eaberry@miners.utep.edu

Follow this and additional works at: https://digitalcommons.utep.edu/open_etd



Part of the [Electrical and Electronics Commons](#)

Recommended Citation

Berry, Eric Alan, "A Spatially Variant Metamaterial Design Process for Transformation Electromagnetic Devices" (2016). *Open Access Theses & Dissertations*. 607.

https://digitalcommons.utep.edu/open_etd/607

This is brought to you for free and open access by DigitalCommons@UTEP. It has been accepted for inclusion in Open Access Theses & Dissertations by an authorized administrator of DigitalCommons@UTEP. For more information, please contact lweber@utep.edu.

A SPATIALLY VARIANT METAMATERIAL DESIGN
PROCESS FOR TRANSFORMATION
ELECTROMAGNETIC
DEVICES

ERIC ALAN BERRY, B.S.E.E.

Doctoral Program in Electrical and Computer Engineering

APPROVED:

Raymond C. Rumpf, Ph.D., Chair

Bryan Usevitch, Ph.D.

Virgilio Gonzalez, Ph.D.

Namsoo Peter Kim, Ph.D.

Charles H. Ambler, Ph.D.

Dean of the Graduate School

Copyright ©

by

Eric Alan Berry

2016

Dedication

To my wife Jenny who has supported me throughout this chapter in our lives.

My children Madeleine, Mateo and Elias who have inspired me to be a better person.

To my mom, brothers, and sister, thank you for believing in me.

My extended family in El Paso, thank you for always cheering me on.

I dedicate my work in memory of my father Coy Berry, who taught me a lot about math and life.

A SPATIALLY VARIANT METAMATERIAL DESIGN
PROCESS FOR TRANSFORMATION
ELECTROMAGNETIC
DEVICES

by

Eric Alan Berry, B.S.E.E.

DISSERTATION

Presented to the Faculty of the Graduate School of

The University of Texas at El Paso

in Partial Fulfillment

of the Requirements

for the Degree of

DOCTOR OF PHILOSOPHY

Doctoral Program in Electrical and Computer Engineering

THE UNIVERSITY OF TEXAS AT EL PASO

December 2016

Acknowledgements

I am very grateful to have a wonderful family that has helped me through this endeavor. My wife, Jenny Berry has always encouraged me to continue my studies. She has given me the support that I needed to successfully finish this chapter in my life. My amazing children Madeleine, Mateo, and Elias have been my inspiration to be a better person. I hope that my achievements also inspire my children to continue learning. A big thanks to my family in El Paso, Chaparral, and Central Texas for their words of encouragement.

I would like to thank my dissertation advisor Dr. Raymond Rumpf for guiding me with his knowledge and expertise. He has taught me so much about my field of research. His patience and dedication to his students is admirable.

Thank you to my defense committee for overseeing my research: Dr. Bryan Usevitch, Dr. Virgilio Gonzalez, Dr. Namsoo Peter Kim, and Dr. Shirley Moore, Ph. D.

I also appreciate my friends and coworkers who have dedicate time to give me advice: Dr. Jay Barton, UTEP, Sandia National Laboratories; Dr. Cesar Garcia, UTEP, Lockheed Martin; Mr. Jose Enriquez, UTEP, *White Sands Missile Range* (WSMR); Mr. Kurt Knox, WSMR; Ms. Sandra Saldivar-Valles, WSMR; Mr. Gustavo Sierra, WSMR; Dr. Bruce Freeman, XL Scientific; and Mr. Dan Treibel, XL Scientific.

Facilities support provided by the following:

The EM Lab at the University of Texas at El Paso

The Survivability, Vulnerability and Assessment Directorate at White Sands Missile Range

Abstract

A technique for the implementation of devices designed using *transformation optics* (TO) is presented using metamaterial elements arranged using spatially variant lattices. A description of transformation optics, including the design of arbitrarily shaped devices by solving Laplace's equation numerically, is discussed. Analysis of a variety of metamaterial unit cells using frequency sweeps of the unit cells with the resulting permittivity and permeability values. Metamaterial unit cells are also analyzed by the scaling of all the features of the metamaterial elements in the unit cell and calculating the permittivity and permeability. *Finite-difference time domain* (FDTD) and *finite-difference frequency domain* (FDFD) methods are described including the simulation of anisotropic structures using FDFD. An arbitrary electromagnetic cloak is given as an example device and is designed using the methods presented within to demonstrate the toolchain.

Table of Contents

Dedication.....	iii
Acknowledgements.....	v
Abstract	vi
Table of Contents.....	vii
List of Figures.....	ix
Chapter 1: Introduction	1
1.1 Purpose.....	1
1.2 Overview	6
Chapter 2: Background Material.....	9
2.1 Maxwell's Equations	9
2.2 Coordinate Transformations.....	12
2.3 Transformation Electromagnetics.....	15
2.4 Metamaterial Parameter Retrieval	17
Chapter 3: The Finite-Difference Time-Domain Method	20
3.1 Introduction	20
3.2 Formulation	20
Chapter 4: Simulation of Anisotropic Devices Using Finite-Difference Frequency-Domain	38
4.1 Formulation	38
4.2 Total-Field/Scattered-Field Formulation	50
4.3 Improved Anisotropic Finite-Difference Frequency-Domain.....	52
Chapter 5: Design of Arbitrary Transformation Optics Devices.....	55
5.1 Introduction	55
5.2 Numerical Grid Generation Using Laplace's Equation	56
5.3 Calculating the Permittivity and Permeability Functions	64
5.4 Benchmark and Examples.....	67
5.5 Conclusions	76
Chapter 6: Synthesis of Spatially Variant Lattices	78
6.1 Purpose.....	78
6.2 Grating Vectors	78
6.3 Spatially Varying Parameters.....	80
6.4 Spatial Harmonics.....	81
6.5 Construction of Lattice	83
6.6 Optimization of the Algorithm.....	85
Chapter 7: Demonstration of Transformation Optics and Spatially Variant Lattice Toolchain	87
7.1 Coordinate Transformation	87
7.2 Material Parameters	89
7.3 Decomposition of Materials to Principal Axes	90

7.4	Metamaterial Mapping.....	95
7.5	Spatially Variant Method for Non-Uniform and Circulating Grids ..	102
7.6	Hybridization of Transformation Optics and Spatially Variant Lattices	106
7.7	Metamaterial Device Simulation.....	110
Chapter 8: Conclusion.....		112
References		114
Vita.....		119

List of Figures

Figure 1.1: Electromagnetic cloak designed by analytical coordinate transformation [1, 17].....	1
Figure 1.2: AFDFD simulation of devices using arbitrarily generated coordinate transformations [19].....	2
Figure 1.3: An electric LC metamaterial unit cell [29].....	3
Figure 1.4: Frequency sweep of ELC metamaterial. The left-hand figure displays the permittivity of the unit cell as a function of frequency and the figure on the right shows the permeability as a function of frequency.	4
Figure 1.5: Scaling of ELC metamaterial. The leftmost figure is an ELC unit cell with a scaling of 0.5, the center unit cell has unity scaling, and the rightmost unit cell has a scaling of 2.	5
Figure 1.6: Permittivity of ELC metamaterial shown in Figure 1.3 for a parameter sweep of scale the unit cell.....	5
Figure 1.7: Spatially variant lattice used to determine the position of a metamaterial unit cell. ...	6
Figure 1.8: Block diagram of TO design process using metamaterials and spatially variant lattices to realize the material parameters of the device.....	6
Figure 2.1: An example of two coordinate systems[38]	12
Figure 2.2: Block diagram for a two-port network. The superscript + signifies an incident voltage wave and the superscript – signifies a reflected wave.	17
Figure 2.3: Dielectric slab of thickness d , relative permittivity ϵ_r , relative permeability μ_r . An incident electromagnetic wave with wave vector \vec{k}_i undergo reflections and transmission which are characterized by scattering parameters.....	18
Figure 3.1: The Yee grid shown in three dimensions [68, 69]	27
Figure 3.2: Total-Field/Scattered-Field Implementation. The figure on the left shows a typical periodic unit cell with PML on the $\pm z$ boundaries, a reflection plane, a transmission plane, periodic boundary conditions on the $\pm x$ and $\pm y$ boundaries, and a TF/SF boundary. The figure on the right shows the effect of the TF/SF boundary on propagating waves as shown in Ref. [63].	35
Figure 4.1: Three dimensional Yee grid showing the placement of the field components within a cell of the computational grid as well as the tensor component locations [17].....	41
Figure 4.2: Simulation time for AFDFD using the impermeability tensor versus the permeability tensor	54
Figure 5.1: (Left) Three-dimensional grid for $U(x, y, z)$. (Right) Two-dimensional grid for $U(x, y, z)$	56
Figure 5.2. Two-dimensional grid to illustrate solution of Laplace’s equation.	60
Figure 5.3. (Left) Physical boundary conditions enclose a portion of the grid. (Right) Solution to Laplace’s equations obtained only in the enclosed portion of the grid.....	61
Figure 5.4. (Left) Matrix equation $\mathbf{L}'\mathbf{u} = \mathbf{b}$ for entire grid. (Middle) Reduced Laplace’s equation.	61
Figure 5.5. Boundary conditions for the coordinate transformation in equations (5.21) and (5.22) . (Left) original coordinate system. (Right) Transformed coordinate system.	63
Figure 5.6. Coordinate transformation boundary value problem shown in Figure 5.5. The figure on the left is the original Cartesian coordinate system within the transformation boundaries. The	

figure on the right is the transformed coordinate system determined using the boundaries shown in Figure 5.5 and defined in Eqs. (5.21) and (5.22).	64
Figure 5.7. Elements composing the Jacobian matrix for the coordinate transformation shown in Figure 5.6.	66
Figure 5.8. Coordinate transformation boundary conditions for a cylindrical cloak.	67
Figure 5.9. Permittivity tensor for cylindrical electromagnetic cloak.	68
Figure 5.10. AFDFD simulation of cylindrical electromagnetic cloak.	69
Figure 5.11. Coordinate transformation for flat transformation optics lens. The figure on the left is the original coordinate space while that on the right is the transformed space.	69
Figure 5.12. Permittivity tensors for flat transformation optics lens. The permeability tensor is identical for a bend based in free space. All tensor components which are not visualized are zero throughout the grid. The material values for this lens are for a grid resolution of $\lambda_0/120$	70
Figure 5.13. AFDFD simulation of flat TO lens.	71
Figure 5.14. Outline of arbitrary electromagnetic cloak and object to be cloaked.	72
Figure 5.15. Permittivity tensor for arbitrary electromagnetic cloak. The permeability tensor is identical for a cloak based in free space. All tensor components which are not visualized are equal to one for the elements along the diagonal and zeros for the off-diagonal elements.	73
Figure 5.16. AFDFD simulation of arbitrary electromagnetic cloak.	74
Figure 5.17. Coordinate transformation for transformation optics bend. The figure on the left is the original coordinate space while that on the right is the transformed space.	75
Figure 5.18. Permittivity tensors for arbitrary electromagnetic bend. The permeability tensor is identical for a bend based in free space. All tensor components which are not visualized are zero throughout the grid.	75
Figure 5.19. AFDFD simulation of TO electromagnetic bend.	76
Figure 6.1: (a) Uniform lattice of periodic unit cells, (b) lattice bent 90° using conventional means, (c) lattice bent using spatially variant lattice synthesis tool [97].	78
Figure 6.2: Summary of spatial variation parameters for a spatially variant grating [97].	81
Figure 6.3: Spatial harmonics for 2D and 3D unit cell arranged in an infinitely periodic lattice [81].	82
Figure 6.4: Effect of number of spatial harmonics in the reconstruction of a unit cell [104]	83
Figure 6.5: Illustration of Gibbs Phenomenon for a continuous time signal. The application to Fourier space is similar [105].	83
Figure 6.6: Graphical representation of method for determining spatially variant lattice grating vectors.	84
Figure 6.7: The left plot of this figure displays the real part of the spatial harmonics for a unit cell. On the right a threshold was set to eliminate all harmonics which exceeded this threshold.	85
Figure 6.8: Spatial harmonics of a unit cell reduced to the minimum number of unique orientations by eliminating all collinear components.	86
Figure 7.1: Boundaries of arbitrary electromagnetic cloak.	87
Figure 7.2: Coordinate axes for the reverse electromagnetic cloak coordinate transformation.	88
Figure 7.3: Derivatives of x and y coordinates calculated using Laplace's equation.	89
Figure 7.4: Arrays of permittivity tensor elements for the arbitrary electromagnetic cloak shown in Figure 7.1. The permeability will be identical to the permittivity.	90
Figure 7.5: Convergence sweep of electromagnetic cloak. A value of $N_{RES} = \Delta x / \lambda_0$ above 100 is seen to be well converged.	91

Figure 7.6: Principal axes and diagonalized permittivity tensor values along principal axes. The permittivity values ε_c in the direction of \hat{c} approach infinity near the center of the cloaking region.....	91
Figure 7.7: Result of AFDFD simulation of the cloak with the material tensors shown in Figure 7.6. This simulation was performed with a grid resolution of $\lambda_0/100$	92
Figure 7.8: Simplified material parameters for metamaterial cloak.	94
Figure 7.9: Cloak constructed using reduced permittivity and permeability values as shown in Figure 7.8 simulated using AFDFD with a grid resolution of $\lambda_0/80$	95
Figure 7.10: MELC unit cell with the dimensions $d = 3.0$ mm , $w = 0.25$ mm , $g = 0.25$ mm , $l = 0.6$ mm , $c = 0.25$ mm . The spacing between structures is $p = 0.25$ mm and the conductor thickness is $t = 0.25$ mm	96
Figure 7.11: Effective material parameter sweeps for the MELC structure shown in Figure 7.10.	97
Figure 7.12: Real part of the material parameters from the scaling sweep for the MELC metamaterial unit cell.....	98
Figure 7.13: Imaginary part of the material parameters from the scaling sweep for the MELC metamaterial unit cell.....	98
Figure 7.14: Plot of the device material parameters with a cursor at the position (0.016,0.048)	99
Figure 7.15: Difference terms for the material values for the position (0.016,0.048) in the device.	99
Figure 7.16: Combined material differences shown on the left. On the right the combined differences are plotted on a logarithmic scale and the minimum scale values are shown with a data cursor.	100
Figure 7.17: Metamaterial mapping for the electromagnetic cloak.....	101
Figure 7.18: AFDFD simulation of electromagnetic cloak with only the real part of the material parameters used.....	101
Figure 7.19: Reduced material model for electromagnetic cloak described in [18]......	102
Figure 7.20: Implementation of the Spatially Variant algorithm on a non-uniform grid.	103
Figure 7.21: Expanded view of a section of the non-uniform grid shown in Figure 7.20.	104
Figure 7.22: Grating vectors derived using spatially variant planar gratings with principal axes as the grating vectors.....	105
Figure 7.23: Sum of the planar gratings shown in Figure 7.22.	106
Figure 7.24: Intersection of planar gratings shown in Figure 7.23 determined using a threshold of 1.0.....	106
Figure 7.25: Cut out of grating intersection grid showing cell grouping.....	107
Figure 7.26: Final cloak designed using transformation optics hybridized with spatially variant metamaterials.....	108
Figure 7.27: Uniform lattice with lattice spacing of MELC element described in Section 7.4.	108
Figure 7.28: Cartesian lattice of metamaterial positions for transformation optics cloak boundaries shown in Figure 7.1.....	109
Figure 7.29: Transformation optics cloak with metamaterial elements arranged according to the Cartesian lattice shown in Figure 7.28.....	110

Figure 7.30: FDTD simulation of cloak shown in Figure 7.26 performed using VSim from Tech-X Corp.	111
Figure 7.31: Discrete element experimental result of cloak designed in Ref. [18]	111

Chapter 1: Introduction

1.1 PURPOSE

Transformation electromagnetics, which is also commonly known as transformation optics (TO), is a technique which allows electromagnetic fields to be sculpted using coordinate transformations that determine how the electric and magnetic fields will bend within a device [1-3]. TO uses the invariance of Maxwell's equations to coordinate transformations to encapsulate all the effects of the coordinate transformations into the material properties of the device itself. TO provides a graphical representation of the behavior of the fields and calculates the material properties that must be used for the fields to behave in the prescribed manner. This level of control over the electromagnetic fields allows devices such as cloaks [4-9], lenses [10, 11], bends [12], beam splitters [2, 13, 14], concentrators [8, 15, 16], and many others [2] to be designed. Figure 1.1 shows the coordinate axes for the famous electromagnetic cloak described by Pendry [1] on the left and the response of the cloak to a wave incident from the left simulated using the *anisotropic finite-difference frequency-domain* (AFDFD) presented in Ref. [17].

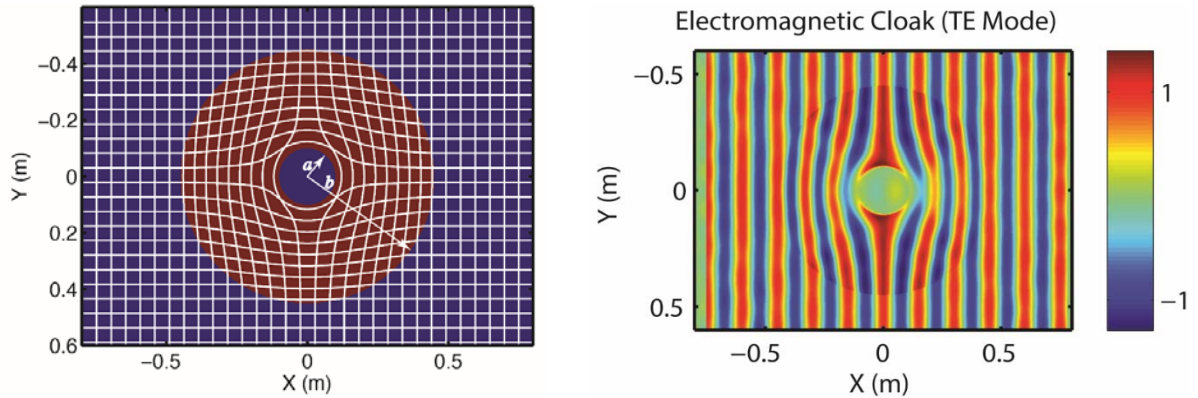


Figure 1.1: Electromagnetic cloak designed by analytical coordinate transformation [1, 17]

The vast majority of devices designed to date using TO have been derived using analytical expressions [2, 18]. These expressions cannot describe the flow of energy through an arbitrary geometry. This research describes a technique to numerically design an arbitrary device using coordinate transformations defined by boundary conditions. A numerically generated coordinate transformation is performed by solving Laplace's equation using the finite-difference method. A

boundary value problem is constructed in which the boundaries of the device in the original coordinate system are replaced by the boundaries in the transformed coordinate system. This technique allows for the coordinates in the transformed system to be calculated [19]. Determining the Jacobian matrix of the resultant coordinate transformation, the anisotropic tensors required to realize the coordinate transformation are solved using the equations of transformation optics [1, 2, 20]. Figure 1.2 displays two devices using transformation optics defined for arbitrary coordinate transformations [19]. The figure on the left is that of an arbitrary electromagnetic bend and that on the right that of an electromagnetic cloak. Both devices were simulated using AFDFD [17]

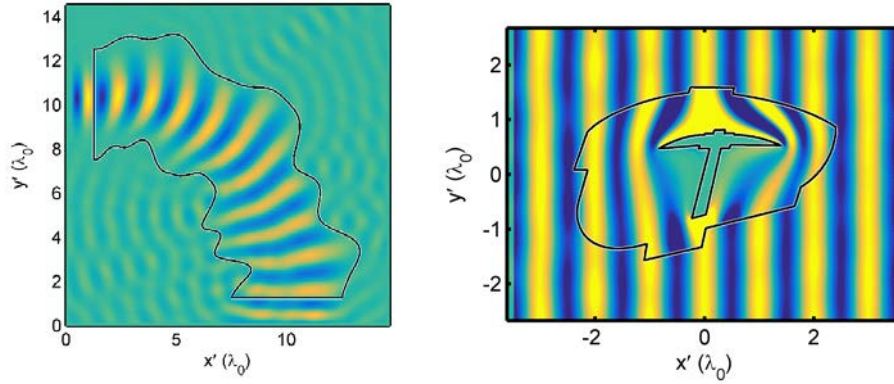


Figure 1.2: AFDFD simulation of devices using arbitrarily generated coordinate transformations [19]

The material tensors which are constructed are generally fully anisotropic tensors [21]. In order to realize such materials it is necessary to determine a coordinate system in which the tensors can be represented as diagonal matrices. The orientation of the coordinate system in which the off-diagonal tensor elements vanish is known as the principal axes of the material [22, 23]. The principal axes of the tensors are determined by solving an eigenvalue problem [22, 24, 25] at every point in the grid. The eigenvalues are the permittivity or permeability in the direction of the eigenvector for that value. The eigenvectors are known as the principal axes of the anisotropic material.

In addition to the materials determined by transformation optics being generally anisotropic, the permittivity and permeability values which are necessary are not achievable using naturally occurring materials [4, 26]. In order to manufacture a device designed using TO, materials must be used which have the same electromagnetic response as that of the material tensors derived from TO. As the values

required for permittivity and permeability vary beyond the limits of materials which are naturally occurring, engineered materials must be considered. The most promising class of materials to provide the desired response are resonant metamaterials [27, 28]. These materials have a very wide range of response, but only in the neighborhood of the resonant frequency. Another concern with this category of metamaterial is that they exhibit high loss near the resonant frequency. Figure 1.3 shows a common metamaterial unit cell known as an *electric LC* (ELC) metamaterial [29] where L represents inductance and C represents capacitance. This metamaterial unit cell was simulated using Ansys HFSS electromagnetic simulation software [30]. The dimensions of the unit cell used for the simulation were $w=0.25$ mm, $g=0.25$ mm, $l=1.0$ mm, $d=3.0$ mm, $t=0.203$ mm, and copper thickness 0.017 mm. The unit cell was cubic with a lattice spacing of $a=3.333$ mm. The effective permittivity and permeability are plotted in Figure 1.4 as a function of frequency.

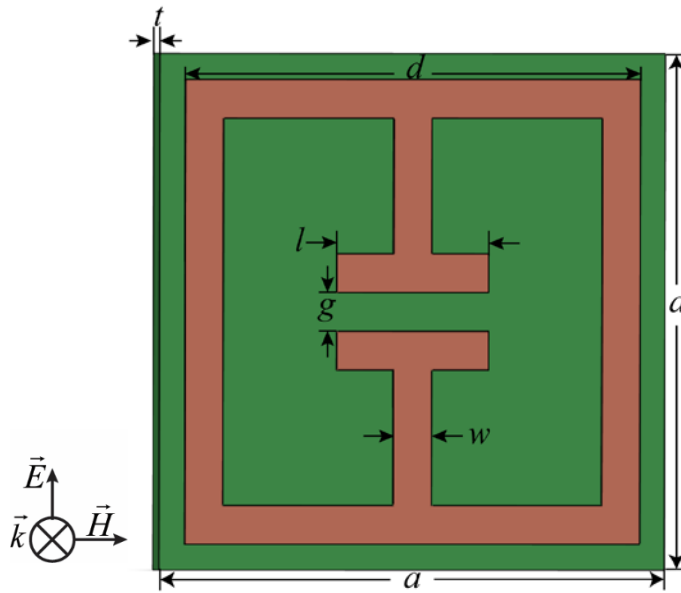


Figure 1.3: An electric LC metamaterial unit cell [29].

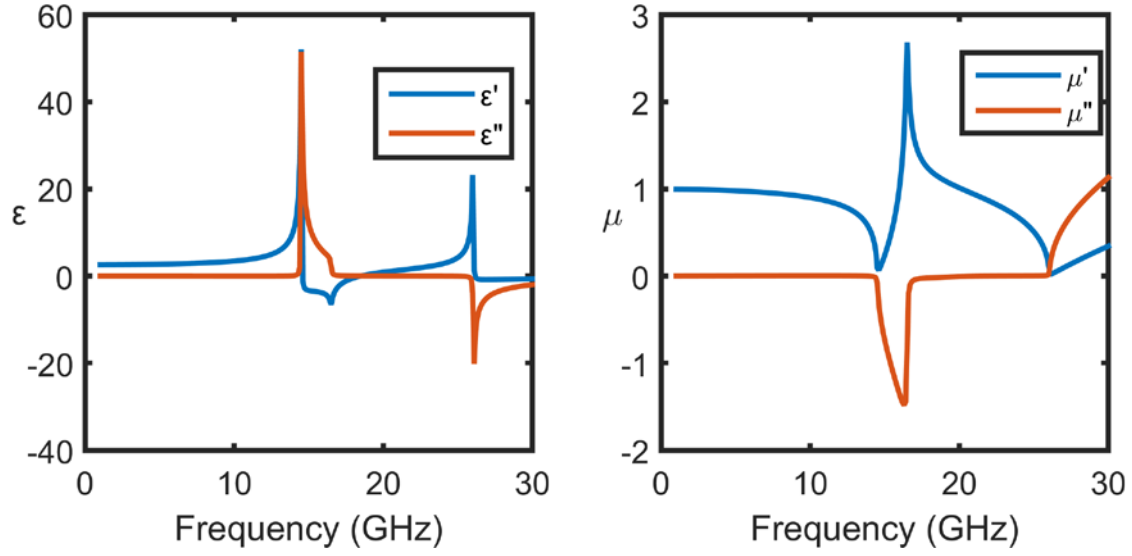


Figure 1.4: Frequency sweep of ELC metamaterial. The left-hand figure displays the permittivity of the unit cell as a function of frequency and the figure on the right shows the permeability as a function of frequency.

A metamaterial mapping is performed by doing a parameter sweep of the scaling of the metamaterial cells at a fixed frequency leading to a parameter space in which the permittivity and permeability values of the unit cells are determined by the physical features of the unit cells. Figure 1.5 displays an ELC metamaterial unit cell which has been scaled by 0.5, 1.0, and 2.0 for the left, center, and right figures respectively. The permittivity sweep of this cell over scale is shown in Figure 1.6 for both the real and imaginary parts of the permittivity.

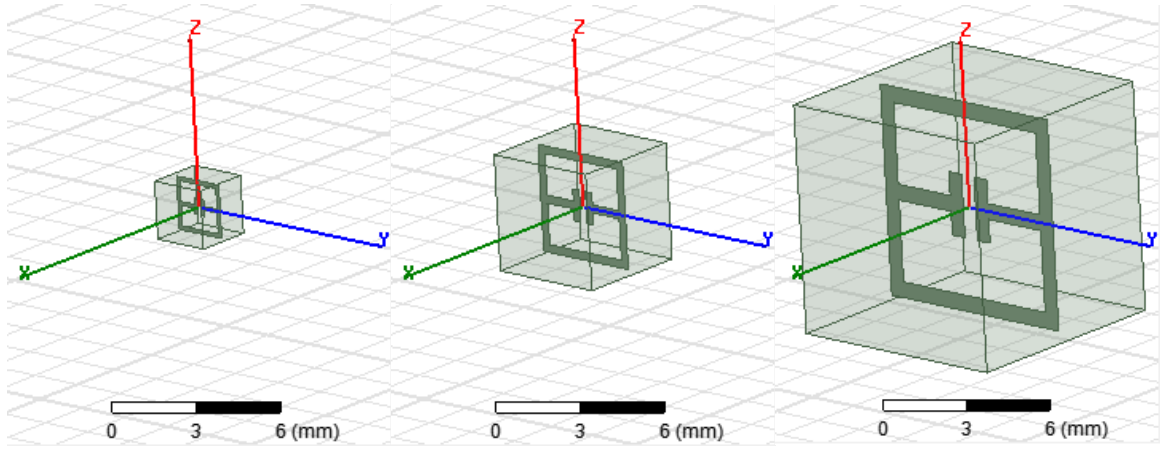


Figure 1.5: Scaling of ELC metamaterial. The leftmost figure is an ELC unit cell with a scaling of 0.5, the center unit cell has unity scaling, and the rightmost unit cell has a scaling of 2.

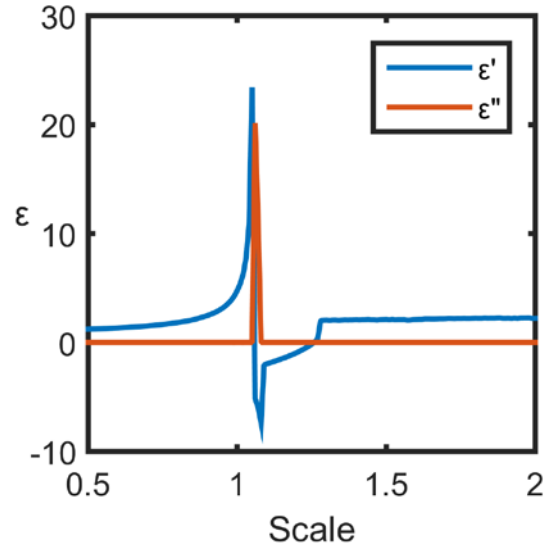


Figure 1.6: Permittivity of ELC metamaterial shown in Figure 1.3 for a parameter sweep of scale the unit cell.

The metamaterials are arranged within the device according to the scaling and orientation which provide the best-fit to the constitutive parameter at that position within the device. A spatially variant lattice, as shown in Figure 1.7, is constructed for each of the material parameters to ensure that the metamaterial cells are positioned and oriented correctly for the electromagnetic response required for the device.

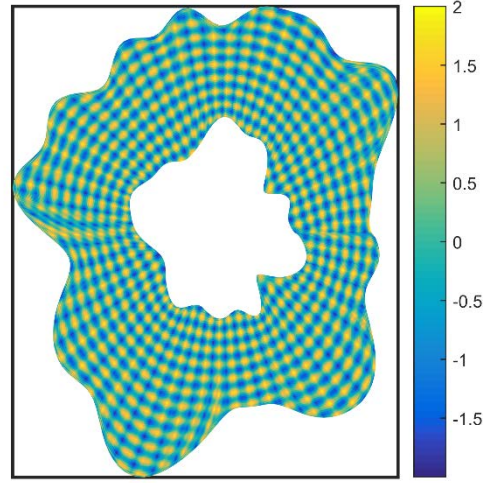


Figure 1.7: Spatially variant lattice used to determine the position of a metamaterial unit cell.

The overall design process is summarized in Figure 1.8. The spatial variation shown in Step 1 is generated by calculating a coordinate transformation based on solving Laplace's equation for an arbitrary boundary value problem. Step 2 is implemented using the equations of TO with the numerically generated coordinate transformation from Step 1. The material tensors derived in Step 2 are assigned to metamaterials based on the response necessary. The proper scaling for the metamaterial is chosen by using a best-fit method to match the effective material properties throughout the device. The metamaterial elements are then placed throughout the device by using a spatially variant lattice to ensure that the arrangement of elements are smooth, continuous, and defect free.

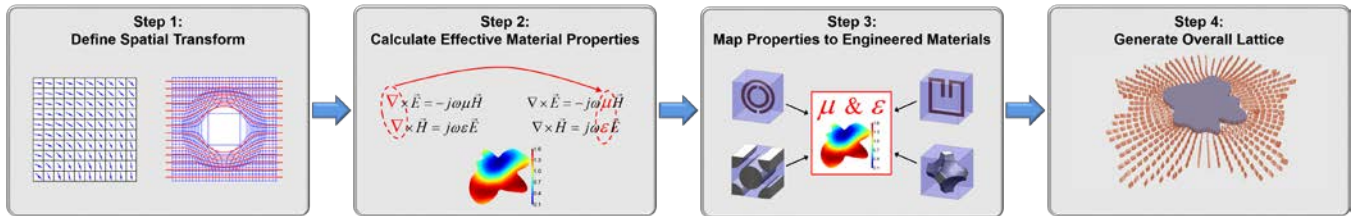


Figure 1.8: Block diagram of TO design process using metamaterials and spatially variant lattices to realize the material parameters of the device.

1.2 OVERVIEW

Chapter 2 provides the fundamentals of electromagnetics to understand the following chapters. A detailed description of Maxwell's equations in anisotropic materials is discussed. The constitutive relations are discussed in detail and the wave equation is derived. Coordinate transformations, in

particular the transformation of vectors, tensors, and linear operators are explained. The theory of transformation electromagnetics is derived by presenting the form invariance of Maxwell's equations and concluding with the equations for calculating the materials necessary to perform the transformation. Finally, a discussion of the retrieval of the electromagnetic material properties of a metamaterial are calculated using the scattering parameters for a metamaterial unit cell.

Chapter 3 provides a detailed description of the *Finite-Difference Time Domain* (FDTD) Method. The method is rigorously derived and the formulation, as applicable to the scope of this research, is provided.

Chapter 4 presents the *Finite-Difference Frequency Domain* (FDFD) simulation algorithm for solving Maxwell's equations with anisotropic materials. A complete derivation is given of the algorithm and a method of implementing Total-Field/Scattered-Field boundaries is given which is simple and intuitive. An improvement to the AFDFD approach of Ref. [17] is presented where the impermeability tensor is created in order to replace the use of the matrix inverse with multiplication of a matrix which is inverted prior to the creation of the wave equation. The two methods are compared and the performance of each is discussed.

Chapter 5 provides a method of designing arbitrary transformation electromagnetic devices by using finite-differences to solve Laplace's equation for a boundary value problem where the boundaries of the original coordinate system are assigned to those of the transformed system. A method of isolating the calculation on Laplace's equation to only the region of consideration is explained to increase computational speed. Creation of the Jacobian matrix for the coordinate transformation is discussed. The calculation of the material tensors derived using transformation optics is presented. Finally, several examples are presented to benchmark and demonstrate the algorithm.

Chapter 6 introduces a method of synthesizing spatially variant lattices. The ability to spatially vary the orientation, period, and fill fraction of a unit cell is discussed. Optimization of this algorithm are also presented which dramatically reduce the computational time required to synthesize a spatially variant lattice.

Chapter 7 presents an in-depth discussion of the device which is simulated to validate the entirety of the tool chain offered in this research. The full toolchain is demonstrated in the implementation of this device. Performance of the device is also discussed and compared between the discrete metamaterial simulation and the effective media model.

Chapter 8 presents the summary of this research effort. Future work and other possible devices are also discussed.

Chapter 2: Background Material

2.1 MAXWELL'S EQUATIONS

Maxwell's equations describe the physical behavior of electromagnetic phenomenon [31]

$$\nabla \cdot \vec{D} = \rho_v \quad (2.1)$$

$$\nabla \cdot \vec{B} = 0 \quad (2.2)$$

$$\nabla \times \vec{E} = -\frac{\partial \vec{B}}{\partial t} \quad (2.3)$$

$$\nabla \times \vec{H} = \vec{J} + \frac{\partial \vec{D}}{\partial t}. \quad (2.4)$$

The quantities in Eqs. (2.1)-(2.4) are the electric flux density, \vec{D} (C/m²), the charge density per unit volume, ρ_v (C/m³), magnetic flux density \vec{B} (Wb/m²), the electric field intensity, \vec{E} (V/m), the magnetic field intensity, \vec{H} (A/m), and the current density, \vec{J} (A/m²).

The time-varying description of electromagnetic fields can be predicted using Maxwell's equation combined with the constitutive relations which describe the effect of materials on electromagnetic fields. The frequency domain representations of Maxwell's equation are

$$\nabla \cdot \vec{D} = \rho_v \quad (2.5)$$

$$\nabla \cdot \vec{B} = 0 \quad (2.6)$$

$$\nabla \times \vec{E} = -j\omega \vec{B} \quad (2.7)$$

$$\nabla \times \vec{H} = \vec{J} + j\omega \vec{D}. \quad (2.8)$$

Maxwell's equations for systems with materials which have a negligible conductivity can omit the current density and charge density terms. Maxwell's equations for charge free space are

$$\nabla \cdot \vec{D} = 0 \quad (2.9)$$

$$\nabla \cdot \vec{B} = 0 \quad (2.10)$$

$$\nabla \times \vec{E} = -j\omega \vec{B} \quad (2.11)$$

$$\nabla \times \vec{H} = j\omega \vec{D}. \quad (2.12)$$

2.1.1 Constitutive Relations

The constitutive relations relate the electric displacement field \vec{D} to the electric field intensity \vec{E} and the magnetic induction field \vec{B} to the magnetic field intensity \vec{H} as shown below

$$\vec{D}(t) = \epsilon_0 [\epsilon_r(t)] * \vec{E}(t) \quad (2.13)$$

$$\vec{B}(t) = \mu_0 [\mu_r(t)] * \vec{H}(t) \quad (2.14)$$

$$\vec{J}(t) = [\sigma(t)] * \vec{E}(t). \quad (2.15)$$

Where the square brackets denote tensor quantities and the asterisk denotes convolution.

The permittivity of free space ϵ_0 and the permeability of free space μ_0 are both constants which are derived from the speed of light in vacuum as

$$c_0 = \frac{1}{\sqrt{\mu_0 \epsilon_0}} = 299,792,458 \text{ (m/s)} \quad (2.16)$$

$$\mu_0 = 4\pi \times 10^{-7} \text{ (H/m)}. \quad (2.17)$$

With both c_0 and μ_0 defined exactly [32] the value of ϵ_0 can be calculated from Eq. (2.16) to be

$$\epsilon_0 = 8.854187817... \times 10^{-12} \text{ (F/m)}. \quad (2.18)$$

As the relative permittivity ϵ_r , the permeability μ_r , and the conductivity σ can be nonlinear, anisotropic, and dispersive it is much easier to work with the frequency domain representation of Eqs. (2.13) and (2.14) to reduce complexity by replacing convolution in the time domain with multiplication in the frequency domain giving

$$\vec{D}(\omega) = \epsilon_0 [\epsilon_r(\omega)] \vec{E}(\omega) \quad (2.19)$$

$$\vec{B}(\omega) = \mu_0 [\mu_r(\omega)] \vec{H}(\omega) \quad (2.20)$$

$$\vec{J}(\omega) = [\sigma(\omega)] \vec{E}(\omega). \quad (2.21)$$

The quantities \vec{D} , \vec{B} , \vec{E} and \vec{H} are vector quantities which can be expressed in Cartesian coordinates as

$$\vec{D} = D_x \hat{x} + D_y \hat{y} + D_z \hat{z} \quad (2.22)$$

and similarly for the other terms. The terms \hat{x} , \hat{y} , and \hat{z} are the unit vectors of the coordinate system.

Permittivity

The permittivity of a material is the measure of the ability of an electric field to polarize a material. In general, the permittivity is a tensor quantity expressed in Cartesian coordinates as [33]

$$[\epsilon_r] = \begin{bmatrix} \epsilon_{xx} & \epsilon_{xy} & \epsilon_{xz} \\ \epsilon_{yx} & \epsilon_{yy} & \epsilon_{yz} \\ \epsilon_{zx} & \epsilon_{zy} & \epsilon_{zz} \end{bmatrix}. \quad (2.23)$$

Rewriting Eq. (2.19) as a system of equations using Eqs. (2.22) and (2.23) leads to

$$\begin{aligned}
D_x &= \varepsilon_0 (\varepsilon_{xx} E_x + \varepsilon_{xy} E_y + \varepsilon_{xz} E_z) \\
D_y &= \varepsilon_0 (\varepsilon_{yx} E_x + \varepsilon_{yy} E_y + \varepsilon_{yz} E_z) \\
D_z &= \varepsilon_0 (\varepsilon_{zx} E_x + \varepsilon_{zy} E_y + \varepsilon_{zz} E_z)
\end{aligned} \tag{2.24}$$

Equation (2.24) shows that the direction of the fields D_x , D_y , and D_z may be different than that of the applied field \vec{E} if the material permittivity is anisotropic.

Permeability

The permeability of a material is the measure of the ability of a magnetic field to magnetize a material. The permeability tensor in Cartesian coordinates is [33]

$$[\mu_r] = \begin{bmatrix} \mu_{xx} & \mu_{xy} & \mu_{xz} \\ \mu_{yx} & \mu_{yy} & \mu_{yz} \\ \mu_{zx} & \mu_{zy} & \mu_{zz} \end{bmatrix} \tag{2.25}$$

Similar to Eq.(2.24), Eq. (2.20) can be written as

$$\begin{aligned}
B_x &= \mu_0 (\mu_{xx} H_x + \mu_{xy} H_y + \mu_{xz} H_z) \\
B_y &= \mu_0 (\mu_{yx} H_x + \mu_{yy} H_y + \mu_{yz} H_z) \\
B_z &= \mu_0 (\mu_{zx} H_x + \mu_{zy} H_y + \mu_{zz} H_z)
\end{aligned} \tag{2.26}$$

2.1.2 Wave Equation

Perhaps the most profound result of Maxwell's equations is that they predict electromagnetic waves and in fact were used to conclude that light radiates as electromagnetic waves [34]. Rewriting Eqs. (2.11) and (2.12) including the constitutive relations Eqs. (2.19) and (2.20) leads to

$$\nabla \times \vec{E} = -j\omega\mu_0 [\mu_r] \vec{H} \tag{2.27}$$

$$\nabla \times \vec{H} = j\omega\varepsilon_0 [\varepsilon_r] \vec{E}. \tag{2.28}$$

Solving Eq. (2.27) for \vec{H} yields

$$\vec{H} = -\frac{1}{j\omega\mu_0} [\mu_r]^{-1} (\nabla \times \vec{E}). \tag{2.29}$$

Substituting Eq. (2.29) into Eq. (2.28) leads to

$$\nabla \times \left(-\frac{1}{j\omega\mu_0} [\mu_r]^{-1} (\nabla \times \vec{E}) \right) = j\omega\varepsilon_0 [\varepsilon_r] \vec{E} \tag{2.30}$$

which when simplified becomes

$$\nabla \times \left([\mu_r]^{-1} (\nabla \times \vec{E}) \right) - \frac{\omega^2}{c_0^2} [\epsilon_r] \vec{E} = 0. \quad (2.31)$$

Using the relations $\omega = 2\pi f$, $\lambda_0 = c_0 / f$, and $k_0 = 2\pi / \lambda_0$ equation (2.31) becomes

$$\nabla \times \left([\mu_r]^{-1} (\nabla \times \vec{E}) \right) - k_0^2 [\epsilon_r] \vec{E} = 0. \quad (2.32)$$

The equation (2.32) is the wave equation for the electric field in anisotropic media [35], which is also known as the Helmholtz equation [36].

2.2 COORDINATE TRANSFORMATIONS

2.2.1 Coordinate Transformation

A coordinate transformation is a mapping from one coordinate system to another [37, 38].

Consider the two coordinate systems shown in Figure 2.1. In order to map the coordinate system shown on the left side of the figure to that on the right, a mapping must be used such as

$$\vec{r} = T(\vec{r}') \quad (2.33)$$

which maps the coordinate system defined as

$$\vec{r} = x\hat{x} + y\hat{y} + z\hat{z} \quad (2.34)$$

to the coordinate system

$$\vec{r}' = x'\hat{x}' + y'\hat{y}' + z'\hat{z}'. \quad (2.35)$$

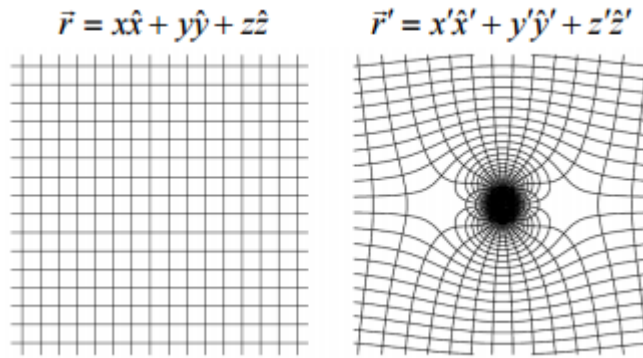


Figure 2.1: An example of two coordinate systems[38]

This mapping is specific to the coordinate systems being transformed. As an example, to map a Cartesian coordinate system to a cylindrical coordinate system, the following equations are used

$$\begin{aligned}
\rho &= \sqrt{x^2 + y^2} \\
\phi &= \tan^{-1} \left(\frac{y}{x} \right) . \\
z &= z
\end{aligned} \tag{2.36}$$

The coordinate transformation for cylindrical coordinates to Cartesian coordinates is given by

$$\begin{aligned}
x &= \rho \cos \phi \\
y &= \rho \sin \phi . \\
z &= z
\end{aligned} \tag{2.37}$$

Another example is the coordinate transformation from Cartesian coordinates to spherical coordinates which is defined as

$$\begin{aligned}
x &= r \sin \theta \cos \phi \\
y &= r \sin \theta \sin \phi . \\
z &= r \cos \theta
\end{aligned} \tag{2.38}$$

The transformation from spherical coordinates to Cartesian coordinates is given by

$$\begin{aligned}
r &= \sqrt{x^2 + y^2 + z^2} \\
\theta &= \cos^{-1} \left(\frac{z}{\sqrt{x^2 + y^2 + z^2}} \right) . \\
\phi &= \tan^{-1} \left(\frac{y}{x} \right)
\end{aligned} \tag{2.39}$$

2.2.2 Jacobian Matrix

In order transform a vector quantity, function, or tensor from one coordinate system to another, a quantity known as the Jacobian matrix must be used [39]. The Jacobian matrix is

$$[\Lambda] = \begin{bmatrix} \frac{h'_1}{h_1} \frac{\partial x'_1}{\partial x_1} & \frac{h'_1}{h_2} \frac{\partial x'_1}{\partial x_2} & \frac{h'_1}{h_3} \frac{\partial x'_1}{\partial x_3} \\ \frac{h'_2}{h_1} \frac{\partial x'_2}{\partial x_1} & \frac{h'_2}{h_2} \frac{\partial x'_2}{\partial x_2} & \frac{h'_2}{h_3} \frac{\partial x'_2}{\partial x_3} \\ \frac{h'_3}{h_1} \frac{\partial x'_3}{\partial x_1} & \frac{h'_3}{h_2} \frac{\partial x'_3}{\partial x_2} & \frac{h'_3}{h_3} \frac{\partial x'_3}{\partial x_3} \end{bmatrix} = \frac{h'_i}{h_j} \frac{\partial x'_i}{\partial x_j} \tag{2.40}$$

for $i, j = 1, 2, 3$ where x'_i are the coordinates in the transformed system, x_j are the coordinates in the original system, h'_i are the scale factors in the transformed system, and h_j are the scale factors in the original system.

The scale factors h'_i and h_j are defined by the specific orthogonal coordinate system [36] and are given as [40]

$$h_j = \sqrt{\sum_{k=1}^3 \left(\frac{\partial x_k}{\partial x'_j} \right)^2}. \quad (2.41)$$

These terms are necessary for any expressions requiring line, surface, or volume differential elements. For the Cartesian coordinate system, the coordinates are $x_i = \{x, y, z\}$ scale factors are $h_i = \{1, 1, 1\}$ and the squared differential arc length is

$$ds^2 = dx^2 + dy^2 + dz^2. \quad (2.42)$$

For the polar cylindrical system of coordinates, $x_i = \{\rho, \phi, z\}$, the coordinate transformation to Cartesian coordinates is

$$\begin{aligned} x &= \rho \cos \phi \\ y &= \rho \sin \phi \\ z &= z \end{aligned} \quad (2.43)$$

and the scale factors are $h_i = \{1, \rho, 1\}$ giving a squared differential arc length of

$$ds^2 = d\rho^2 + \rho^2 d\phi^2 + dz^2. \quad (2.44)$$

2.2.3 Tensors

A tensor quantity is defined by its rank and how it undergoes a coordinate transformation. The rank of a tensor determines how many terms are required to define that tensor. For three dimensional space a rank n tensor has 3^n terms [36]. A tensors of rank 1 is a vector and is transformed according to [41]

$$T'_i = \sum_{j=1}^3 \Lambda_{ij} T_j = \Lambda_{ij} T_j \quad (2.45)$$

for $i, j = 1, 2, 3$. In Eq. (2.45) a notation referred to as Einstein summation notation [42] is used in which all repeated indices are summed over. Rank 2 tensors are generally expressed as 3×3 matrices, which are transformed as

$$T'_{ij} = \Lambda_{ik} \Lambda_{jl} T_{kl} \quad (2.46)$$

for $i, j, k, l = 1, 2, 3$. Expressed in matrix form, equation (2.46) can be written

$$\mathbf{T}' = \mathbf{\Lambda} \mathbf{T} \mathbf{\Lambda}^T. \quad (2.47)$$

In general, a rank n tensor can be transformed by

$$T'_{i,j,k,\dots} = \Lambda_{il}\Lambda_{jm}\Lambda_{kn}\dots T_{lmn\dots} \quad (2.48)$$

Finally, another concept which is used frequently is that of tensor density [43-45] or pseudotensors [36]. A tensor density is a tensor which transforms as in Eq. (2.48), but which is changed by an inversion transformation [46]. These tensors are classified according to a term referred to as weight. Ordinary tensors which transform according to Eq. (2.48) are of weight 0. The transformation of Eq. (2.48) can be further generalized to tensor densities of weight w using [43, 47]

$$T'_{i,j,k,\dots} = |\det(\Lambda)|^{-w} \Lambda_{il}\Lambda_{jm}\Lambda_{kn}\dots T_{lmn\dots} \quad (2.49)$$

2.3 TRANSFORMATION ELECTROMAGNETICS

2.3.1 Form Invariance of Maxwell's Equations

From Eqs. (2.27) and (2.28), Maxwell's curl equations are

$$\nabla \times \vec{E} = -j\omega\mu_0 [\mu_r] \vec{H} \quad (2.50)$$

$$\nabla \times \vec{H} = j\omega\varepsilon_0 [\varepsilon_r] \vec{E}. \quad (2.51)$$

According to [20] and the transformation of vectors in Eq. (2.45), the electric field intensity transforms from the original coordinate system x_i to the transformed coordinate system x'_i by

$$\begin{bmatrix} E_{x_1} \\ E_{x_2} \\ E_{x_3} \end{bmatrix} = \begin{bmatrix} \frac{h'_1}{h_1} \frac{\partial x'_1}{\partial x_1} & \frac{h'_2}{h_1} \frac{\partial x'_2}{\partial x_1} & \frac{h'_3}{h_1} \frac{\partial x'_3}{\partial x_1} \\ \frac{h'_1}{h_2} \frac{\partial x'_1}{\partial x_2} & \frac{h'_2}{h_2} \frac{\partial x'_2}{\partial x_2} & \frac{h'_3}{h_2} \frac{\partial x'_3}{\partial x_2} \\ \frac{h'_1}{h_3} \frac{\partial x'_1}{\partial x_3} & \frac{h'_2}{h_3} \frac{\partial x'_2}{\partial x_3} & \frac{h'_3}{h_3} \frac{\partial x'_3}{\partial x_3} \end{bmatrix} \begin{bmatrix} E_{x'_1} \\ E_{x'_2} \\ E_{x'_3} \end{bmatrix} \quad (2.52)$$

which can be written in vector notation as

$$\vec{E} = [\Lambda]^T \vec{E}' \quad (2.53)$$

and similarly for the magnetic field intensity

$$\vec{H} = [\Lambda]^T \vec{H}'. \quad (2.54)$$

The material tensors $[\varepsilon_r]$ and $[\mu_r]$ transform as weight +1 tensor densities [48] using the transformation equation Eq. (2.49)

$$[\varepsilon_r]' = |\det(\Lambda)|^{-1} [\Lambda][\varepsilon_r][\Lambda]^T \quad (2.55)$$

$$[\mu_r]' = \det(\Lambda)^{-1} [\Lambda][\mu_r][\Lambda]^T. \quad (2.56)$$

Solving Eqs. (2.55) and (2.56) for $[\varepsilon_r]$ and $[\mu_r]$ gives

$$[\varepsilon_r] = \det(\Lambda) \left\{ [\Lambda]^{-1} [\varepsilon_r]' ([\Lambda]^T)^{-1} \right\} \quad (2.57)$$

$$[\mu_r] = \det(\Lambda) \left\{ [\Lambda]^{-1} [\mu_r]' ([\Lambda]^T)^{-1} \right\}. \quad (2.58)$$

Substituting Eqs. (2.53), (2.54), (2.57), and (2.58) into Eqs. (2.50) and (2.51) leads to

$$\nabla \times [\Lambda]^T \vec{E}' = -j\omega\mu_0 \det(\Lambda)^{-1} \left\{ [\Lambda]^{-1} [\mu_r]' ([\Lambda]^T)^{-1} \right\} [\Lambda]^T \vec{H}' \quad (2.59)$$

$$\nabla \times [\Lambda]^T \vec{H}' = j\omega\varepsilon_0 \det(\Lambda)^{-1} \left\{ [\Lambda]^{-1} [\varepsilon_r]' ([\Lambda]^T)^{-1} \right\} [\Lambda]^T \vec{E}' \quad (2.60)$$

which can be further simplified to

$$\frac{[\Lambda](\nabla \times)[\Lambda]^T}{\det(\Lambda)} \vec{E}' = -j\omega\mu_0 [\mu_r]' \vec{H}' \quad (2.61)$$

$$\frac{[\Lambda](\nabla \times)[\Lambda]^T}{\det(\Lambda)} \vec{H}' = j\omega\varepsilon_0 [\varepsilon_r]' \vec{E}'. \quad (2.62)$$

The curl operator can be transformed as

$$\nabla' \times = \frac{\Lambda(\nabla \times)\Lambda^T}{\det(\Lambda)}. \quad (2.63)$$

Replacing the curl transformation in Eqs. (2.61) and (2.62) with Eq. (2.63) yields

$$\nabla' \times \vec{E}' = -j\omega\mu_0 [\mu_r]' \vec{H}' \quad (2.64)$$

$$\nabla' \times \vec{H}' = j\omega\varepsilon_0 [\varepsilon_r]' \vec{E}'. \quad (2.65)$$

Comparing Eqs. (2.64) and (2.65) with Eqs. (2.50) and (2.51) shows that Maxwell's equations maintain the same form regardless of the coordinate system.

2.3.2 Derivation of Transformation Media

From the results derived in the previous section the materials necessary to implement the effects of a coordinate transformation on the electromagnetic fields within a device can be calculated using [1, 2]

$$[\varepsilon_r]' = \frac{[\Lambda][\varepsilon_r][\Lambda]^T}{\det(\Lambda)} \quad (2.66)$$

$$[\mu_r]' = \frac{[\Lambda][\mu_r][\Lambda]^T}{\det(\Lambda)} . \quad (2.67)$$

These tensors are in general anisotropic and rotated from their principal axes to yield tensors with Hermitian symmetry [49].

2.4 METAMATERIAL PARAMETER RETRIEVAL

2.4.1 Scattering Parameters

Scattering parameters are a method of classifying an electromagnetic device or network [50] at its ports without any knowledge of the internal components of the device or network. Figure 2.2 shows a two port device.

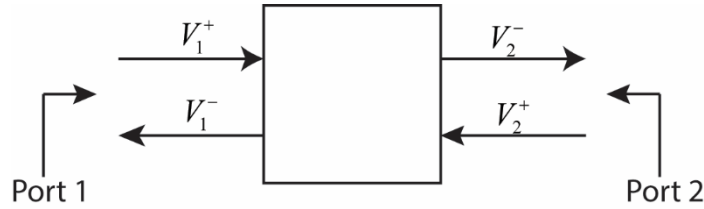


Figure 2.2: Block diagram for a two-port network. The superscript + signifies an incident voltage wave and the superscript – signifies a reflected wave.

For a two-port device as shown in Figure 2.2 the following equation can be written

$$\begin{bmatrix} V_1^- \\ V_2^- \end{bmatrix} = \begin{bmatrix} S_{11} & S_{12} \\ S_{21} & S_{22} \end{bmatrix} \begin{bmatrix} V_1^+ \\ V_2^+ \end{bmatrix}. \quad (2.68)$$

The terms in the scattering matrix are defined according to [50]

$$S_{ij} = \frac{V_i^-}{V_j^+} \bigg|_{V_k^+ = 0 \text{ for } k \neq j}. \quad (2.69)$$

Scattering matrices are also used to characterize the response of a structure to radiated electromagnetic waves as well. Consider the dielectric slab shown in Figure 2.3. The reflection coefficient of the slab at the left most interface is [51]

$$r = \frac{\eta - \eta_0}{\eta + \eta_0} \quad (2.70)$$

where the wave impedance of the slab is given by

$$\eta = \sqrt{\frac{\mu_0 \mu_r}{\epsilon_0 \epsilon_r}} \quad (2.71)$$

and the free space wave impedance is

$$\eta_0 = \sqrt{\frac{\mu_0}{\epsilon_0}} \approx 120\pi. \quad (2.72)$$

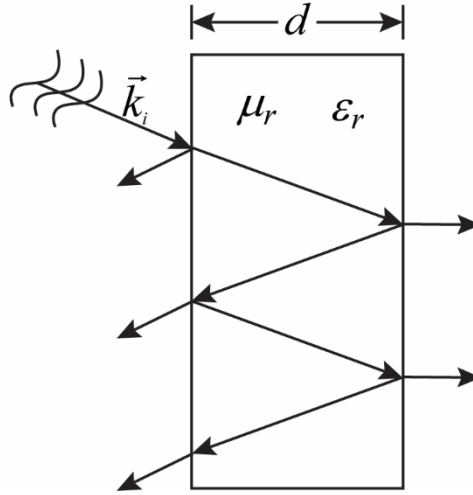


Figure 2.3: Dielectric slab of thickness d , relative permittivity ϵ_r , relative permeability μ_r . An incident electromagnetic wave with wave vector \vec{k}_i undergo reflections and transmission which are characterized by scattering parameters.

The transmission coefficient of the slab is [51]

$$t = \exp(jk_0 nd). \quad (2.73)$$

The scattering parameters for the dielectric slab are

$$S_{11} = \frac{(1-t^2)r}{1-r^2t^2} \quad (2.74)$$

$$S_{21} = \frac{(1-r^2)t}{1-r^2t^2}. \quad (2.75)$$

$$S_{12} = S_{21} \quad (2.76)$$

$$S_{22} = S_{11} \quad (2.77)$$

Expressing the wave impedance and transmission coefficient in terms of the scattering parameters leads to [51, 52]

$$\eta = \pm \sqrt{\frac{(1+S_{11})^2 - S_{21}^2}{(1-S_{11})^2 - S_{21}^2}} \quad (2.78)$$

$$t = \exp(jk_0 nd) = \frac{S_{21}}{1 - S_{11} \frac{\eta - 1}{\eta + 1}}. \quad (2.79)$$

The choice of sign is important to ensure that the wave impedance [51, 52] and that the index of refraction [52] correspond to a passive medium. The conditions determining the signs are given by

$$\eta' \geq 0 \quad (2.80)$$

$$n'' \geq 0 \quad (2.81)$$

where η' is the real part of the wave impedance and n'' is the imaginary part of the refractive index.

Solving for n from Eq. (2.79) leads to

$$n = \frac{1}{k_0 d} \left\{ \left[\text{Im} \left[\ln \left(e^{jk_0 nd} \right) \right] + 2\pi m \right] - j \left[\text{Re} \left[\ln \left(e^{jk_0 nd} \right) \right] \right] \right\}. \quad (2.82)$$

Due to the nature of inverting a complex exponential the expression given in Eq. (2.82) has a periodicity given by integer multiples of 2π . The ambiguity of this periodic function necessitates solving for the correct branch. The wave propagating through a media is periodic therefore the phase at any time is somewhat arbitrary. The periodicity of this phase leads to there being multiple possible solutions to the material properties corresponding to the multiple branches given by (2.82) [51, 52]. The permittivity and permeability defined in terms of refractive index and wave impedance are

$$\epsilon_r = \frac{n}{\eta} \quad (2.83)$$

$$\mu_r = n\eta. \quad (2.84)$$

For a passive material, the imaginary part of both the permittivity and permeability must be greater than zero. Writing the imaginary part of these terms [51, 52]

$$\epsilon_r'' = \frac{1}{|\eta|^2} (\text{Im}(n)\text{Re}(\eta) - \text{Re}(n)\text{Im}(\eta)) \quad (2.85)$$

$$\mu_r'' = \text{Re}(n)\text{Im}(\eta) + \text{Im}(n)\text{Re}(\eta). \quad (2.86)$$

The condition for which both Eqs. (2.85) and (2.86) are greater than zero is given by

$$|\text{Re}(n)\text{Im}(\eta)| \leq \text{Im}(n)\text{Re}(\eta). \quad (2.87)$$

Chapter 3: The Finite-Difference Time-Domain Method

3.1 INTRODUCTION

The *Finite Difference Time Domain* (FDTD) method is a powerful simulation tool which solves Maxwell's equations in time domain form. Common applications of FDTD are metamaterial characterization [53], antenna design [54, 55], lens design [56-58], and plasma physics simulations [59-61]. FDTD allows for transient wave propagation to be modeled therefore it is very useful for modeling devices which exhibit a wideband response.

3.2 FORMULATION

3.2.1 Maxwell's Equations

Maxwell's equations in time domain for a charge free space are

$$\nabla \cdot \vec{D} = 0 \quad (3.1)$$

$$\nabla \cdot \vec{B} = 0 \quad (3.2)$$

$$\nabla \times \vec{E} = -\frac{\partial \vec{B}}{\partial t} \quad (3.3)$$

$$\nabla \times \vec{H} = \frac{\partial \vec{D}}{\partial t}. \quad (3.4)$$

The constitutive relations are given by

$$\vec{D} = [\varepsilon] \vec{E} \quad (3.5)$$

$$\vec{B} = [\mu] \vec{H} \quad (3.6)$$

where $[\varepsilon] = \varepsilon_0 [\varepsilon_r]$ is the permittivity tensor and $[\mu] = \mu_0 [\mu_r]$ is the permeability tensor. Although the FDTD method can be used for generally anisotropic media, for the purposes of this dissertation only materials exhibiting diagonal anisotropy must be considered.

3.2.2 Normalization of Electric Field Intensity

In order to reduce the effect of truncation and rounding error [62] due to the difference in magnitude between the electric field intensity \vec{E} and magnetic field intensity \vec{H} one of the values must be normalized to be of the same order of magnitude as the other. As the decision as to which field should be normalized is arbitrary, the electric field intensity vector is normalized in this dissertation.

The value used to normalize \vec{E} is the wave impedance of free space η_0 which relates \vec{E} and \vec{H} according to

$$\eta_0 = \frac{|\vec{E}|}{|\vec{H}|}. \quad (3.7)$$

The normalized electric field intensity can be expressed as

$$\vec{\tilde{E}} = \frac{\vec{E}}{\eta_0}. \quad (3.8)$$

The electric flux density vector \vec{D} is also normalized according to Ref. [63] as

$$\vec{\tilde{D}} = c_0 \vec{D} \quad (3.9)$$

leading to the relationship

$$\vec{\tilde{D}} = \epsilon_r \vec{\tilde{E}}. \quad (3.10)$$

A further consideration is made for the magnetic flux density \vec{B} and magnetic field intensity \vec{H} in order to place Eq. (3.6) in a form similar to (3.10) such that

$$\vec{B} = \mu_r \vec{H}. \quad (3.11)$$

Substituting Eqs. (3.8) and (3.9) into Eqs. (3.3) and (3.4) leads to

$$\nabla \times \vec{\tilde{E}} = -\frac{1}{c_0} \frac{\partial \vec{B}}{\partial t} \quad (3.12)$$

$$\nabla \times \vec{H} = \frac{1}{c_0} \frac{\partial \vec{\tilde{D}}}{\partial t} \quad (3.13)$$

where the curl term in Eq. (3.12) is altered in order to implement Eq. (3.11)

Expanding the normalized curl expressions (3.12) and (3.13) into their vector components leads to

$$\frac{\partial \tilde{E}_z}{\partial y} - \frac{\partial \tilde{E}_y}{\partial z} = -\frac{1}{c_0} \frac{\partial B_x}{\partial t} \quad (3.14)$$

$$\frac{\partial \tilde{E}_z}{\partial x} - \frac{\partial \tilde{E}_x}{\partial z} = -\frac{1}{c_0} \frac{\partial B_y}{\partial t} \quad (3.15)$$

$$\frac{\partial \tilde{E}_y}{\partial x} - \frac{\partial \tilde{E}_x}{\partial y} = -\frac{1}{c_0} \frac{\partial B_z}{\partial t} \quad (3.16)$$

for Eq. (3.3) and

$$\frac{\partial H_z}{\partial y} - \frac{\partial H_y}{\partial z} = -\frac{1}{c_0} \frac{\partial \tilde{D}_x}{\partial t} \quad (3.17)$$

$$\frac{\partial H_z}{\partial x} - \frac{\partial H_x}{\partial z} = -\frac{1}{c_0} \frac{\partial \tilde{D}_y}{\partial t} \quad (3.18)$$

$$\frac{\partial H_y}{\partial x} - \frac{\partial H_x}{\partial y} = -\frac{1}{c_0} \frac{\partial \tilde{D}_z}{\partial t} \quad (3.19)$$

for Eq. (3.4). The constitutive relations can be expanded into components according to

$$\tilde{D}_x = \varepsilon_{xx} \tilde{E}_x \quad (3.20)$$

$$\tilde{D}_y = \varepsilon_{yy} \tilde{E}_y \quad (3.21)$$

$$\tilde{D}_z = \varepsilon_{zz} \tilde{E}_z \quad (3.22)$$

and

$$H_x = \mu_{xx} H_x \quad (3.23)$$

$$H_y = \mu_{yy} H_y \quad (3.24)$$

$$H_z = \mu_{zz} H_z. \quad (3.25)$$

3.2.3 Perfectly Matched Layers

To simulate many devices, it is essential that the electromagnetic energy reaching the boundary of the computational grid be prevented from scattering back into the computational domain. A common approach to this problem is to use the *Uniaxial Perfectly Matched Layer* (UPML) [64-66]. To implement the UPML, a layer of material with loss is placed at the boundaries where the wave is desired to be absorbed. The material must be such that the impedance is matched to eliminate reflections while still providing loss [67]. This is done by introducing the concept of complex permittivity and permeability according to

$$\tilde{\varepsilon}_r = \varepsilon'_r + j\varepsilon''_r \quad (3.26)$$

$$\tilde{\mu}_r = \mu'_r + j\mu''_r. \quad (3.27)$$

While the loss introduced into the boundary region with complex material parameters effectively absorbs the wave, it does so at a single frequency, angle of incidence, and polarization [67]. By using anisotropic materials the absorption can be extended to encompass all polarizations, angles of incidence, and frequencies. In order to account for waves traveling in any direction the PML tensors are defined as

$$[s_x] = \begin{bmatrix} s_x^{-1} & 0 & 0 \\ 0 & s_x & 0 \\ 0 & 0 & s_x \end{bmatrix} \quad (3.28)$$

$$[s_y] = \begin{bmatrix} s_y & 0 & 0 \\ 0 & s_y^{-1} & 0 \\ 0 & 0 & s_y \end{bmatrix} \quad (3.29)$$

$$[s_z] = \begin{bmatrix} s_z & 0 & 0 \\ 0 & s_z & 0 \\ 0 & 0 & s_z^{-1} \end{bmatrix}. \quad (3.30)$$

A combined PML tensor can be made according to

$$[s] = [s_x][s_y][s_z] = \begin{bmatrix} \frac{s_y s_z}{s_x} & 0 & 0 \\ 0 & \frac{s_x s_z}{s_y} & 0 \\ 0 & 0 & \frac{s_x s_y}{s_z} \end{bmatrix} \quad (3.31)$$

where the elements of Eq. (3.31) are given as

$$s_x(x) = 1 + \frac{\sigma'_x(x)}{j\omega\epsilon_0} \quad (3.32)$$

$$s_y(y) = 1 + \frac{\sigma'_y(y)}{j\omega\epsilon_0} \quad (3.33)$$

$$s_z(z) = 1 + \frac{\sigma'_z(z)}{j\omega\epsilon_0} \quad (3.34)$$

and the conductivity terms are defined according to

$$\sigma'_x(x) = \frac{\epsilon_0}{2\Delta t} \left(\frac{x}{L_x} \right)^3 \quad (3.35)$$

$$\sigma'_y(y) = \frac{\epsilon_0}{2\Delta t} \left(\frac{y}{L_y} \right)^3 \quad (3.36)$$

$$\sigma'_z(z) = \frac{\epsilon_0}{2\Delta t} \left(\frac{z}{L_z} \right)^3 \quad (3.37)$$

where Δt is the time step interval to be defined later and L_i is the PML depth in the i direction.

3.2.4 Incorporation of PML into Maxwell's Equations

Maxwell's equations must be written using their frequency domain representation to more easily implement the PML from the previous section. Maxwell's equations and the constitutive relations in frequency domain are given by

$$\nabla \times \vec{\tilde{E}}(\omega) = -\frac{j\omega}{c_0} [s] \vec{\tilde{B}}(\omega) \quad (3.38)$$

$$\nabla \times \vec{\tilde{H}}(\omega) = \eta_0 [\sigma] \vec{\tilde{E}}(\omega) + \frac{j\omega}{c_0} [s] \vec{\tilde{D}}(\omega) \quad (3.39)$$

$$\vec{\tilde{D}}(\omega) = [\varepsilon_r] \vec{\tilde{E}}(\omega) \quad (3.40)$$

$$\vec{\tilde{B}}(\omega) = [\mu_r] \vec{\tilde{H}}(\omega) \quad (3.41)$$

where the current density term \vec{J} is implemented using the relation

$$\vec{J} = [\sigma] \vec{E} \quad (3.42)$$

where σ is the conductivity tensor given by

$$[\sigma] = \begin{bmatrix} \sigma_{xx} & \sigma_{xy} & \sigma_{xz} \\ \sigma_{yx} & \sigma_{yy} & \sigma_{yz} \\ \sigma_{zx} & \sigma_{zy} & \sigma_{zz} \end{bmatrix}. \quad (3.43)$$

For a diagonally anisotropic conductivity tensor this becomes

$$[\sigma] = \begin{bmatrix} \sigma_{xx} & 0 & 0 \\ 0 & \sigma_{yy} & 0 \\ 0 & 0 & \sigma_{zz} \end{bmatrix} \quad (3.44)$$

Normalizing the current density vector \vec{J} with the normalized electric field intensity $\vec{\tilde{E}}$ leads to

$$\vec{\tilde{J}} = \eta_0 [\sigma] \vec{\tilde{E}}. \quad (3.45)$$

Writing Maxwell's curl equations (3.38) and (3.39) for each component yields

$$\frac{\partial \tilde{E}_z(\omega)}{\partial y} - \frac{\partial \tilde{E}_y(\omega)}{\partial z} = -\frac{j\omega}{c_0} \frac{s_y s_z}{s_x} B_x(\omega) \quad (3.46)$$

$$\frac{\partial \tilde{E}_x(\omega)}{\partial z} - \frac{\partial \tilde{E}_z(\omega)}{\partial x} = -\frac{j\omega}{c_0} \frac{s_x s_z}{s_y} B_y(\omega) \quad (3.47)$$

$$\frac{\partial \tilde{E}_y(\omega)}{\partial x} - \frac{\partial \tilde{E}_x(\omega)}{\partial y} = -\frac{j\omega}{c_0} \frac{s_x s_y}{s_z} B_z(\omega) \quad (3.48)$$

$$\frac{\partial H_z(\omega)}{\partial y} - \frac{\partial H_y(\omega)}{\partial z} = \eta_0 \sigma_{xx} \tilde{E}_x(\omega) + \frac{j\omega}{c_0} \frac{s_y s_z}{s_x} \tilde{D}_x(\omega) \quad (3.49)$$

$$\frac{\partial H_x(\omega)}{\partial z} - \frac{\partial H_z(\omega)}{\partial x} = \eta_0 \sigma_{yy} \tilde{E}_y(\omega) + \frac{j\omega}{c_0} \frac{s_x s_z}{s_y} \tilde{D}_y(\omega) \quad (3.50)$$

$$\frac{\partial H_y(\omega)}{\partial x} - \frac{\partial H_x(\omega)}{\partial y} = \eta_0 \sigma_{zz} \tilde{E}_z(\omega) + \frac{j\omega}{c_0} \frac{s_x s_y}{s_z} \tilde{D}_z(\omega). \quad (3.51)$$

The constitutive relations in Eqs. (3.40) and (3.41) become

$$\tilde{D}_x(\omega) = \varepsilon_{xx} \tilde{E}_x(\omega) \quad (3.52)$$

$$\tilde{D}_y(\omega) = \varepsilon_{yy} \tilde{E}_y(\omega) \quad (3.53)$$

$$\tilde{D}_z(\omega) = \varepsilon_{zz} \tilde{E}_z(\omega) \quad (3.54)$$

$$B_x(\omega) = \mu_{xx} H_x(\omega) \quad (3.55)$$

$$B_y(\omega) = \mu_{yy} H_y(\omega) \quad (3.56)$$

$$B_z(\omega) = \mu_{zz} H_z(\omega). \quad (3.57)$$

Substituting Eqs. (3.32) - (3.34) into Eqs. (3.46) - (3.51) gives

$$\frac{\partial \tilde{E}_z(\omega)}{\partial y} - \frac{\partial \tilde{E}_y(\omega)}{\partial z} = -\frac{j\omega}{c_0} \left(1 + \frac{\sigma'_x}{j\omega\varepsilon_0}\right)^{-1} \left(1 + \frac{\sigma'_y}{j\omega\varepsilon_0}\right) \left(1 + \frac{\sigma'_z}{j\omega\varepsilon_0}\right) B_x(\omega) \quad (3.58)$$

$$\frac{\partial \tilde{E}_x(\omega)}{\partial z} - \frac{\partial \tilde{E}_z(\omega)}{\partial x} = -\frac{j\omega}{c_0} \left(1 + \frac{\sigma'_x}{j\omega\varepsilon_0}\right) \left(1 + \frac{\sigma'_y}{j\omega\varepsilon_0}\right)^{-1} \left(1 + \frac{\sigma'_z}{j\omega\varepsilon_0}\right) B_y(\omega) \quad (3.59)$$

$$\frac{\partial \tilde{E}_y(\omega)}{\partial x} - \frac{\partial \tilde{E}_x(\omega)}{\partial y} = -\frac{j\omega}{c_0} \left(1 + \frac{\sigma'_x}{j\omega\varepsilon_0}\right) \left(1 + \frac{\sigma'_y}{j\omega\varepsilon_0}\right) \left(1 + \frac{\sigma'_z}{j\omega\varepsilon_0}\right)^{-1} B_z(\omega) \quad (3.60)$$

$$\frac{\partial H_z(\omega)}{\partial y} - \frac{\partial H_y(\omega)}{\partial z} = \eta_0 \sigma_{xx} \tilde{E}_x(\omega) + \frac{j\omega}{c_0} \left(1 + \frac{\sigma'_x}{j\omega\varepsilon_0}\right)^{-1} \left(1 + \frac{\sigma'_y}{j\omega\varepsilon_0}\right) \left(1 + \frac{\sigma'_z}{j\omega\varepsilon_0}\right) \tilde{D}_x(\omega) \quad (3.61)$$

$$\frac{\partial H_x(\omega)}{\partial z} - \frac{\partial H_z(\omega)}{\partial x} = \eta_0 \sigma_{yy} \tilde{E}_y(\omega) + \frac{j\omega}{c_0} \left(1 + \frac{\sigma'_x}{j\omega\varepsilon_0}\right) \left(1 + \frac{\sigma'_y}{j\omega\varepsilon_0}\right)^{-1} \left(1 + \frac{\sigma'_z}{j\omega\varepsilon_0}\right) \tilde{D}_y(\omega) \quad (3.62)$$

$$\frac{\partial H_y(\omega)}{\partial x} - \frac{\partial H_x(\omega)}{\partial y} = \eta_0 \sigma_{zz} \tilde{E}_z(\omega) + \frac{j\omega}{c_0} \left(1 + \frac{\sigma'_x}{j\omega\varepsilon_0}\right) \left(1 + \frac{\sigma'_y}{j\omega\varepsilon_0}\right) \left(1 + \frac{\sigma'_z}{j\omega\varepsilon_0}\right)^{-1} \tilde{D}_z(\omega). \quad (3.63)$$

3.2.5 Conversion to Time Domain

In order to solve Maxwell's equations with PML included in the time domain the equations (3.52) - (3.63) must be converted to time domain expressions using the inverse Fourier transform. In order to illustrate this process Eq. (3.61) will be used. The conversion of the remaining equations is similar.

Starting with Eq. (3.61) below

$$\frac{\partial H_z(\omega)}{\partial y} - \frac{\partial H_y(\omega)}{\partial z} = \eta_0 \sigma_{xx} \tilde{E}_x(\omega) + \frac{j\omega}{c_0} \left(1 + \frac{\sigma'_x}{j\omega\epsilon_0}\right)^{-1} \left(1 + \frac{\sigma'_y}{j\omega\epsilon_0}\right) \left(1 + \frac{\sigma'_z}{j\omega\epsilon_0}\right) \tilde{D}_x(\omega) \quad (3.64)$$

the curl operator can be written as

$$C_x^H = \frac{\partial H_z(\omega)}{\partial y} - \frac{\partial H_y(\omega)}{\partial z}. \quad (3.65)$$

Rewriting Eq. (3.64) with (3.65) and rearranging terms gives

$$c_0 \left(1 + \frac{\sigma'_x}{j\omega\epsilon_0}\right) C_x^H = \eta_0 \sigma_{xx} \tilde{E}_x(\omega) + j\omega \left(1 + \frac{\sigma'_y}{j\omega\epsilon_0}\right) \left(1 + \frac{\sigma'_z}{j\omega\epsilon_0}\right) \tilde{D}_x(\omega). \quad (3.66)$$

Multiplying all terms in (3.66) leads to

$$c_0 C_x^H + \frac{\sigma'_x}{j\omega\epsilon_0} c_0 C_x^H = \eta_0 \sigma_{xx} \tilde{E}_x(\omega) + j\omega \tilde{D}_x(\omega) + \frac{\sigma'_y + \sigma'_z}{\epsilon_0} \tilde{D}_x(\omega) + \frac{\sigma'_z \sigma'_y}{j\omega\epsilon_0^2} \tilde{D}_x(\omega). \quad (3.67)$$

Using the following properties of the Fourier transform

$$\mathbf{F}\{g(t)\} = G(\omega) \quad (3.68)$$

$$\mathbf{F}\{ag(t)\} = aG(\omega) \quad (3.69)$$

$$\mathbf{F}\left\{\frac{d^a}{dt^a}\right\} = (j\omega)^a G(\omega) \quad (3.70)$$

$$\mathbf{F}\left\{\int_{-\infty}^t g(\tau) d\tau\right\} = \frac{1}{j\omega} G(\omega). \quad (3.71)$$

Eq. (3.67) becomes

$$c_0 C_x^H(t) + \frac{c_0 \sigma'_x}{\epsilon_0} \int_{-\infty}^t C_x^H(\tau) d\tau = \eta_0 \sigma_{xx} \tilde{E}_x(t) + \frac{\partial \tilde{D}_x(t)}{\partial t} + \frac{\sigma'_y + \sigma'_z}{\epsilon_0} \tilde{D}_x(t) + \frac{\sigma'_z \sigma'_y}{\epsilon_0^2} \int_{-\infty}^t \tilde{D}_x(\tau) d\tau. \quad (3.72)$$

Rewriting Eqs. (3.58) - (3.63) and Eqs. (3.52) - (3.57) in the time domain yields

$$\frac{\partial B_x(t)}{\partial t} + \frac{\sigma'_y + \sigma'_z}{\epsilon_0} B_x(t) + \frac{\sigma'_z \sigma'_y}{\epsilon_0^2} \int_{-\infty}^t B_x(\tau) d\tau = -c_0 C_x^E(t) - \frac{c_0 \sigma'_x}{\epsilon_0} \int_{-\infty}^t C_x^E(\tau) d\tau \quad (3.73)$$

$$\frac{\partial B_y(t)}{\partial t} + \frac{\sigma'_x + \sigma'_z}{\epsilon_0} B_y(t) + \frac{\sigma'_x \sigma'_z}{\epsilon_0^2} \int_{-\infty}^t B_y(\tau) d\tau = -c_0 C_y^E(t) - \frac{c_0 \sigma'_y}{\epsilon_0} \int_{-\infty}^t C_y^E(\tau) d\tau \quad (3.74)$$

$$\frac{\partial B_z(t)}{\partial t} + \frac{\sigma'_x + \sigma'_y}{\epsilon_0} B_z(t) + \frac{\sigma'_x \sigma'_y}{\epsilon_0^2} \int_{-\infty}^t B_z(\tau) d\tau = -c_0 C_z^E(t) - \frac{c_0 \sigma'_z}{\epsilon_0} \int_{-\infty}^t C_z^E(\tau) d\tau \quad (3.75)$$

$$\frac{\partial \tilde{D}_x(t)}{\partial t} + \frac{\sigma'_y + \sigma'_z}{\epsilon_0} \tilde{D}_x(t) + \frac{\sigma'_y \sigma'_z}{\epsilon_0^2} \int_{-\infty}^t \tilde{D}_x(\tau) d\tau + \eta_0 \sigma_{xx} \tilde{E}_x(t) = c_0 C_x^H(t) + \frac{c_0 \sigma'_x}{\epsilon_0} \int_{-\infty}^t C_x^H(\tau) d\tau \quad (3.76)$$

$$\frac{\partial \tilde{D}_y(t)}{\partial t} + \frac{\sigma'_x + \sigma'_z}{\epsilon_0} \tilde{D}_y(t) + \frac{\sigma'_x \sigma'_z}{\epsilon_0^2} \int_{-\infty}^t \tilde{D}_y(\tau) d\tau + \eta_0 \sigma_{yy} \tilde{E}_y(t) = c_0 C_y^H(t) + \frac{c_0 \sigma'_y}{\epsilon_0} \int_{-\infty}^t C_y^H(\tau) d\tau \quad (3.77)$$

$$\frac{\partial \tilde{D}_z(t)}{\partial t} + \frac{\sigma'_x + \sigma'_y}{\epsilon_0} \tilde{D}_z(t) + \frac{\sigma'_x \sigma'_y}{\epsilon_0^2} \int_{-\infty}^t \tilde{D}_z(\tau) d\tau + \eta_0 \sigma_{zz} \tilde{E}_z(t) = c_0 C_z^H(t) + \frac{c_0 \sigma'_z}{\epsilon_0} \int_{-\infty}^t C_z^H(\tau) d\tau \quad (3.78)$$

$$\tilde{D}_x(t) = \epsilon_{xx} \tilde{E}_x(t) \quad (3.79)$$

$$\tilde{D}_y(t) = \epsilon_{yy} \tilde{E}_y(t) \quad (3.80)$$

$$\tilde{D}_z(t) = \epsilon_{zz} \tilde{E}_z(t) \quad (3.81)$$

$$B_x(t) = \mu_{xx} H_x(t) \quad (3.82)$$

$$B_y(t) = \mu_{yy} H_y(t) \quad (3.83)$$

$$B_z(t) = \mu_{zz} H_z(t). \quad (3.84)$$

3.2.6 Approximation of Maxwell's Equations with PML

To solve Maxwell's equations with the PML added numerically the equations must be discretized and approximations must be made for the derivatives and integrals in the expressions. The fields are arranged using a formulation known as the Yee grid [68]. The Yee grid allows the divergence equations in Maxwell's Equations to be satisfied as well as satisfying physical boundary conditions [68, 69]. The Yee grid shown in Figure 3.1 uses staggered positions for the electric and field components which provides a graphical and intuitive interpretation of Maxwell's curl equations [69].

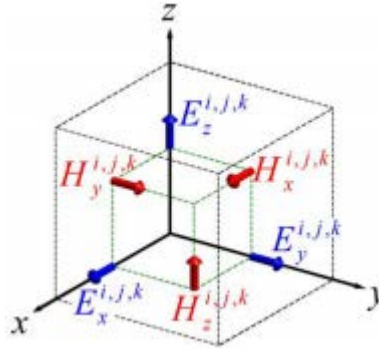


Figure 3.1: The Yee grid shown in three dimensions [68, 69]

With the field components arranged according to the Yee grid, Maxwell's equations with the PML terms are able to be discretized and approximated. Consider Eq. (3.73) as shown below.

$$\frac{\partial B_x(t)}{\partial t} + \frac{\sigma'_y + \sigma'_z}{\epsilon_0} B_x(t) + \frac{\sigma'_z \sigma'_y}{\epsilon_0^2} \int_{-\infty}^t B_x(\tau) d\tau = -c_0 C_x^E(t) - \frac{c_0 \sigma'_x}{\epsilon_0} \int_{-\infty}^t C_x^E(\tau) d\tau. \quad (3.85)$$

Each term which must be approximated is denoted by a different color. The term which is colored red can be approximated using finite-differences to be

$$\frac{\partial B_x(t)}{\partial t} \cong \frac{B_x|_{t+\Delta t/2}^{i,j,k} - B_x|_{t-\Delta t/2}^{i,j,k}}{\Delta t}. \quad (3.86)$$

It is important to note in Eq. (3.86) that the value of B_x must be known at the half time step intervals before and after time t in order for the derivative to be defined at time t . Using the fact that B , and therefore H , are defined at half time step intervals, the approximation for the term colored orange in Eq. (3.85) can be approximated at time t by interpolating the term at times $t + \Delta t / 2$ and $t - \Delta t / 2$ according to

$$\frac{\sigma'_y + \sigma'_z}{\epsilon_0} B_x(t) \cong \frac{\sigma'_y|_{t+\Delta t/2}^{i,j,k} + \sigma'_z|_{t-\Delta t/2}^{i,j,k}}{\epsilon_0} \left[\frac{B_x|_{t+\Delta t/2}^{i,j,k} + B_x|_{t-\Delta t/2}^{i,j,k}}{2} \right]. \quad (3.87)$$

The integral equation in the green colored term of Eq. (3.85) can be approximated using a summation to be

$$\frac{\sigma'_z \sigma'_y}{\epsilon_0^2} \int_{-\infty}^t B_x(\tau) d\tau \cong \frac{\sigma'_z|_{t+\Delta t/2}^{i,j,k} \sigma'_y|_{t-\Delta t/2}^{i,j,k}}{\epsilon_0^2} \sum_{T=\Delta t/2}^{t+\Delta t/2} B_x|_T^{i,j,k} \Delta t. \quad (3.88)$$

There exists a problem with Eq. (3.88) in that the summation contains a term which extends beyond the time being evaluated. In order to rectify this discrepancy, the term existing at time $t = t + \Delta t / 2$ is removed from the summation and is interpolated to time t yielding

$$\frac{\sigma'_z \sigma'_y}{\epsilon_0^2} \int_{-\infty}^t B_x(\tau) d\tau \cong \frac{\sigma'_z|_{t+\Delta t/2}^{i,j,k} \sigma'_y|_{t-\Delta t/2}^{i,j,k}}{\epsilon_0^2} \left[\frac{B_x|_{t+\Delta t/2}^{i,j,k} + B_x|_{t-\Delta t/2}^{i,j,k}}{2} \frac{\Delta t}{2} + \sum_{T=\Delta t/2}^{t-\Delta t/2} B_x|_T^{i,j,k} \Delta t \right]. \quad (3.89)$$

The term $\Delta t / 2$ multiplying the interpolated B_x term is relevant because the term is integrated over a half time step. Simplifying (3.89) leads to

$$\frac{\sigma'_z \sigma'_y}{\epsilon_0^2} \int_{-\infty}^t B_x(\tau) d\tau \cong \frac{\sigma'_z|_{t+\Delta t/2}^{i,j,k} \sigma'_y|_{t-\Delta t/2}^{i,j,k}}{\epsilon_0^2} \Delta t \left[\frac{B_x|_{t+\Delta t/2}^{i,j,k} + B_x|_{t-\Delta t/2}^{i,j,k}}{4} + \sum_{T=\Delta t/2}^{t-\Delta t/2} B_x|_T^{i,j,k} \right]. \quad (3.90)$$

The blue term in Eq. (3.85) is approximated using

$$c_0 C_x^E(t) \cong c_0 C_x^E|_t^{i,j,k}. \quad (3.91)$$

The curl term $C_x^E|_t^{i,j,k}$ is approximated using first order finite-differences to be

$$C_x^E \Big|_t^{i,j,k} = \frac{\tilde{E}_z \Big|_t^{i,j+1,k} - \tilde{E}_z \Big|_t^{i,j,k}}{\Delta y} - \frac{\tilde{E}_y \Big|_t^{i,j,k+1} - \tilde{E}_y \Big|_t^{i,j,k}}{\Delta z}. \quad (3.92)$$

Approximating the term colored magenta in Eq. (3.85) leads to

$$\frac{c_0 \sigma'_x}{\epsilon_0} \int_{-\infty}^t C_x^E(\tau) d\tau \cong \frac{c_0 \sigma'_x \Big|_t^{i,j,k}}{\epsilon_0} \sum_{T=0}^t C_x^E \Big|_T^{i,j,k} \Delta t \quad (3.93)$$

which can be simplified to

$$\frac{c_0 \sigma'_x}{\epsilon_0} \int_{-\infty}^t C_x^E(\tau) d\tau \cong \frac{c_0 \sigma'_x \Big|_t^{i,j,k}}{\epsilon_0} \Delta t \sum_{T=0}^t C_x^E \Big|_T^{i,j,k}. \quad (3.94)$$

Rewriting Eq. (3.85) using the approximations in Eq. (3.86), (3.87), (3.90), (3.91), and (3.94)

leads to

$$\begin{aligned} & \frac{B_x \Big|_{t+\Delta t/2}^{i,j,k} - B_x \Big|_{t-\Delta t/2}^{i,j,k}}{\Delta t} + \frac{\sigma'_y \Big|_t^{i,j,k} + \sigma'_z \Big|_t^{i,j,k}}{\epsilon_0} \left[\frac{B_x \Big|_{t+\Delta t/2}^{i,j,k} + B_x \Big|_{t-\Delta t/2}^{i,j,k}}{2} \right] \\ & + \frac{\sigma'_z \Big|_t^{i,j,k} \sigma'_y \Big|_t^{i,j,k}}{\epsilon_0^2} \Delta t \left[\frac{B_x \Big|_{t+\Delta t/2}^{i,j,k} + B_x \Big|_{t-\Delta t/2}^{i,j,k}}{4} + \sum_{T=\Delta t/2}^{t-\Delta t/2} B_x \Big|_T^{i,j,k} \right] \\ & = -c_0 C_x^E \Big|_t^{i,j,k} - \frac{c_0 \sigma'_x \Big|_t^{i,j,k}}{\epsilon_0} \Delta t \sum_{T=0}^t C_x^E \Big|_T^{i,j,k} \end{aligned} \quad (3.95)$$

The approximate value of Eq. (3.79) is

$$\tilde{D}_x \Big|_t^{i,j,k} = \epsilon_{xx} \Big|_t^{i,j,k} \tilde{E}_x \Big|_t^{i,j,k}. \quad (3.96)$$

The remaining equations are derived similarly.

3.2.7 Deriving the Update Equations

To solve Maxwell's equations using the Finite-Difference Time-Domain method, the value of the fields at the future time step must be determined. Consider Eq. (3.95) as written below

$$\begin{aligned}
& \frac{\textcolor{red}{B}_x|_{t+\Delta t/2}^{i,j,k} - B_x|_{t-\Delta t/2}^{i,j,k}}{\Delta t} + \frac{\sigma'_y|^{i,j,k} + \sigma'_z|^{i,j,k}}{\varepsilon_0} \left[\frac{\textcolor{red}{B}_x|_{t+\Delta t/2}^{i,j,k} + B_x|_{t-\Delta t/2}^{i,j,k}}{2} \right] \\
& + \frac{\sigma'_z|^{i,j,k} \sigma'_y|^{i,j,k} \Delta t}{\varepsilon_0^2} \left[\frac{\textcolor{red}{B}_x|_{t+\Delta t/2}^{i,j,k} + B_x|_{t-\Delta t/2}^{i,j,k}}{4} + \sum_{T=\Delta t/2}^{t-\Delta t/2} B_x|_T^{i,j,k} \right] \\
& = -c_0 C_x^E|_t^{i,j,k} - \frac{c_0 \sigma'_x|^{i,j,k} \Delta t}{\varepsilon_0} \sum_{T=0}^t C_x^E|_T^{i,j,k}
\end{aligned} \tag{3.97}$$

where the future time step is colored red. In order to isolate the term $B_x|_{t+\Delta t/2}^{i,j,k}$ in Eq. (3.97) the expression must be expanded by multiplying out and rearranging all terms. This leads to

$$\begin{aligned}
& \left(\frac{1}{\Delta t} + \frac{\sigma'_y|^{i,j,k} + \sigma'_z|^{i,j,k}}{2\varepsilon_0} + \frac{\sigma'_z|^{i,j,k} \sigma'_y|^{i,j,k} \Delta t}{4\varepsilon_0^2} \right) B_x|_{t+\Delta t/2}^{i,j,k} - \\
& \left(\frac{1}{\Delta t} - \frac{\sigma'_y|^{i,j,k} + \sigma'_z|^{i,j,k}}{2\varepsilon_0} - \frac{\sigma'_z|^{i,j,k} \sigma'_y|^{i,j,k} \Delta t}{4\varepsilon_0^2} \right) B_x|_{t-\Delta t/2}^{i,j,k} + \\
& \sum_{T=\Delta t/2}^{t-\Delta t/2} B_x|_T^{i,j,k} \frac{\sigma'_z|^{i,j,k} \sigma'_y|^{i,j,k} \Delta t}{\varepsilon_0^2} = -c_0 C_x^E|_t^{i,j,k} - \frac{c_0 \sigma'_x|^{i,j,k} \Delta t}{\varepsilon_0} \sum_{T=0}^t C_x^E|_T^{i,j,k}
\end{aligned} \tag{3.98}$$

Solving for $B_x|_{t+\Delta t/2}^{i,j,k}$ in Eq. (3.98) yields

$$B_x|_{t+\Delta t/2}^{i,j,k} = m_{Bx1}|^{i,j,k} B_x|_{t-\Delta t/2}^{i,j,k} + m_{Bx2}|^{i,j,k} C_x^E|_t^{i,j,k} + m_{Bx3}|^{i,j,k} I_{CEx}|_t^{i,j,k} + m_{Bx4}|^{i,j,k} I_{Bx}|_{t-\Delta t/2}^{i,j,k} \tag{3.99}$$

where

$$m_{Bx0}|^{i,j,k} = \frac{1}{\Delta t} + \frac{\sigma'_y|^{i,j,k} + \sigma'_z|^{i,j,k}}{2\varepsilon_0} + \frac{\sigma'_z|^{i,j,k} \sigma'_y|^{i,j,k} \Delta t}{4\varepsilon_0^2} \tag{3.100}$$

$$m_{Bx1}|^{i,j,k} = \frac{1}{m_{Bx0}|^{i,j,k}} \left(\frac{1}{\Delta t} - \frac{\sigma'_y|^{i,j,k} + \sigma'_z|^{i,j,k}}{2\varepsilon_0} - \frac{\sigma'_z|^{i,j,k} \sigma'_y|^{i,j,k} \Delta t}{4\varepsilon_0^2} \right) \tag{3.101}$$

$$m_{Bx2}|^{i,j,k} = -\frac{c_0}{m_{Bx0}|^{i,j,k}} \tag{3.102}$$

$$m_{Bx3}|^{i,j,k} = -\frac{1}{m_{Bx0}|^{i,j,k}} \frac{c_0 \sigma'_x|^{i,j,k} \Delta t}{\varepsilon_0} \tag{3.103}$$

$$m_{Bx4}|^{i,j,k} = -\frac{1}{m_{Bx0}|^{i,j,k}} \frac{\sigma'_z|^{i,j,k} \sigma'_y|^{i,j,k} \Delta t}{\varepsilon_0^2} \tag{3.104}$$

$$I_{CEx}|_t^{i,j,k} = \sum_{T=0}^t C_x^E|_T^{i,j,k} \tag{3.105}$$

$$I_{B_x}|_{t-\Delta t/2}^{i,j,k} = \sum_{T=\Delta t/2}^{t-\Delta t/2} B_x|_T^{i,j,k}. \quad (3.106)$$

The update equations for the other field components are found similarly.

3.2.8 Summary of Update Equations

B_x

$$\begin{aligned} B_x|_{t+\Delta t/2}^{i,j,k} &= m_{Bx1}|^{i,j,k} B_x|_{t-\Delta t/2}^{i,j,k} + m_{Bx2}|^{i,j,k} C_x^E|_t^{i,j,k} + m_{Bx3}|^{i,j,k} I_{CEX}|_t^{i,j,k} + m_{Bx4}|^{i,j,k} I_{Bx}|_{t-\Delta t/2}^{i,j,k} \\ m_{Bx0}|^{i,j,k} &= \frac{1}{\Delta t} + \frac{\sigma'_y|^{i,j,k} + \sigma'_z|^{i,j,k}}{2\varepsilon_0} + \frac{\sigma'_z|^{i,j,k} \sigma'_y|^{i,j,k} \Delta t}{4\varepsilon_0^2} \\ m_{Bx1}|^{i,j,k} &= \frac{1}{m_{Bx0}|^{i,j,k}} \left(\frac{1}{\Delta t} - \frac{\sigma'_y|^{i,j,k} + \sigma'_z|^{i,j,k}}{2\varepsilon_0} - \frac{\sigma'_z|^{i,j,k} \sigma'_y|^{i,j,k} \Delta t}{4\varepsilon_0^2} \right) \\ m_{Bx2}|^{i,j,k} &= -\frac{c_0}{m_{Bx0}|^{i,j,k}} \quad m_{Bx3}|^{i,j,k} = -\frac{1}{m_{Bx0}|^{i,j,k}} \frac{c_0 \sigma'_x|^{i,j,k} \Delta t}{\varepsilon_0} \\ m_{Bx4}|^{i,j,k} &= -\frac{1}{m_{Bx0}|^{i,j,k}} \frac{\sigma'_z|^{i,j,k} \sigma'_y|^{i,j,k} \Delta t}{\varepsilon_0^2} \quad I_{CEX}|_t^{i,j,k} = \sum_{T=0}^t C_x^E|_T^{i,j,k} \\ I_{Bx}|_{t-\Delta t/2}^{i,j,k} &= \sum_{T=\Delta t/2}^{t-\Delta t/2} B_x|_T^{i,j,k} \quad C_x^E|_t^{i,j,k} = \frac{\tilde{E}_z|_t^{i,j+1,k} - \tilde{E}_z|_t^{i,j,k}}{\Delta y} - \frac{\tilde{E}_y|_t^{i,j,k+1} - \tilde{E}_y|_t^{i,j,k}}{\Delta z} \end{aligned} \quad (3.107)$$

B_y

$$\begin{aligned} B_y|_{t+\Delta t/2}^{i,j,k} &= m_{By1}|^{i,j,k} B_y|_{t-\Delta t/2}^{i,j,k} + m_{By2}|^{i,j,k} C_y^E|_t^{i,j,k} + m_{By3}|^{i,j,k} I_{CEY}|_t^{i,j,k} + m_{By4}|^{i,j,k} I_{By}|_{t-\Delta t/2}^{i,j,k} \\ m_{By0}|^{i,j,k} &= \frac{1}{\Delta t} + \frac{\sigma'_x|^{i,j,k} + \sigma'_z|^{i,j,k}}{2\varepsilon_0} + \frac{\sigma'_x|^{i,j,k} \sigma'_z|^{i,j,k} \Delta t}{4\varepsilon_0^2} \\ m_{By1}|^{i,j,k} &= \frac{1}{m_{By0}|^{i,j,k}} \left(\frac{1}{\Delta t} - \frac{\sigma'_x|^{i,j,k} + \sigma'_z|^{i,j,k}}{2\varepsilon_0} - \frac{\sigma'_x|^{i,j,k} \sigma'_z|^{i,j,k} \Delta t}{4\varepsilon_0^2} \right) \\ m_{By2}|^{i,j,k} &= -\frac{c_0}{m_{By0}|^{i,j,k}} \quad m_{By3}|^{i,j,k} = -\frac{1}{m_{By0}|^{i,j,k}} \frac{c_0 \sigma'_y|^{i,j,k} \Delta t}{\varepsilon_0} \\ m_{By4}|^{i,j,k} &= -\frac{1}{m_{By0}|^{i,j,k}} \frac{\sigma'_x|^{i,j,k} \sigma'_z|^{i,j,k} \Delta t}{\varepsilon_0^2} \quad I_{CEY}|_t^{i,j,k} = \sum_{T=0}^t C_y^E|_T^{i,j,k} \\ I_{By}|_{t-\Delta t/2}^{i,j,k} &= \sum_{T=\Delta t/2}^{t-\Delta t/2} B_y|_T^{i,j,k} \quad C_y^E|_t^{i,j,k} = \frac{\tilde{E}_x|_t^{i,j,k+1} - \tilde{E}_x|_t^{i,j,k}}{\Delta z} - \frac{\tilde{E}_z|_t^{i+1,j,k} - \tilde{E}_z|_t^{i,j,k}}{\Delta x} \end{aligned} \quad (3.108)$$

B_z

$$\begin{aligned}
B_z|_{t+\Delta t/2}^{i,j,k} &= m_{Bz1}|^{i,j,k} B_z|_{t-\Delta t/2}^{i,j,k} + m_{Bz2}|^{i,j,k} C_z^E|_t^{i,j,k} + m_{Bz3}|^{i,j,k} I_{CEz}|_t^{i,j,k} + m_{Bz4}|^{i,j,k} I_{Bz}|_{t-\Delta t/2}^{i,j,k} \\
m_{Bz0}|^{i,j,k} &= \frac{1}{\Delta t} + \frac{\sigma'_x|^{i,j,k} + \sigma'_y|^{i,j,k}}{2\varepsilon_0} + \frac{\sigma'_x|^{i,j,k} \sigma'_y|^{i,j,k} \Delta t}{4\varepsilon_0^2} \\
m_{Bz1}|^{i,j,k} &= \frac{1}{m_{Bz0}|^{i,j,k}} \left(\frac{1}{\Delta t} - \frac{\sigma'_x|^{i,j,k} + \sigma'_y|^{i,j,k}}{2\varepsilon_0} - \frac{\sigma'_x|^{i,j,k} \sigma'_y|^{i,j,k} \Delta t}{4\varepsilon_0^2} \right) \\
m_{Bz2}|^{i,j,k} &= -\frac{c_0}{m_{Bz0}|^{i,j,k}} \quad m_{Bz3}|^{i,j,k} = -\frac{1}{m_{Bz0}|^{i,j,k}} \frac{c_0 \sigma'_z|^{i,j,k} \Delta t}{\varepsilon_0} \\
m_{Bz4}|^{i,j,k} &= -\frac{1}{m_{Bz0}|^{i,j,k}} \frac{\sigma'_x|^{i,j,k} \sigma'_y|^{i,j,k} \Delta t}{\varepsilon_0^2} \quad I_{CEz}|_t^{i,j,k} = \sum_{T=0}^t C_z^E|_T^{i,j,k} \\
I_{Bz}|_{t-\Delta t/2}^{i,j,k} &= \sum_{T=\Delta t/2}^{t-\Delta t/2} B_z|_T^{i,j,k} \quad C_z^E|_t^{i,j,k} = \frac{\tilde{E}_y|_t^{i+1,j,k} - \tilde{E}_y|_t^{i,j,k}}{\Delta x} - \frac{\tilde{E}_x|_t^{i,j+1,k} - \tilde{E}_x|_t^{i,j,k}}{\Delta y}
\end{aligned} \tag{3.109}$$

D_x

$$\begin{aligned}
\tilde{D}_x|_{t+\Delta t}^{i,j,k} &= m_{Dx1}|^{i,j,k} \tilde{D}_x|_t^{i,j,k} + m_{Dx2}|^{i,j,k} C_x^H|_{t+\Delta t/2}^{i,j,k} + m_{Dx3}|^{i,j,k} I_{CHx}|_{t-\Delta t/2}^{i,j,k} + m_{Dx4}|^{i,j,k} I_{Dx}|_{t-\Delta t}^{i,j,k} + m_{Dx5}|^{i,j,k} \tilde{E}_x|_t^{i,j,k} \\
m_{Dx0}|^{i,j,k} &= \frac{1}{\Delta t} + \frac{\sigma'_y|^{i,j,k} + \sigma'_z|^{i,j,k}}{2\varepsilon_0} + \frac{\sigma'_y|^{i,j,k} \sigma'_z|^{i,j,k} \Delta t}{4\varepsilon_0^2} \\
m_{Dx1}|^{i,j,k} &= \frac{1}{m_{Dx0}|^{i,j,k}} \left(\frac{1}{\Delta t} - \frac{\sigma'_y|^{i,j,k} + \sigma'_z|^{i,j,k}}{2\varepsilon_0} - \frac{\sigma'_y|^{i,j,k} \sigma'_z|^{i,j,k} \Delta t}{4\varepsilon_0^2} \right) \\
m_{Dx2}|^{i,j,k} &= -\frac{c_0}{m_{Dx0}|^{i,j,k}} \quad m_{Dx3}|^{i,j,k} = -\frac{1}{m_{Dx0}|^{i,j,k}} \frac{c_0 \sigma'_x|^{i,j,k} \Delta t}{\varepsilon_0} \\
m_{Dx4}|^{i,j,k} &= -\frac{1}{m_{Dx0}|^{i,j,k}} \frac{\sigma'_y|^{i,j,k} \sigma'_z|^{i,j,k} \Delta t}{\varepsilon_0^2} \quad m_{Dx5}|^{i,j,k} = \eta_0 \sigma_{xx}|^{i,j,k} \tilde{E}_x|_t^{i,j,k} \\
I_{CHx}|_t^{i,j,k} &= \sum_{T=0}^t C_x^H|_T^{i,j,k} \quad I_{Dx}|_{t-\Delta t/2}^{i,j,k} = \sum_{T=\Delta t/2}^{t-\Delta t/2} \tilde{D}_x|_T^{i,j,k} \quad C_x^H|_{t+\Delta t/2}^{i,j,k} = \frac{H_z|_{t+\Delta t/2}^{i,j,k} - H_z|_{t+\Delta t/2}^{i,j-1,k}}{\Delta y} - \frac{H_y|_{t+\Delta t/2}^{i,j,k} - H_y|_{t+\Delta t/2}^{i,j,k-1}}{\Delta z}
\end{aligned} \tag{3.110}$$

D_y

$$\begin{aligned}
\tilde{D}_y \Big|_{t+\Delta t}^{i,j,k} &= m_{Dy1} \Big|_{t+\Delta t}^{i,j,k} \tilde{D}_y \Big|_t^{i,j,k} + m_{Dy2} \Big|_{t+\Delta t}^{i,j,k} C_y^H \Big|_{t+\Delta t/2}^{i,j,k} + m_{Dy3} \Big|_{t+\Delta t}^{i,j,k} I_{CHy} \Big|_{t-\Delta t/2}^{i,j,k} + m_{Dy4} \Big|_{t+\Delta t}^{i,j,k} I_{Dy} \Big|_{t-\Delta t}^{i,j,k} + m_{Dy5} \tilde{E}_y \Big|_t^{i,j,k} \\
m_{Dy0} \Big|_{t+\Delta t}^{i,j,k} &= \frac{1}{\Delta t} + \frac{\sigma'_x \Big|_{t+\Delta t}^{i,j,k} + \sigma'_z \Big|_{t+\Delta t}^{i,j,k}}{2\varepsilon_0} + \frac{\sigma'_x \Big|_{t+\Delta t}^{i,j,k} \sigma'_z \Big|_{t+\Delta t}^{i,j,k} \Delta t}{4\varepsilon_0^2} \\
m_{Dy1} \Big|_{t+\Delta t}^{i,j,k} &= \frac{1}{m_{Dy0} \Big|_{t+\Delta t}^{i,j,k}} \left(\frac{1}{\Delta t} - \frac{\sigma'_x \Big|_{t+\Delta t}^{i,j,k} + \sigma'_z \Big|_{t+\Delta t}^{i,j,k}}{2\varepsilon_0} - \frac{\sigma'_x \Big|_{t+\Delta t}^{i,j,k} \sigma'_z \Big|_{t+\Delta t}^{i,j,k} \Delta t}{4\varepsilon_0^2} \right) \\
m_{Dy2} \Big|_{t+\Delta t}^{i,j,k} &= -\frac{c_0}{m_{Dy0} \Big|_{t+\Delta t}^{i,j,k}} \quad m_{Dy3} \Big|_{t+\Delta t}^{i,j,k} = -\frac{1}{m_{Dy0} \Big|_{t+\Delta t}^{i,j,k}} \frac{c_0 \sigma'_y \Big|_{t+\Delta t}^{i,j,k} \Delta t}{\varepsilon_0} \\
m_{Dy4} \Big|_{t+\Delta t}^{i,j,k} &= -\frac{1}{m_{Dy0} \Big|_{t+\Delta t}^{i,j,k}} \frac{\sigma'_x \Big|_{t+\Delta t}^{i,j,k} \sigma'_z \Big|_{t+\Delta t}^{i,j,k} \Delta t}{\varepsilon_0^2} \quad m_{Dy5} = \eta_0 \sigma_{yy} \Big|_t^{i,j,k} \tilde{E}_y \Big|_t^{i,j,k} \\
I_{CHy} \Big|_t^{i,j,k} &= \sum_{T=0}^t C_y^H \Big|_T^{i,j,k} \quad I_{Dy} \Big|_{t-\Delta t/2}^{i,j,k} = \sum_{T=\Delta t/2}^{t-\Delta t/2} \tilde{D}_y \Big|_T^{i,j,k} \quad C_y^H \Big|_{t+\Delta t/2}^{i,j,k} = \frac{H_x \Big|_{t+\Delta t/2}^{i,j,k} - H_x \Big|_{t+\Delta t/2}^{i,j,k-1}}{\Delta z} - \frac{H_z \Big|_{t+\Delta t/2}^{i,j,k} - H_z \Big|_{t+\Delta t/2}^{i,j,k-1}}{\Delta x}
\end{aligned} \tag{3.111}$$

D_z

$$\begin{aligned}
\tilde{D}_z \Big|_{t+\Delta t}^{i,j,k} &= m_{Dz1} \Big|_{t+\Delta t}^{i,j,k} \tilde{D}_z \Big|_t^{i,j,k} + m_{Dz2} \Big|_{t+\Delta t}^{i,j,k} C_z^H \Big|_{t+\Delta t/2}^{i,j,k} + m_{Dz3} \Big|_{t+\Delta t}^{i,j,k} I_{CHz} \Big|_{t-\Delta t/2}^{i,j,k} + m_{Dz4} \Big|_{t+\Delta t}^{i,j,k} I_{Dz} \Big|_{t-\Delta t}^{i,j,k} + m_{Dz5} \tilde{E}_z \Big|_t^{i,j,k} \\
m_{Dz0} \Big|_{t+\Delta t}^{i,j,k} &= \frac{1}{\Delta t} + \frac{\sigma'_x \Big|_{t+\Delta t}^{i,j,k} + \sigma'_y \Big|_{t+\Delta t}^{i,j,k}}{2\varepsilon_0} + \frac{\sigma'_x \Big|_{t+\Delta t}^{i,j,k} \sigma'_y \Big|_{t+\Delta t}^{i,j,k} \Delta t}{4\varepsilon_0^2} \\
m_{Dz1} \Big|_{t+\Delta t}^{i,j,k} &= \frac{1}{m_{Dz0} \Big|_{t+\Delta t}^{i,j,k}} \left(\frac{1}{\Delta t} - \frac{\sigma'_x \Big|_{t+\Delta t}^{i,j,k} + \sigma'_y \Big|_{t+\Delta t}^{i,j,k}}{2\varepsilon_0} - \frac{\sigma'_x \Big|_{t+\Delta t}^{i,j,k} \sigma'_y \Big|_{t+\Delta t}^{i,j,k} \Delta t}{4\varepsilon_0^2} \right) \\
m_{Dz2} \Big|_{t+\Delta t}^{i,j,k} &= -\frac{c_0}{m_{Dz0} \Big|_{t+\Delta t}^{i,j,k}} \quad m_{Dz3} \Big|_{t+\Delta t}^{i,j,k} = -\frac{1}{m_{Dz0} \Big|_{t+\Delta t}^{i,j,k}} \frac{c_0 \sigma'_z \Big|_{t+\Delta t}^{i,j,k} \Delta t}{\varepsilon_0} \\
m_{Dz4} \Big|_{t+\Delta t}^{i,j,k} &= -\frac{1}{m_{Dz0} \Big|_{t+\Delta t}^{i,j,k}} \frac{\sigma'_x \Big|_{t+\Delta t}^{i,j,k} \sigma'_y \Big|_{t+\Delta t}^{i,j,k} \Delta t}{\varepsilon_0^2} \quad m_{Dz5} = \eta_0 \sigma_{zz} \Big|_t^{i,j,k} \tilde{E}_z \Big|_t^{i,j,k} \\
I_{CHz} \Big|_t^{i,j,k} &= \sum_{T=0}^t C_z^H \Big|_T^{i,j,k} \quad I_{Dz} \Big|_{t-\Delta t/2}^{i,j,k} = \sum_{T=\Delta t/2}^{t-\Delta t/2} \tilde{D}_z \Big|_T^{i,j,k} \quad C_z^H \Big|_{t+\Delta t/2}^{i,j,k} = \frac{H_y \Big|_{t+\Delta t/2}^{i,j,k} - H_y \Big|_{t+\Delta t/2}^{i-1,j,k}}{\Delta x} - \frac{H_x \Big|_{t+\Delta t/2}^{i,j,k} - H_x \Big|_{t+\Delta t/2}^{i,j,k-1}}{\Delta y}
\end{aligned} \tag{3.112}$$

E_x

$$\begin{aligned}
\tilde{E}_x \Big|_{t+\Delta t}^{i,j,k} &= m_{Ex1} \Big|_{t+\Delta t}^{i,j,k} \tilde{D}_x \Big|_{t+\Delta t}^{i,j,k} \\
m_{Ex1} \Big|_{t+\Delta t}^{i,j,k} &= \frac{1}{\varepsilon_{xx} \Big|_{t+\Delta t}^{i,j,k}}
\end{aligned} \tag{3.113}$$

E_y

$$\begin{aligned}
\tilde{E}_y \Big|_{t+\Delta t}^{i,j,k} &= m_{Ey1} \Big|_{t+\Delta t}^{i,j,k} \tilde{D}_y \Big|_{t+\Delta t}^{i,j,k} \\
m_{Ey1} \Big|_{t+\Delta t}^{i,j,k} &= \frac{1}{\varepsilon_{yy} \Big|_{t+\Delta t}^{i,j,k}}
\end{aligned} \tag{3.114}$$

E_z

$$\begin{aligned}\tilde{E}_z \Big|_{t+\Delta t}^{i,j,k} &= m_{Ez1} \Big|_{t+\Delta t}^{i,j,k} \tilde{D}_z \Big|_{t+\Delta t}^{i,j,k} \\ m_{Ez1} \Big|_{t+\Delta t}^{i,j,k} &= \frac{1}{\epsilon_{zz} \Big|_{t+\Delta t}^{i,j,k}}\end{aligned}\tag{3.115}$$

H_x

$$\begin{aligned}H_x \Big|_{t+\Delta t}^{i,j,k} &= m_{Hx1} \Big|_{t+\Delta t}^{i,j,k} B_x \Big|_{t+\Delta t}^{i,j,k} \\ m_{Hx1} \Big|_{t+\Delta t}^{i,j,k} &= \frac{1}{\mu_{xx} \Big|_{t+\Delta t}^{i,j,k}}\end{aligned}\tag{3.116}$$

H_y

$$\begin{aligned}H_y \Big|_{t+\Delta t}^{i,j,k} &= m_{Hy1} \Big|_{t+\Delta t}^{i,j,k} B_y \Big|_{t+\Delta t}^{i,j,k} \\ m_{Hy1} \Big|_{t+\Delta t}^{i,j,k} &= \frac{1}{\mu_{yy} \Big|_{t+\Delta t}^{i,j,k}}\end{aligned}\tag{3.117}$$

H_z

$$\begin{aligned}H_z \Big|_{t+\Delta t}^{i,j,k} &= m_{Hz1} \Big|_{t+\Delta t}^{i,j,k} B_z \Big|_{t+\Delta t}^{i,j,k} \\ m_{Hz1} \Big|_{t+\Delta t}^{i,j,k} &= \frac{1}{\mu_{zz} \Big|_{t+\Delta t}^{i,j,k}}\end{aligned}\tag{3.118}$$

3.2.9 Total-Field/Scattered-Field Source

In order to implement a plane wave source in which the effect of a scattered wave may be characterized with FDTD a method known as *Total-Field Scattered-Field* (TF/SF) is used [63, 70]. TF/SF allows for the computational domain to be divided into two regions: the total-field region and the scattered field region. This has the effect of allowing for the propagation of a one-way source originating on the TF/SF boundary and traveling away from the boundary as shown in Figure 3.2. This figure shows the construction of a periodic unit cell within an FDTD grid on the left and the effect of the TF/SF boundary on propagating waves on the right.

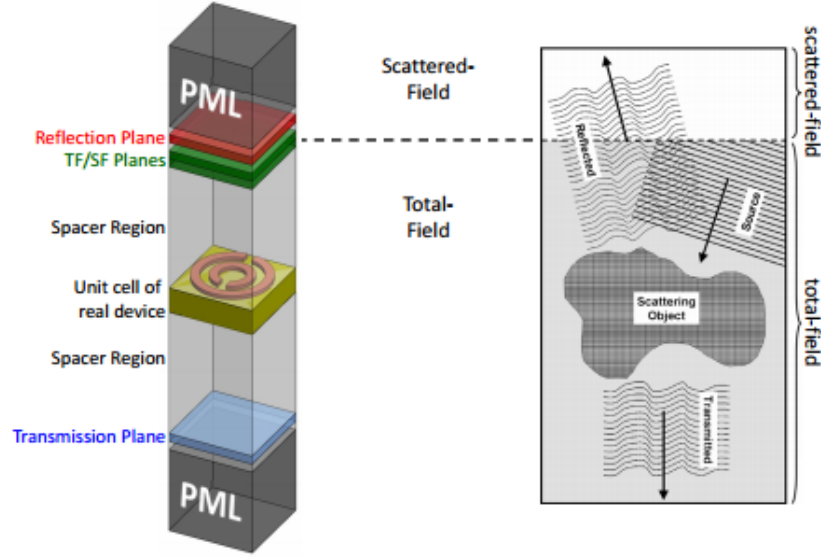


Figure 3.2: Total-Field/Scattered-Field Implementation. The figure on the left shows a typical periodic unit cell with PML on the $\pm z$ boundaries, a reflection plane, a transmission plane, periodic boundary conditions on the $\pm x$ and $\pm y$ boundaries, and a TF/SF boundary. The figure on the right shows the effect of the TF/SF boundary on propagating waves as shown in Ref. [63].

Consider the finite-difference approximation of Maxwell's curl equations at the TF/SF boundary which is the x - y plane between positions $k_{src} - 1$ and k_{src}

$$C_x^E \Big|_t^{i,j,k_{src}-1} = \frac{\tilde{E}_z \Big|_t^{i,j+1,k_{src}-1} - \tilde{E}_z \Big|_t^{i,j,k_{src}-1}}{\Delta y} - \frac{\tilde{E}_y \Big|_t^{i,j,k_{src}} - \tilde{E}_y \Big|_t^{i,j,k_{src}-1}}{\Delta z} \quad (3.119)$$

$$C_y^E \Big|_t^{i,j,k_{src}-1} = \frac{\tilde{E}_x \Big|_t^{i,j,k_{src}} - \tilde{E}_x \Big|_t^{i,j,k_{src}-1}}{\Delta z} - \frac{\tilde{E}_z \Big|_t^{i,j+1,k_{src}-1} - \tilde{E}_z \Big|_t^{i,j,k_{src}-1}}{\Delta x} \quad (3.120)$$

$$C_z^E \Big|_t^{i,j,k_{src}-1} = \frac{\tilde{E}_y \Big|_t^{i,j+1,k_{src}-1} - \tilde{E}_y \Big|_t^{i,j,k_{src}-1}}{\Delta x} - \frac{\tilde{E}_x \Big|_t^{i,j+1,k_{src}-1} - \tilde{E}_x \Big|_t^{i,j,k_{src}-1}}{\Delta y} \quad (3.121)$$

$$C_x^H \Big|_{t+\Delta t/2}^{i,j,k_{src}} = \frac{H_z \Big|_{t+\Delta t/2}^{i,j,k_{src}} - H_z \Big|_{t+\Delta t/2}^{i,j-1,k_{src}}}{\Delta y} - \frac{H_y \Big|_{t+\Delta t/2}^{i,j,k_{src}} - H_y \Big|_{t+\Delta t/2}^{i,j,k_{src}-1}}{\Delta z} \quad (3.122)$$

$$C_y^H \Big|_{t+\Delta t/2}^{i,j,k_{src}} = \frac{H_x \Big|_{t+\Delta t/2}^{i,j,k_{src}} - H_x \Big|_{t+\Delta t/2}^{i,j,k_{src}-1}}{\Delta z} - \frac{H_z \Big|_{t+\Delta t/2}^{i,j,k_{src}} - H_z \Big|_{t+\Delta t/2}^{i-1,j,k_{src}}}{\Delta x} \quad (3.123)$$

$$C_z^H \Big|_{t+\Delta t/2}^{i,j,k_{src}} = \frac{H_y \Big|_{t+\Delta t/2}^{i,j,k_{src}} - H_y \Big|_{t+\Delta t/2}^{i-1,j,k_{src}}}{\Delta x} - \frac{H_x \Big|_{t+\Delta t/2}^{i,j,k_{src}} - H_x \Big|_{t+\Delta t/2}^{i,j-1,k_{src}}}{\Delta y} \quad (3.124)$$

The field quantities in Eqs. (3.119) and (3.120) colored red exist on the total-field side of the boundary while all other terms exist solely on the scattered-field side. Similarly, Eqs. (3.122) and

(3.123) contain terms, colored blue, from the scattered-field side of the TF/SF boundary while the remaining terms are on the total-field side of the boundary.

To ensure that all terms in Eqs. (3.119) and (3.120) reflect the correct side of the TF/SF boundary that the calculation occurs on, two source terms $\tilde{\mathbf{E}}_x^{src} \Big|_t^{i,j,k_{src}}$ and $\tilde{\mathbf{E}}_y^{src} \Big|_t^{i,j,k_{src}}$ must be subtracted from the total-field terms. This correction leads to

$$C_x^E \Big|_t^{i,j,k_{src}-1} = \frac{\tilde{E}_z \Big|_t^{i,j+1,k_{src}-1} - \tilde{E}_z \Big|_t^{i,j,k_{src}-1}}{\Delta y} - \frac{\left(\tilde{E}_y \Big|_t^{i,j,k_{src}} - \tilde{E}_y^{src} \Big|_t^{i,j,k_{src}} \right) - \tilde{E}_y \Big|_t^{i,j,k_{src}-1}}{\Delta z} \quad (3.125)$$

$$C_y^E \Big|_t^{i,j,k_{src}-1} = \frac{\left(\tilde{E}_x \Big|_t^{i,j,k_{src}} - \tilde{E}_x^{src} \Big|_t^{i,j,k_{src}} \right) - \tilde{E}_x \Big|_t^{i,j,k_{src}-1}}{\Delta z} - \frac{\tilde{E}_z \Big|_t^{i+1,j,k_{src}-1} - \tilde{E}_z \Big|_t^{i,j,k_{src}-1}}{\Delta x}. \quad (3.126)$$

These equations can be further simplified to

$$C_x^E \Big|_t^{i,j,k_{src}-1} = \frac{\tilde{E}_z \Big|_t^{i,j+1,k_{src}-1} - \tilde{E}_z \Big|_t^{i,j,k_{src}-1}}{\Delta y} - \frac{\tilde{E}_y \Big|_t^{i,j,k_{src}} - \tilde{E}_y \Big|_t^{i,j,k_{src}-1}}{\Delta z} + \frac{1}{\Delta z} \tilde{E}_y^{src} \Big|_t^{i,j,k_{src}} \quad (3.127)$$

$$C_y^E \Big|_t^{i,j,k_{src}-1} = \frac{\tilde{E}_x \Big|_t^{i,j,k_{src}} - \tilde{E}_x \Big|_t^{i,j,k_{src}-1}}{\Delta z} - \frac{\tilde{E}_z \Big|_t^{i+1,j,k_{src}-1} - \tilde{E}_z \Big|_t^{i,j,k_{src}-1}}{\Delta x} - \frac{1}{\Delta z} \tilde{E}_x^{src} \Big|_t^{i,j,k_{src}}. \quad (3.128)$$

Correcting for the total-field terms in Eqs. (3.122) and (3.123) by adding the source terms $\mathbf{H}_x^{src} \Big|_{t+\Delta t/2}^{i,j,k_{src}-1}$ and $\mathbf{H}_y^{src} \Big|_{t+\Delta t/2}^{i,j,k_{src}-1}$ to the scattered-field terms. This is written as

$$C_x^H \Big|_{t+\Delta t/2}^{i,j,k_{src}} = \frac{H_z \Big|_{t+\Delta t/2}^{i,j,k_{src}} - H_z \Big|_{t+\Delta t/2}^{i,j-1,k_{src}}}{\Delta y} - \frac{H_y \Big|_{t+\Delta t/2}^{i,j,k_{src}} - \left(H_y \Big|_{t+\Delta t/2}^{i,j,k_{src}-1} + H_y^{src} \Big|_{t+\Delta t/2}^{i,j,k_{src}-1} \right)}{\Delta z} \quad (3.129)$$

$$C_y^H \Big|_{t+\Delta t/2}^{i,j,k_{src}} = \frac{H_x \Big|_{t+\Delta t/2}^{i,j,k_{src}} - \left(H_x \Big|_{t+\Delta t/2}^{i,j,k_{src}-1} + H_x^{src} \Big|_{t+\Delta t/2}^{i,j,k_{src}-1} \right)}{\Delta z} - \frac{H_z \Big|_{t+\Delta t/2}^{i,j,k_{src}} - H_z \Big|_{t+\Delta t/2}^{i,j-1,k_{src}}}{\Delta x}. \quad (3.130)$$

Simplification leads to

$$C_x^H \Big|_{t+\Delta t/2}^{i,j,k_{src}} = \frac{H_z \Big|_{t+\Delta t/2}^{i,j,k_{src}} - H_z \Big|_{t+\Delta t/2}^{i,j-1,k_{src}}}{\Delta y} - \frac{H_y \Big|_{t+\Delta t/2}^{i,j,k_{src}} - H_y \Big|_{t+\Delta t/2}^{i,j,k_{src}-1}}{\Delta z} + \frac{1}{\Delta z} H_y^{src} \Big|_{t+\Delta t/2}^{i,j,k_{src}-1} \quad (3.131)$$

$$C_y^H \Big|_{t+\Delta t/2}^{i,j,k_{src}} = \frac{H_x \Big|_{t+\Delta t/2}^{i,j,k_{src}} - H_x \Big|_{t+\Delta t/2}^{i,j,k_{src}-1}}{\Delta z} - \frac{H_z \Big|_{t+\Delta t/2}^{i,j,k_{src}} - H_z \Big|_{t+\Delta t/2}^{i,j-1,k_{src}}}{\Delta x} - \frac{1}{\Delta z} H_x^{src} \Big|_{t+\Delta t/2}^{i,j,k_{src}-1}. \quad (3.132)$$

The expressions given in Eqs. (3.127), (3.128), (3.131), and (3.132) are simply the curl equations with the modification of the source term at the TF/SF interface. For the source terms to be consistent

and exist at the proper place and times they must be defined correctly. For an electric field source with polarization vector

$$\vec{P}(\vec{r}) = P_x \hat{x} + P_y \hat{y} \quad (3.133)$$

the source terms can be written as

$$\tilde{E}_x^{src} \Big|_t^{i,j,k_{src}} = P_x \cdot g(t) \quad (3.134)$$

$$\tilde{E}_y^{src} \Big|_t^{i,j,k_{src}} = P_y \cdot g(t) \quad (3.135)$$

where $g(t)$ is the waveform being injected into the simulation. Since the electric and magnetic fields exist at one-half time steps from one another and at different positions within the Yee grid, the magnetic field source term must be modified to account for this difference. Defining the term

$$\delta t = -\frac{n_{inc} \Delta z}{2c_0} + \frac{\Delta t}{2} \quad (3.136)$$

where n_{inc} is the refractive index at the TF/SF boundary, the magnetic field source terms are given as

$$H_x^{src} \Big|_{t+\Delta t/2}^{i,j,k_{src}-1} = -P_y \sqrt{\frac{\epsilon_{r,inc}}{\mu_{r,inc}}} \cdot g(t + \delta t) \quad (3.137)$$

$$H_y^{src} \Big|_{t+\Delta t/2}^{i,j,k_{src}-1} = P_x \sqrt{\frac{\epsilon_{r,inc}}{\mu_{r,inc}}} \cdot g(t + \delta t) \quad (3.138)$$

with $\epsilon_{r,inc}$ and $\mu_{r,inc}$ being the permittivity and permeability, respectively, at the TF/SF interface.

Chapter 4: Simulation of Anisotropic Devices Using Finite-Difference Frequency-Domain

4.1 FORMULATION

Finite-difference frequency-domain (FDFD) is an easy method to implement, yet extremely powerful tool for the simulation of electromagnetic devices [71]. FDFD can be extended to simulate anisotropic devices such as those presented in Chapter 5 as described below and in Ref. [17].

4.1.1 Maxwell's Equations

Beginning with Maxwell's curl equations in the frequency domain in a charge-free space

$$\nabla \times \vec{E} = -j\omega \vec{B} \quad (4.1)$$

$$\nabla \times \vec{H} = j\omega \vec{D} \quad (4.2)$$

and the constitutive relations

$$\vec{D} = [\varepsilon] \vec{E} \quad (4.3)$$

$$\vec{B} = [\mu] \vec{H} \quad (4.4)$$

where the permittivity tensor is

$$[\varepsilon] = \varepsilon_0 [\varepsilon_r] = \varepsilon_0 \begin{bmatrix} \varepsilon_{xx} & \varepsilon_{xy} & \varepsilon_{xz} \\ \varepsilon_{yx} & \varepsilon_{yy} & \varepsilon_{yz} \\ \varepsilon_{zx} & \varepsilon_{zy} & \varepsilon_{zz} \end{bmatrix} \quad (4.5)$$

and the permeability tensor is

$$[\mu] = \mu_0 [\mu_r] = \mu_0 \begin{bmatrix} \mu_{xx} & \mu_{xy} & \mu_{xz} \\ \mu_{yx} & \mu_{yy} & \mu_{yz} \\ \mu_{zx} & \mu_{zy} & \mu_{zz} \end{bmatrix} \quad (4.6)$$

a rigorous method for the simulation of three-dimensional anisotropic devices will be developed. In order to minimize truncation error [72] the magnetic field intensity and electric field intensity should be roughly the same order of magnitude. Normalizing the magnetic field such that

$$\vec{\tilde{H}} = -j\eta_0 \vec{H} \quad (4.7)$$

where η_0 is the free space wave impedance given by $\eta_0 = \sqrt{\mu_0 / \varepsilon_0} \approx 377 \, \Omega$. Using the relation

$k_0 = \omega / c_0$ and rewriting Eqs. (4.1) and (4.2) with the inclusion of Eqs. (4.3) and (4.4) along with the normalized magnetic field intensity Eq. (4.7) gives

$$\nabla \times \vec{E} = k_0 [\mu_r] \vec{H} \quad (4.8)$$

$$\nabla \times \vec{H} = k_0 [\varepsilon_r] \vec{E} . \quad (4.9)$$

To further simplify Eqs. (4.8) and (4.9) the grid coordinates are normalized with respect to k_0 giving

$$\tilde{x} = k_0 x \quad (4.10)$$

$$\tilde{y} = k_0 y \quad (4.11)$$

$$\tilde{z} = k_0 z \quad (4.12)$$

Rewriting Eqs. (4.8) and (4.9) with the normalized grid coordinates of Eqs. (4.10) - (4.12) leads to

$$\tilde{\nabla} \times \vec{E} = k_0 [\mu_r] \vec{H} \quad (4.13)$$

$$\tilde{\nabla} \times \vec{H} = k_0 [\varepsilon_r] \vec{E} \quad (4.14)$$

where the partial derivatives in the curl operator are with respect the normalized grid coordinates.

4.1.2 Uniaxial Perfectly Matched Layers

To limit the domain of an electromagnetic simulation, some form of absorbing boundary condition must be used. A very powerful, yet easy to implement, approach is to use the UPML [17, 65, 66, 71]. The UPML is an absorbing boundary which incorporates loss in the boundary region while minimizing reflection. The UPML is also independent of the angle of incidence and polarization of the energy incident on the UPML region [64]. In order to implement the UPML, Maxwell's equations (4.8) and (4.9) are modified using the tensor

$$[s] = \begin{bmatrix} \frac{s_y s_z}{s_x} & 0 & 0 \\ 0 & \frac{s_x s_z}{s_y} & 0 \\ 0 & 0 & \frac{s_x s_y}{s_z} \end{bmatrix} \quad (4.15)$$

where

$$s_x(x) = s_{x0}(x) [1 - j\eta_0 \sigma'_x(x)] \quad s_{x0}(x) = 1 + s_{\max} \cdot \left(\frac{x}{L_x} \right)^p \quad (4.16)$$

$$\sigma'_x(x) = \sigma'_{\max} \sin^2 \left(\frac{\pi x}{2L_x} \right)$$

$$s_y(y) = s_{y0}(y) [1 - j\eta_0 \sigma'_y(y)] \quad s_{y0}(y) = 1 + s_{\max} \cdot \left(\frac{y}{L_y} \right)^p \quad (4.17)$$

$$\sigma'_y(y) = \sigma'_{\max} \sin^2 \left(\frac{\pi y}{2L_y} \right)$$

$$s_z(z) = s_{z0}(z) [1 - j\eta_0 \sigma'_z(z)] \quad s_{z0}(z) = 1 + s_{\max} \cdot \left(\frac{z}{L_z} \right)^p \quad (4.18)$$

$$\sigma'_z(z) = \sigma'_{\max} \sin^2 \left(\frac{\pi z}{2L_z} \right)$$

Several terms in Eqs. (4.16) - (4.18) can be adjusted to control the performance of the PML.

Ranges for these values which are standard are [71]

$$1 \leq p < 5 \quad (4.19)$$

$$0 \leq s_{\max} \leq 5 \quad (4.20)$$

$$\sigma'_{\max} = 1. \quad (4.21)$$

The terms L_x , L_y , and L_z are the lengths of the PML regions in the x , y , and z regions respectively. The PML tensor is incorporated into Maxwell's equations by multiplying with the material tensors to give [17]

$$[\mu'_r] = \begin{bmatrix} \mu'_{xx} & \mu'_{xy} & \mu'_{xz} \\ \mu'_{yx} & \mu'_{yy} & \mu'_{yz} \\ \mu'_{zx} & \mu'_{zy} & \mu'_{zz} \end{bmatrix} = \begin{bmatrix} \mu_{xx} \frac{s_y s_z}{s_x} & \mu_{xy} \frac{s_x s_z}{s_y} & \mu_{xz} \frac{s_x s_y}{s_z} \\ \mu_{yx} \frac{s_y s_z}{s_x} & \mu_{yy} \frac{s_x s_z}{s_y} & \mu_{yz} \frac{s_x s_y}{s_z} \\ \mu_{zx} \frac{s_y s_z}{s_x} & \mu_{zy} \frac{s_x s_z}{s_y} & \mu_{zz} \frac{s_x s_y}{s_z} \end{bmatrix} \quad (4.22)$$

$$[\epsilon'_r] = \begin{bmatrix} \epsilon'_{xx} & \epsilon'_{xy} & \epsilon'_{xz} \\ \epsilon'_{yx} & \epsilon'_{yy} & \epsilon'_{yz} \\ \epsilon'_{zx} & \epsilon'_{zy} & \epsilon'_{zz} \end{bmatrix} = \begin{bmatrix} \epsilon_{xx} \frac{s_y s_z}{s_x} & \epsilon_{xy} \frac{s_x s_z}{s_y} & \epsilon_{xz} \frac{s_x s_y}{s_z} \\ \epsilon_{yx} \frac{s_y s_z}{s_x} & \epsilon_{yy} \frac{s_x s_z}{s_y} & \epsilon_{yz} \frac{s_x s_y}{s_z} \\ \epsilon_{zx} \frac{s_y s_z}{s_x} & \epsilon_{zy} \frac{s_x s_z}{s_y} & \epsilon_{zz} \frac{s_x s_y}{s_z} \end{bmatrix} \quad (4.23)$$

leading to writing Maxwell's equations in the form

$$\tilde{\nabla} \times \vec{E} = [\mu'_r] \vec{\tilde{H}} \quad (4.24)$$

$$\tilde{\nabla} \times \vec{\tilde{H}} = [\epsilon'_r] \vec{E}. \quad (4.25)$$

4.1.3 Finite-Difference Approximations

Figure 4.1 shows the three-dimensional arrangements of the electric and magnetic field components within a single cell using the Yee grid which was described in Section 3.2.6.

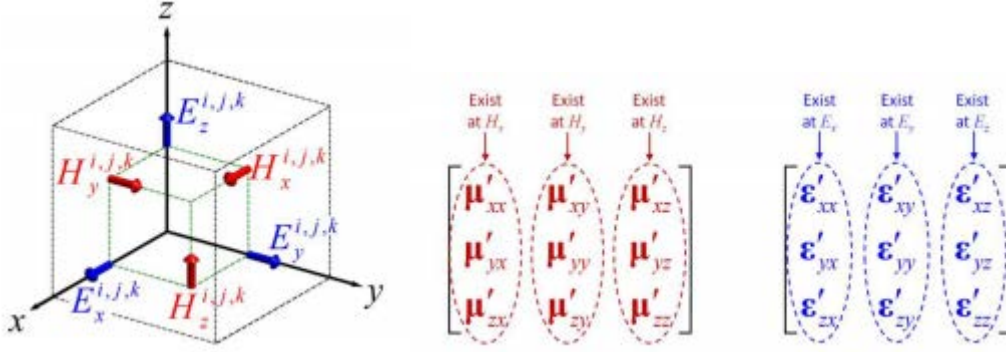


Figure 4.1: Three dimensional Yee grid showing the placement of the field components within a cell of the computational grid as well as the tensor component locations [17].

Expanding Eq. (4.24) into each of its vector components leads to

$$\frac{\partial E_z}{\partial y} - \frac{\partial E_y}{\partial z} = \mu'_{xx} \tilde{H}_x + \mu'_{xy} \tilde{H}_y + \mu'_{xz} \tilde{H}_z \quad (4.26)$$

$$\frac{\partial E_x}{\partial z} - \frac{\partial E_z}{\partial x} = \mu'_{yx} \tilde{H}_x + \mu'_{yy} \tilde{H}_y + \mu'_{yz} \tilde{H}_z \quad (4.27)$$

$$\frac{\partial E_y}{\partial x} - \frac{\partial E_x}{\partial y} = \mu'_{zx} \tilde{H}_x + \mu'_{zy} \tilde{H}_y + \mu'_{zz} \tilde{H}_z. \quad (4.28)$$

Likewise, Eq. (4.25) can be expanded as

$$\frac{\partial \tilde{H}_z}{\partial y} - \frac{\partial \tilde{H}_y}{\partial z} = \epsilon'_{xx} E_x + \epsilon'_{xy} E_y + \epsilon'_{xz} E_z \quad (4.29)$$

$$\frac{\partial \tilde{H}_x}{\partial z} - \frac{\partial \tilde{H}_z}{\partial x} = \epsilon'_{yx} E_x + \epsilon'_{yy} E_y + \epsilon'_{yz} E_z \quad (4.30)$$

$$\frac{\partial \tilde{H}_y}{\partial x} - \frac{\partial \tilde{H}_x}{\partial y} = \epsilon'_{zx} E_x + \epsilon'_{zy} E_y + \epsilon'_{zz} E_z. \quad (4.31)$$

With Eqs. (4.24) and (4.25) fully expanded, the equations (4.26) - (4.31) can be approximated using a centered finite-difference approximation [62]. Referring to Figure 4.1, equation (4.26) is defined at the position of $H_x^{i,j,k}$ in the Yee grid cell. In order to approximate Eq. (4.26) rigorously, the values of \tilde{H}_y and \tilde{H}_z must be determined at the position where the expression is evaluated, which in the case of Eq. (4.26) is the location of $H_x^{i,j,k}$. Similarly, all of the other field values must be evaluated at the positions where the equation being approximated exists. In order to address the discrepancies of having field components staggered throughout the grid the values are interpolated to the position at which the equation is to be evaluated.

Implementing the interpolation approach described above Eqs. (4.26) - (4.28) become

$$\frac{E_z^{i,j,k+1} - E_z^{i,j,k}}{\Delta \tilde{y}} - \frac{E_y^{i,j,k+1} - E_y^{i,j,k}}{\Delta \tilde{z}} = \mu'_{xx} \tilde{H}_x^{i,j,k} + \frac{\mu'_{xy} \tilde{H}_y^{i-1,j,k} + \mu'_{xy} \tilde{H}_y^{i,j,k} + \mu'_{xy} \tilde{H}_y^{i-1,j+1,k} + \mu'_{xy} \tilde{H}_y^{i,j+1,k}}{4} + \frac{\mu'_{xz} \tilde{H}_z^{i,j,k} + \mu'_{xz} \tilde{H}_z^{i-1,j,k} + \mu'_{xz} \tilde{H}_z^{i,j,k+1} + \mu'_{xz} \tilde{H}_z^{i-1,j,k+1}}{4} \quad (4.32)$$

$$\frac{E_x^{i,j,k+1} - E_x^{i,j,k}}{\Delta \tilde{z}} - \frac{E_z^{i+1,j,k} - E_z^{i,j,k}}{\Delta \tilde{x}} = \mu'_{yy} \tilde{H}_y^{i,j,k} + \frac{\mu'_{yx} \tilde{H}_x^{i,j,k} + \mu'_{yx} \tilde{H}_x^{i,j-1,k} + \mu'_{yx} \tilde{H}_x^{i+1,j,k} + \mu'_{yx} \tilde{H}_x^{i+1,j-1,k}}{4} + \frac{\mu'_{yz} \tilde{H}_z^{i,j,k} + \mu'_{yz} \tilde{H}_z^{i,j-1,k} + \mu'_{yz} \tilde{H}_z^{i,j,k+1} + \mu'_{yz} \tilde{H}_z^{i,j-1,k+1}}{4} \quad (4.33)$$

$$\frac{E_y^{i+1,j,k} - E_y^{i,j,k}}{\Delta \tilde{x}} - \frac{E_x^{i,j,k+1} + E_x^{i,j,k}}{\Delta \tilde{y}} = \mu'_{zz} \tilde{H}_z^{i,j,k} + \frac{\mu'_{zx} \tilde{H}_x^{i,j,k} + \mu'_{zx} \tilde{H}_x^{i,j,k-1} + \mu'_{zx} \tilde{H}_x^{i+1,j,k} + \mu'_{zx} \tilde{H}_x^{i+1,j,k-1}}{4} + \frac{\mu'_{zy} \tilde{H}_y^{i,j,k} + \mu'_{zy} \tilde{H}_y^{i,j+1,k} + \mu'_{zy} \tilde{H}_y^{i,j,k-1} + \mu'_{zy} \tilde{H}_y^{i,j+1,k-1}}{4} \quad (4.34)$$

and equations (4.29) - (4.31) become

$$\frac{\tilde{H}_z^{i,j,k} - \tilde{H}_z^{i,j-1,k}}{\Delta \tilde{y}} - \frac{\tilde{H}_y^{i,j,k} - \tilde{H}_y^{i,j,k-1}}{\Delta \tilde{z}} = \epsilon'_{xx} E_x^{i,j,k} + \frac{\epsilon'_{xy} E_y^{i,j,k} + \epsilon'_{xy} E_y^{i,j-1,k} + \epsilon'_{xy} E_y^{i+1,j,k} + \epsilon'_{xy} E_y^{i+1,j-1,k}}{4} + \frac{\epsilon'_{xz} E_z^{i,j,k} + \epsilon'_{xz} E_z^{i,j,k-1} + \epsilon'_{xz} E_z^{i+1,j,k} + \epsilon'_{xz} E_z^{i+1,j,k-1}}{4} \quad (4.35)$$

$$\frac{\tilde{H}_x^{i,j,k} - \tilde{H}_x^{i,j,k-1}}{\Delta \tilde{z}} - \frac{\tilde{H}_z^{i,j,k} - \tilde{H}_z^{i-1,j,k}}{\Delta \tilde{x}} = \epsilon'_{yy} E_y^{i,j,k} + \frac{\epsilon'_{yx} E_x^{i,j,k} + \epsilon'_{yx} E_x^{i,j+1,k} + \epsilon'_{yx} E_x^{i-1,j,k} + \epsilon'_{yx} E_x^{i-1,j+1,k}}{4} + \frac{\epsilon'_{yz} E_z^{i,j,k} + \epsilon'_{yz} E_z^{i,j,k-1} + \epsilon'_{yz} E_z^{i+1,j,k} + \epsilon'_{yz} E_z^{i+1,j,k-1}}{4} \quad (4.36)$$

$$\frac{\tilde{H}_y^{i,j,k} - \tilde{H}_y^{i-1,j,k}}{\Delta\tilde{x}} - \frac{\tilde{H}_x^{i,j,k} - \tilde{H}_x^{i,j-1,k}}{\Delta\tilde{y}} = \varepsilon'_{zz} E_z^{i,j,k} + \frac{\varepsilon'_{zx} E_x^{i,j,k} + \varepsilon'_{zx} E_x^{i,j,k+1} + \varepsilon'_{zx} E_x^{i-1,j,k} + \varepsilon'_{zx} E_x^{i-1,j,k+1}}{4} + \frac{\varepsilon'_{zy} E_y^{i,j,k} + \varepsilon'_{zy} E_y^{i,j,k+1} + \varepsilon'_{zy} E_y^{i,j-1,k} + \varepsilon'_{zy} E_y^{i,j-1,k+1}}{4}. \quad (4.37)$$

4.1.4 Derivation of Matrix Operators

The finite differences in Eqs. (4.32) - (4.37) can be written as matrix operators to perform the derivative approximation point by point throughout the grid. For a computational grid with size $N_x \times N_y \times N_z$ the magnetic field intensity components $\tilde{H}_x^{i,j,k}$, $\tilde{H}_y^{i,j,k}$, $\tilde{H}_z^{i,j,k}$ can be rearranged into column vectors $\tilde{\mathbf{h}}_x$, $\tilde{\mathbf{h}}_y$, $\tilde{\mathbf{h}}_z$ such that [71]

$$\begin{aligned} \tilde{\mathbf{h}}_x &= \begin{bmatrix} \tilde{H}_x^{0,\frac{1}{2},\frac{1}{2}} \\ \tilde{H}_x^{1,\frac{1}{2},\frac{1}{2}} \\ \vdots \\ \tilde{H}_x^{N_x-1,N_y-\frac{1}{2},N_z-\frac{1}{2}} \end{bmatrix} & \tilde{\mathbf{h}}_y &= \begin{bmatrix} \tilde{H}_y^{\frac{1}{2},0,\frac{1}{2}} \\ \tilde{H}_y^{\frac{3}{2},0,\frac{1}{2}} \\ \vdots \\ \tilde{H}_y^{N_x-\frac{1}{2},N_y-1,N_z-\frac{1}{2}} \end{bmatrix}, \\ \tilde{\mathbf{h}}_z &= \begin{bmatrix} \tilde{H}_z^{\frac{1}{2},\frac{1}{2},0} \\ \tilde{H}_z^{\frac{3}{2},\frac{1}{2},0} \\ \vdots \\ \tilde{H}_z^{N_x-\frac{1}{2},N_y-\frac{1}{2},N_z-1} \end{bmatrix} \end{aligned} \quad (4.38)$$

and the electric field intensity components $E_x^{i,j,k}$, $E_y^{i,j,k}$, $E_z^{i,j,k}$ can be rearranged into column vectors \mathbf{e}_x , \mathbf{e}_y , \mathbf{e}_z as

$$\begin{aligned}
\mathbf{e}_x &= \begin{bmatrix} E_x^{1,0,0} \\ E_x^{3,0,0} \\ \vdots \\ E_x^{N_x-\frac{1}{2},N_y-1,N_z-1} \end{bmatrix} & \mathbf{e}_y &= \begin{bmatrix} E_y^{0,\frac{1}{2},0} \\ E_y^{1,\frac{1}{2},0} \\ \vdots \\ E_y^{N_x-1,N_y-\frac{1}{2},N_z-1} \end{bmatrix} \\
\mathbf{e}_z &= \begin{bmatrix} E_z^{0,0,\frac{1}{2}} \\ E_z^{1,0,\frac{1}{2}} \\ \vdots \\ E_z^{N_x-1,N_y-1,N_z-\frac{1}{2}} \end{bmatrix}
\end{aligned} \tag{4.39}$$

With the rearrangement of the field components into Eqs. (4.38) and (4.39), the finite difference approximations can be written as matrices to calculate the derivative at each point in the grid. Consider a partial differential approximation in the one dimension as

$$\left. \frac{\partial E}{\partial x} \right|_{i-\frac{1}{2}} \cong \frac{E_i - E_{i-1}}{\Delta x} . \tag{4.40}$$

The expression shown in Eq. (4.40) can be expanded into a system of equations given as

$$\left. \frac{\partial E}{\partial x} \right|_{i-\frac{1}{2}} \cong \begin{bmatrix} \frac{\partial E_{1.5}}{\partial x} \\ \frac{\partial E_{2.5}}{\partial x} \\ \frac{\partial E_{3.5}}{\partial x} \\ \frac{\partial E_{4.5}}{\partial x} \\ \frac{\partial E_{5.5}}{\partial x} \end{bmatrix} = \begin{cases} \frac{E_2 - E_1}{\Delta x} \\ \frac{E_3 - E_2}{\Delta x} \\ \frac{E_4 - E_3}{\Delta x} \\ \frac{E_5 - E_4}{\Delta x} \\ \frac{E_6 - E_5}{\Delta x} \end{cases} . \tag{4.41}$$

The system of equations given by Eq. (4.41), a matrix equation can be formed such as

$$\left. \frac{\partial E}{\partial x} \right|_{i-\frac{1}{2}} \cong \begin{bmatrix} \frac{\partial E_{1.5}}{\partial x} \\ \frac{\partial E_{2.5}}{\partial x} \\ \frac{\partial E_{3.5}}{\partial x} \\ \frac{\partial E_{4.5}}{\partial x} \\ \frac{\partial E_{5.5}}{\partial x} \end{bmatrix} = \frac{1}{\Delta x} \begin{bmatrix} -1 & 1 & & & \\ & -1 & 1 & & \\ & & -1 & 1 & \\ & & & -1 & 1 \\ & & & & -1 \end{bmatrix} \begin{bmatrix} E_1 \\ E_2 \\ E_3 \\ E_4 \\ E_5 \end{bmatrix}. \quad (4.42)$$

For any finite-difference expression it is necessary to address the boundaries of the domain being evaluated. In the system of equations shown in Eq. (4.41) the values of E_0 and E_6 do not exist within the computational domain. Boundary conditions determine how these values are treated in the finite difference approximations. The most common boundary conditions are Dirichlet and Neumann boundary conditions. Dirichlet boundaries are boundaries in which the unknown quantities outside of the grid are set to a constant quantity, typically zero, while Neumann boundary conditions are boundaries in which the derivatives of the quantities outside of the grid are set to a constant value [36, 73].

For a $2 \times 2 \times 2$ grid in the finite-difference of E with respect to \tilde{x} with Dirichlet boundary conditions is

$$\mathbf{D}_x^e \mathbf{E} = \frac{1}{\Delta \tilde{x}} \begin{bmatrix} -1 & 1 & & & & \\ & -1 & 0 & & & \\ & & -1 & 1 & & \\ & & & -1 & 0 & \\ & & & & -1 & 1 \\ & & & & & -1 & 0 \\ & & & & & & -1 & 1 \\ & & & & & & & -1 \end{bmatrix} \begin{bmatrix} E^{1,1,1} \\ E^{2,1,1} \\ E^{1,2,1} \\ E^{2,2,1} \\ E^{1,1,2} \\ E^{2,1,2} \\ E^{1,2,2} \\ E^{2,2,2} \end{bmatrix}, \quad (4.43)$$

the derivative of E with respect to \tilde{y} is

$$\mathbf{D}_y^e \mathbf{E} = \frac{1}{\Delta \tilde{y}} \begin{bmatrix} -1 & & & & & & & \\ & 1 & & & & & & \\ & & -1 & & & & & \\ & & & 1 & & & & \\ & & & & -1 & & & \\ & & & & & 0 & & \\ & & & & & & -1 & \\ & & & & & & & 0 & \\ & & & & & & & & -1 & \\ & & & & & & & & & 1 & \\ & & & & & & & & & & -1 & \\ & & & & & & & & & & & -1 \end{bmatrix} \begin{bmatrix} E^{1,1,1} \\ E^{2,1,1} \\ E^{1,2,1} \\ E^{2,2,1} \\ E^{1,1,2} \\ E^{2,1,2} \\ E^{1,2,2} \\ E^{2,2,2} \end{bmatrix}, \quad (4.44)$$

and the derivative of E with respect to z is

$$\mathbf{D}_z^e \mathbf{E} = \frac{1}{\Delta \tilde{z}} \begin{bmatrix} -1 & & & & & & & \\ & 1 & & & & & & \\ & & -1 & & & & & \\ & & & 1 & & & & \\ & & & & -1 & & & \\ & & & & & 1 & & \\ & & & & & & -1 & \\ & & & & & & & 1 & \\ & & & & & & & & -1 & \\ & & & & & & & & & 1 & \\ & & & & & & & & & & -1 \end{bmatrix} \begin{bmatrix} E^{1,1,1} \\ E^{2,1,1} \\ E^{1,2,1} \\ E^{2,2,1} \\ E^{1,1,2} \\ E^{2,1,2} \\ E^{1,2,2} \\ E^{2,2,2} \end{bmatrix}. \quad (4.45)$$

The matrices that calculate the derivatives of the H field are the negative Hermitian transpose of those of the electric field derivatives [71] as given by

$$\mathbf{D}_x^h = -(\mathbf{D}_x^e)^H \quad \mathbf{D}_y^h = -(\mathbf{D}_y^e)^H \quad \mathbf{D}_z^h = -(\mathbf{D}_z^e)^H. \quad (4.46)$$

The permittivity and permeability tensors are rearranged such that they multiply point-by-point throughout the grid with the magnetic field column vector or electric field column vector. This point-by-point multiplication is performed by expanding each tensor component into a column vector and the placing that vector along the diagonal of a sparse matrix of size $N_x N_y N_z \times N_x N_y N_z$ [17, 71].

$$\begin{aligned} \boldsymbol{\mu}_{xx} &= \text{diag}[\mu_{xx} s_x^{-1} s_y s_z] & \boldsymbol{\mu}_{xy} &= \text{diag}[\mu_{xy} s_x s_y^{-1} s_z] & \boldsymbol{\mu}_{xz} &= \text{diag}[\mu_{xz} s_x s_y s_z^{-1}] \\ \boldsymbol{\mu}_{yx} &= \text{diag}[\mu_{yx} s_x^{-1} s_y s_z] & \boldsymbol{\mu}_{yy} &= \text{diag}[\mu_{yy} s_x s_y^{-1} s_z] & \boldsymbol{\mu}_{yz} &= \text{diag}[\mu_{yz} s_x s_y s_z^{-1}] \\ \boldsymbol{\mu}_{zx} &= \text{diag}[\mu_{zx} s_x^{-1} s_y s_z] & \boldsymbol{\mu}_{zy} &= \text{diag}[\mu_{zy} s_x s_y^{-1} s_z] & \boldsymbol{\mu}_{zz} &= \text{diag}[\mu_{zz} s_x s_y s_z^{-1}] \end{aligned} \quad (4.47)$$

$$\begin{aligned}
\boldsymbol{\epsilon}_{xx} &= \text{diag}[\epsilon_{xx} s_x^{-1} s_y s_z] & \boldsymbol{\epsilon}_{xy} &= \text{diag}[\epsilon_{xy} s_x s_y^{-1} s_z] & \boldsymbol{\epsilon}_{xz} &= \text{diag}[\epsilon_{xz} s_x s_y s_z^{-1}] \\
\boldsymbol{\epsilon}_{yx} &= \text{diag}[\epsilon_{yx} s_x^{-1} s_y s_z] & \boldsymbol{\epsilon}_{yy} &= \text{diag}[\epsilon_{yy} s_x s_y^{-1} s_z] & \boldsymbol{\epsilon}_{yz} &= \text{diag}[\epsilon_{yz} s_x s_y s_z^{-1}] \\
\boldsymbol{\epsilon}_{zx} &= \text{diag}[\epsilon_{zx} s_x^{-1} s_y s_z] & \boldsymbol{\epsilon}_{zy} &= \text{diag}[\epsilon_{zy} s_x s_y^{-1} s_z] & \boldsymbol{\epsilon}_{zz} &= \text{diag}[\epsilon_{zz} s_x s_y s_z^{-1}]
\end{aligned} \tag{4.48}$$

The interpolation operations in Eqs. (4.32) - (4.37) can be made into matrix operations in similar way to the derivative operators. Consider the term

$$\frac{\mu_{xy}'^{i-1,j,k} \tilde{H}_y^{i-1,j,k} + \mu_{xy}'^{i,j,k} \tilde{H}_y^{i,j,k} + \mu_{xy}'^{i-1,j+1,k} \tilde{H}_y^{i-1,j+1,k} + \mu_{xy}'^{i,j+1,k} \tilde{H}_y^{i,j+1,k}}{4}. \tag{4.49}$$

Evaluating Eq. (4.49) point-by-point on a $2 \times 2 \times 2$ grid leads to

$$\begin{aligned}
& \left\{ \begin{aligned} & \frac{1}{4} (\mu_{xy}'^{0,1,1} \tilde{H}_y^{0,1,1} + \mu_{xy}'^{1,1,1} \tilde{H}_y^{1,1,1} + \mu_{xy}'^{0,2,1} \tilde{H}_y^{0,2,1} + \mu_{xy}'^{1,2,1} \tilde{H}_y^{1,2,1}) \\ & \frac{1}{4} (\mu_{xy}'^{1,1,1} \tilde{H}_y^{1,1,1} + \mu_{xy}'^{2,1,1} \tilde{H}_y^{2,1,1} + \mu_{xy}'^{1,2,1} \tilde{H}_y^{1,2,1} + \mu_{xy}'^{2,2,1} \tilde{H}_y^{2,2,1}) \\ & \frac{1}{4} (\mu_{xy}'^{0,2,1} \tilde{H}_y^{0,2,1} + \mu_{xy}'^{1,2,1} \tilde{H}_y^{1,2,1} + \mu_{xy}'^{0,3,1} \tilde{H}_y^{0,3,1} + \mu_{xy}'^{1,3,1} \tilde{H}_y^{1,3,1}) \\ & \frac{1}{4} (\mu_{xy}'^{1,2,1} \tilde{H}_y^{1,2,1} + \mu_{xy}'^{2,2,1} \tilde{H}_y^{2,2,1} + \mu_{xy}'^{1,3,1} \tilde{H}_y^{1,3,1} + \mu_{xy}'^{2,3,1} \tilde{H}_y^{2,3,1}) \\ & \frac{1}{4} (\mu_{xy}'^{0,1,2} \tilde{H}_y^{0,1,2} + \mu_{xy}'^{1,1,2} \tilde{H}_y^{1,1,2} + \mu_{xy}'^{0,2,2} \tilde{H}_y^{0,2,2} + \mu_{xy}'^{1,2,2} \tilde{H}_y^{1,2,2}) \\ & \frac{1}{4} (\mu_{xy}'^{1,1,2} \tilde{H}_y^{1,1,2} + \mu_{xy}'^{2,1,2} \tilde{H}_y^{2,1,2} + \mu_{xy}'^{1,2,2} \tilde{H}_y^{1,2,2} + \mu_{xy}'^{2,2,2} \tilde{H}_y^{2,2,2}) \\ & \frac{1}{4} (\mu_{xy}'^{0,2,2} \tilde{H}_y^{0,2,2} + \mu_{xy}'^{1,2,2} \tilde{H}_y^{1,2,2} + \mu_{xy}'^{0,3,2} \tilde{H}_y^{0,3,2} + \mu_{xy}'^{1,3,2} \tilde{H}_y^{1,3,2}) \\ & \frac{1}{4} (\mu_{xy}'^{1,2,2} \tilde{H}_y^{1,2,2} + \mu_{xy}'^{2,2,2} \tilde{H}_y^{2,2,2} + \mu_{xy}'^{1,3,2} \tilde{H}_y^{1,3,2} + \mu_{xy}'^{2,3,2} \tilde{H}_y^{2,3,2}) \end{aligned} \right. \tag{4.50}
\end{aligned}$$

Writing Eq. (4.50) using the column vector components given in Eqs. (4.38) and (4.39) gives

$$\mathbf{R}_x^- \mathbf{R}_y^+ \boldsymbol{\mu}_{xy} \tilde{\mathbf{h}}_y = \frac{1}{4} \begin{bmatrix} 1 & & & & & & & \\ & 1 & & & & & & \\ & & 1 & & & & & \\ & & & 1 & & & & \\ & & & & 1 & & & \\ & & & & & 1 & & \\ & & & & & & 1 & \\ & & & & & & & 1 \end{bmatrix} \begin{bmatrix} \mu_{xy}'^{1,1,1} \tilde{H}_y^{1,1,1} \\ \mu_{xy}'^{2,1,1} \tilde{H}_y^{2,1,1} \\ \mu_{xy}'^{1,2,1} \tilde{H}_y^{1,2,1} \\ \mu_{xy}'^{2,2,1} \tilde{H}_y^{2,2,1} \\ \mu_{xy}'^{1,1,2} \tilde{H}_y^{1,1,2} \\ \mu_{xy}'^{2,1,2} \tilde{H}_y^{2,1,2} \\ \mu_{xy}'^{1,2,2} \tilde{H}_y^{1,2,2} \\ \mu_{xy}'^{2,2,2} \tilde{H}_y^{2,2,2} \end{bmatrix}. \tag{4.51}$$

Dirichlet boundary conditions are for the values which are outside of the grid. The expression given in Eq. (4.51) can be expanded into two interpolation matrices \mathbf{R}_x^- and \mathbf{R}_y^+ which perform interpolation in the negative x and positive y direction respectively. These interpolation matrices are given as

$$\mathbf{R}_x^- = \frac{1}{2} \begin{bmatrix} 1 & & & & & & & \\ & 1 & & & & & & \\ & & 0 & 1 & & & & \\ & & & 1 & 1 & & & \\ & & & & 0 & 1 & & \\ & & & & & 1 & 1 & \\ & & & & & & 0 & 1 \\ & & & & & & & 1 & 1 \end{bmatrix} \quad (4.52)$$

$$\mathbf{R}_y^+ = \frac{1}{2} \begin{bmatrix} 1 & & & & & & & \\ & 1 & & & & & & \\ & & 1 & & 1 & & & \\ & & & 1 & & 0 & & \\ & & & & 1 & & 0 & \\ & & & & & 1 & & 1 \\ & & & & & & 1 & 1 \\ & & & & & & & 1 & 1 \\ & & & & & & & & 1 \end{bmatrix} \quad (4.53)$$

The interpolation matrices for the negative going terms are the Hermitian conjugates of Eqs. (4.52) and (4.53) given by

$$\mathbf{R}_i^+ = (\mathbf{R}_i^-)^H. \quad (4.54)$$

4.1.5 Matrix Form of Maxwell's Equations

Evaluation of Eqs. (4.32) - (4.37) is done point by point throughout the entire grid. This can be done using matrices to express these equations as a system of linear equations. Writing Eqs. (4.32) - (4.37) in matrix form leads to

$$\mathbf{D}_y^e \mathbf{e}_z - \mathbf{D}_z^e \mathbf{e}_y = \mu'_{xx} \tilde{\mathbf{h}}_x + \mathbf{R}_x^- \mathbf{R}_y^+ \mu'_{xy} \tilde{\mathbf{h}}_y + \mathbf{R}_x^- \mathbf{R}_z^+ \mu'_{xz} \tilde{\mathbf{h}}_z \quad (4.55)$$

$$\mathbf{D}_z^e \mathbf{e}_x - \mathbf{D}_x^e \mathbf{e}_z = \mathbf{R}_y^- \mathbf{R}_x^+ \mu'_{yx} \tilde{\mathbf{h}}_x + \mu'_{yy} \tilde{\mathbf{h}}_y + \mathbf{R}_y^- \mathbf{R}_z^+ \mu'_{yz} \tilde{\mathbf{h}}_z \quad (4.56)$$

$$\mathbf{D}_x^e \mathbf{e}_y - \mathbf{D}_y^e \mathbf{e}_x = \mathbf{R}_z^- \mathbf{R}_x^+ \mu'_{zx} \tilde{\mathbf{h}}_x + \mathbf{R}_z^- \mathbf{R}_y^+ \mu'_{zy} \tilde{\mathbf{h}}_y + \mu'_{zz} \tilde{\mathbf{h}}_z \quad (4.57)$$

$$\mathbf{D}_y^h \tilde{\mathbf{h}}_z - \mathbf{D}_z^h \tilde{\mathbf{h}}_y = \epsilon'_{xx} \mathbf{e}_x + \mathbf{R}_x^- \mathbf{R}_y^+ \epsilon'_{xy} \mathbf{e}_y + \mathbf{R}_x^- \mathbf{R}_z^+ \epsilon'_{xz} \mathbf{e}_z \quad (4.58)$$

$$\mathbf{D}_z^h \tilde{\mathbf{h}}_x - \mathbf{D}_x^h \tilde{\mathbf{h}}_z = \mathbf{R}_y^+ \mathbf{R}_x^- \epsilon'_{yx} \mathbf{e}_x + \epsilon'_{yy} \mathbf{e}_y + \mathbf{R}_y^+ \mathbf{R}_z^- \epsilon'_{yz} \mathbf{e}_z. \quad (4.59)$$

$$\mathbf{D}_x^h \tilde{\mathbf{h}}_y - \mathbf{D}_y^h \tilde{\mathbf{h}}_x = \mathbf{R}_z^+ \mathbf{R}_x^- \boldsymbol{\varepsilon}'_{zx} \tilde{\mathbf{h}}_x + \mathbf{R}_z^+ \mathbf{R}_y^- \boldsymbol{\varepsilon}'_{zy} \tilde{\mathbf{h}}_y + \boldsymbol{\varepsilon}'_{zz} \tilde{\mathbf{h}}_z \quad (4.60)$$

The lower case terms $\tilde{\mathbf{h}}$ and \mathbf{e} are column vectors representing the normalized magnetic field intensity and electric field intensity respectively. They are formed by taking the field components at each point in the grid and placing them into a vector [71]. The finite difference calculations are encapsulated in the matrix derivative operators \mathbf{D}_y^e , \mathbf{D}_x^e , \mathbf{D}_z^e and the corresponding matrices for the magnetic field derivatives. Due to the staggered arrangement of field components on the Yee grid each matrix operator is different. The superscript of the matrix derivative operator designates the type of field (E or H) that the derivative is operating on, while the subscript designates which variable the derivative is with respect to. The interpolation of fields and material parameters in Eqs. (4.32) - (4.37) is performed by the \mathbf{R}^- and \mathbf{R}^+ matrices in Eqs. (4.55) - (4.59).

The product of the interpolation matrices and tensor component matrices can be rewritten using block matrices as

$$[\boldsymbol{\mu}_r''] = \begin{bmatrix} \mu''_{xx} & \mu''_{xy} & \mu''_{xz} \\ \mu''_{yx} & \mu''_{yy} & \mu''_{yz} \\ \mu''_{zx} & \mu''_{zy} & \mu''_{zz} \end{bmatrix} = \begin{bmatrix} \mu'_{xx} & \mathbf{R}_x^- \mathbf{R}_y^+ \mu'_{xy} & \mathbf{R}_x^- \mathbf{R}_z^+ \mu'_{xz} \\ \mathbf{R}_y^- \mathbf{R}_x^+ \mu'_{yx} & \mu'_{yy} & \mathbf{R}_y^- \mathbf{R}_z^+ \mu'_{yz} \\ \mathbf{R}_z^- \mathbf{R}_x^+ \mu'_{zx} & \mathbf{R}_z^- \mathbf{R}_y^+ \mu'_{zy} & \mu'_{zz} \end{bmatrix} \quad (4.61)$$

$$[\boldsymbol{\varepsilon}_r''] = \begin{bmatrix} \varepsilon''_{xx} & \varepsilon''_{xy} & \varepsilon''_{xz} \\ \varepsilon''_{yx} & \varepsilon''_{yy} & \varepsilon''_{yz} \\ \varepsilon''_{zx} & \varepsilon''_{zy} & \varepsilon''_{zz} \end{bmatrix} = \begin{bmatrix} \varepsilon'_{xx} & \mathbf{R}_x^+ \mathbf{R}_y^- \varepsilon'_{xy} & \mathbf{R}_x^+ \mathbf{R}_z^- \varepsilon'_{xz} \\ \mathbf{R}_y^+ \mathbf{R}_x^- \varepsilon'_{yx} & \varepsilon'_{yy} & \mathbf{R}_y^+ \mathbf{R}_z^- \varepsilon'_{yz} \\ \mathbf{R}_z^+ \mathbf{R}_x^- \varepsilon'_{zx} & \mathbf{R}_z^+ \mathbf{R}_y^- \varepsilon'_{zy} & \varepsilon'_{zz} \end{bmatrix} \quad (4.62)$$

Using the above block matrix notation Maxwell's curl equations can be written as given in Ref. [17]

$$\mathbf{C}^e \tilde{\mathbf{e}} = [\boldsymbol{\mu}_r''] \tilde{\mathbf{h}} \quad (4.63)$$

$$\mathbf{C}^h \tilde{\mathbf{h}} = [\boldsymbol{\varepsilon}_r''] \tilde{\mathbf{e}} \quad (4.64)$$

where

$$\mathbf{C}^e = \begin{bmatrix} \mathbf{0} & -\mathbf{D}_z^e & \mathbf{D}_y^e \\ \mathbf{D}_z^e & \mathbf{0} & -\mathbf{D}_x^e \\ -\mathbf{D}_y^e & \mathbf{D}_x^e & \mathbf{0} \end{bmatrix} \quad \mathbf{C}^h = \begin{bmatrix} \mathbf{0} & -\mathbf{D}_z^h & \mathbf{D}_y^h \\ \mathbf{D}_z^h & \mathbf{0} & -\mathbf{D}_x^h \\ -\mathbf{D}_y^h & \mathbf{D}_x^h & \mathbf{0} \end{bmatrix} \quad (4.65)$$

and

$$\tilde{\mathbf{e}} = \begin{bmatrix} \mathbf{e}_x \\ \mathbf{e}_y \\ \mathbf{e}_z \end{bmatrix} \quad \tilde{\mathbf{h}} = \begin{bmatrix} \tilde{\mathbf{h}}_x \\ \tilde{\mathbf{h}}_y \\ \tilde{\mathbf{h}}_z \end{bmatrix}. \quad (4.66)$$

4.1.6 Matrix Wave Equation

Solving Eq. (4.63) for $\vec{\mathbf{h}}$ leads to

$$\vec{\mathbf{h}} = [\boldsymbol{\mu}_r'']^{-1} \mathbf{C}^e \vec{\mathbf{e}} \quad (4.67)$$

Substituting Eq. (4.67) into Eq. (4.64) gives

$$\mathbf{C}^h [\boldsymbol{\mu}_r'']^{-1} \mathbf{C}^e \vec{\mathbf{e}} = [\boldsymbol{\epsilon}_r''] \vec{\mathbf{e}} \quad (4.68)$$

This expression is the matrix wave equation in terms of the electric field intensity [17]. Factoring $\vec{\mathbf{e}}$ from Eq. (4.68) gives the expression

$$\mathbf{A}_e \vec{\mathbf{e}} = 0 \quad (4.69)$$

where

$$\mathbf{A}_e = \mathbf{C}^h [\boldsymbol{\mu}_r'']^{-1} \mathbf{C}^e - [\boldsymbol{\epsilon}_r''] \quad (4.70)$$

Similarly, the wave equation in terms of the magnetic field can be derived as

$$\mathbf{A}_h \vec{\mathbf{h}} = 0 \quad (4.71)$$

with

$$\mathbf{A}_h = \mathbf{C}^e [\boldsymbol{\epsilon}_r'']^{-1} \mathbf{C}^h - [\boldsymbol{\mu}_r''] \quad (4.72)$$

The wave equations above provide only a trivial solution when solved for either the electric field intensity or the magnetic field intensity. However, a source term \mathbf{b} can be incorporated to into either Eq. (4.69) or Eq. (4.71) to yield meaningful system of linear equations of the form

$$\mathbf{A}\mathbf{x} = \mathbf{b} \quad (4.73)$$

which can be solved as $\mathbf{x} = \mathbf{A}^{-1}\mathbf{b}$ using traditional matrix algebra techniques for sparse matrices such as LU decomposition [74] or the conjugate gradient method [75].

4.2 TOTAL-FIELD/SCATTERED-FIELD FORMULATION

In order to create the source term in Eq. (4.73), the *Total-Field/Scattered-Field* (TF/SF), mentioned previously in Chapter 3, is used [71]. In this method, the problem space is divided into two regions: the Total-Field region which consists of both the source field and the scattered waves, and the Scattered-Field region which contains only the scattered energy. To implement this source the source, fields are defined at every point on the Yee grid and reshaped into column vectors as

$$\mathbf{e}_{x,\text{src}} = \begin{bmatrix} e_{x,\text{src}}^{1,1,1} \\ e_{x,\text{src}}^{1,1,2} \\ \vdots \\ e_{x,\text{src}}^{N_x, N_y, N_z} \end{bmatrix} \quad \mathbf{e}_{y,\text{src}} = \begin{bmatrix} e_{y,\text{src}}^{1,1,1} \\ e_{y,\text{src}}^{1,1,2} \\ \vdots \\ e_{y,\text{src}}^{N_x, N_y, N_z} \end{bmatrix} \quad \mathbf{e}_{z,\text{src}} = \begin{bmatrix} e_{z,\text{src}}^{1,1,1} \\ e_{z,\text{src}}^{1,1,2} \\ \vdots \\ e_{z,\text{src}}^{N_x, N_y, N_z} \end{bmatrix} \quad (4.74)$$

These column vectors are then placed into a single column vector given by

$$\vec{\mathbf{e}}_{\text{src}} = \begin{bmatrix} \mathbf{e}_{x,\text{src}} \\ \mathbf{e}_{y,\text{src}} \\ \mathbf{e}_{z,\text{src}} \end{bmatrix}. \quad (4.75)$$

In order to separate the TF region and SF region a mask function $Q(x,y)$ is introduced which identifies the scattered field region. It is created by placing 1's on the grid in the positions where the SF exists and placing 0's in the positions where the TF exists. The resulting array is placed along the center diagonal of a sparse matrix [71] as

$$\mathbf{Q} = \text{diag}[Q(x, y)]. \quad (4.76)$$

In order to simulate anisotropic devices a separate Q matrix is necessary for each component of the source and the three resulting diagonal sparse matrices as placed into a block matrix [17]

$$\mathbf{Q} = \begin{bmatrix} \mathbf{Q}_x & \mathbf{0} & \mathbf{0} \\ \mathbf{0} & \mathbf{Q}_y & \mathbf{0} \\ \mathbf{0} & \mathbf{0} & \mathbf{Q}_z \end{bmatrix} \quad (4.77)$$

Defining two terms

$$\vec{\mathbf{e}}_{\text{SF}} = \mathbf{Q} \vec{\mathbf{e}}_{\text{src}} \quad (4.78)$$

$$\vec{\mathbf{e}}_{\text{TF}} = (\mathbf{I} - \mathbf{Q}) \vec{\mathbf{e}}_{\text{src}} \quad (4.79)$$

it is necessary to modify the matrix wave equation (4.69) in order to remove source terms from the SF region and to add the source terms to the TF region. The terms $\mathbf{A}_e \vec{\mathbf{e}}_{\text{TF}}$ must be subtracted from the SF region, therefore the equation $\mathbf{Q} \mathbf{A}_e \vec{\mathbf{e}}_{\text{TF}}$ is subtracted from Eq. (4.69). Also, the terms $\mathbf{A}_e \vec{\mathbf{e}}_{\text{SF}}$ must be added to the TF region, therefore the equation $(\mathbf{I} - \mathbf{Q}) \mathbf{A}_e \vec{\mathbf{e}}_{\text{SF}}$ is added to Eq. (4.69). The result of these corrections to the matrix wave equation to correct for the effect of the TF/SF implementation is given by [71]

$$\mathbf{A}_e \vec{\mathbf{e}} - \mathbf{Q} \mathbf{A}_e \vec{\mathbf{e}}_{\text{TF}} + (\mathbf{I} - \mathbf{Q}) \mathbf{A}_e \vec{\mathbf{e}}_{\text{SF}} = 0 \quad (4.80)$$

Rewriting Eq. (4.80) in the form $\mathbf{Ax}=\mathbf{b}$, the source term \mathbf{b} is

$$\mathbf{b} = \mathbf{QA}_e \vec{\mathbf{e}}_{\text{TF}} - (\mathbf{I} - \mathbf{Q}) \mathbf{A}_e \vec{\mathbf{e}}_{\text{SF}} \quad (4.81)$$

Substituting Eqs. (4.78) and (4.79) into Eq. (4.81) allows \mathbf{b} to be expressed in terms of only \mathbf{A} , \mathbf{Q} , and $\vec{\mathbf{e}}_{\text{src}}$ [71]

$$\mathbf{b} = \mathbf{QA}_e (\mathbf{I} - \mathbf{Q}) \vec{\mathbf{e}}_{\text{src}} - (\mathbf{I} - \mathbf{Q}) \mathbf{A}_e \mathbf{Q} \vec{\mathbf{e}}_{\text{src}} \quad (4.82)$$

Simplifying Eq. (4.82) leads to

$$\mathbf{b} = (\mathbf{QA}_e - \mathbf{A}_e \mathbf{Q}) \vec{\mathbf{e}}_{\text{src}}. \quad (4.83)$$

4.3 IMPROVED ANISOTROPIC FINITE-DIFFERENCE FREQUENCY-DOMAIN

Electromagnetic simulation of TO devices can be performed using the AFDFD method, which is described in detail in Ref. [17]. The key matrix equation to be solved in the conventional AFDFD is

$$\left(\mathbf{C}^h [\boldsymbol{\mu}_r]^{-1} \mathbf{C}^e - [\boldsymbol{\epsilon}_r] \right) \vec{\mathbf{e}} = \mathbf{0}. \quad (4.84)$$

where \mathbf{C}^h and \mathbf{C}^e are the curl operator matrices for the magnetic field intensity and electric field intensity respectively, $[\boldsymbol{\mu}_r]$ is the permeability tensor, and $[\boldsymbol{\epsilon}_r]$ is the permittivity tensor as described in detail in Ref. [17]. When simulating devices with magnetically anisotropic materials, calculating the matrix inverse of the permeability tensor is very slow and numerically inefficient. To mitigate this, Eq. (4.84) is instead solved using the impermeability matrix $[\boldsymbol{\Psi}]$.

$$\left(\mathbf{C}^h [\boldsymbol{\Psi}] \mathbf{C}^e - [\boldsymbol{\epsilon}_r] \right) \vec{\mathbf{e}} = \mathbf{0} \quad (4.85)$$

$$[\boldsymbol{\Psi}] = [\boldsymbol{\mu}_r]^{-1} \quad (4.86)$$

To calculate $[\boldsymbol{\Psi}]$ most efficiently, the elements are calculated when they are still functions stored in arrays and not yet diagonal matrices. In this context, we have

$$\begin{aligned} [\boldsymbol{\Psi}(i, j, k)] &= \begin{bmatrix} \psi_{xx}(i, j, k) & \psi_{xy}(i, j, k) & \psi_{xz}(i, j, k) \\ \psi_{yx}(i, j, k) & \psi_{yy}(i, j, k) & \psi_{yz}(i, j, k) \\ \psi_{zx}(i, j, k) & \psi_{zy}(i, j, k) & \psi_{zz}(i, j, k) \end{bmatrix} \\ &= \begin{bmatrix} \mu_{xx}(i, j, k) & \mu_{xy}(i, j, k) & \mu_{xz}(i, j, k) \\ \mu_{yx}(i, j, k) & \mu_{yy}(i, j, k) & \mu_{yz}(i, j, k) \\ \mu_{zx}(i, j, k) & \mu_{zy}(i, j, k) & \mu_{zz}(i, j, k) \end{bmatrix}^{-1}. \end{aligned} \quad (4.87)$$

The elements of $[\psi(i, j, k)]$ are derived from the tensor $[\mu_r(i, j, k)]$ by calculating the matrix inverse symbolically.

$$[\psi(i, j, k)] = \frac{\begin{bmatrix} \mu_{yy}\mu_{zz} - \mu_{yz}\mu_{zy} & \mu_{xz}\mu_{zy} - \mu_{xy}\mu_{zz} & \mu_{xy}\mu_{yz} - \mu_{xz}\mu_{yy} \\ \mu_{yz}\mu_{zx} - \mu_{yx}\mu_{zz} & \mu_{xx}\mu_{zz} - \mu_{xz}\mu_{zx} & \mu_{xz}\mu_{yx} - \mu_{xx}\mu_{yz} \\ \mu_{yx}\mu_{zy} - \mu_{yy}\mu_{zx} & \mu_{xy}\mu_{zx} - \mu_{xx}\mu_{zy} & \mu_{xx}\mu_{yy} - \mu_{xy}\mu_{yx} \end{bmatrix}}{\mu_{xx}\mu_{yy}\mu_{zz} - \mu_{xx}\mu_{yz}\mu_{zy} - \mu_{xz}\mu_{yy}\mu_{zx} - \mu_{xy}\mu_{yx}\mu_{zz} + \mu_{xy}\mu_{yz}\mu_{zx} + \mu_{xz}\mu_{yx}\mu_{zy}} \quad (4.88)$$

For brevity, the dependence on the array indices i, j , and k have been dropped from these equations.

All of these calculations are performed point-by-point on arrays instead of with matrices. After the elements of $[\psi(i, j, k)]$ are calculated, they are reshaped into diagonal matrices and assembled into the overall impermeability matrix as follows.

$$[\Psi] = \begin{bmatrix} \Psi_{xx} & \Psi_{xy} & \Psi_{xz} \\ \Psi_{yx} & \Psi_{yy} & \Psi_{yz} \\ \Psi_{zx} & \Psi_{zy} & \Psi_{zz} \end{bmatrix} \quad (4.89)$$

where $\Psi_{mn} = \text{diag}\{\psi_{mn}(i, j, k)\}$.

Using the impermeability tensor rather than the permeability tensor to solve the wave equation in Eq. (4.85) decreased the time required to solve a two dimensional AFDFD simulation greatly. Figure 4.2 shows the performance of AFDFD on a 96 GB computer using the permeability tensor and the impermeability tensor. The memory efficiency of the methods, while not shown in the figure, is also a great benefit of the impermeability tensor formulation. The simulation of an anisotropic slab with a grid resolution (λ_0 / dx) of greater than 22 was not possible using the permeability tensor method because the machine ran out of memory constructing the wave equation. Most device reach convergence at a grid resolution of about 30-40 cells per free-space wavelength. In order to determine the efficiency at 40 cells the curve for the permeability tensor formulation was extrapolated using a polynomial curve fit. At a grid resolution of 40 the benchmark using the permeability tensor would take over 500 times as long to and the impermeability tensor.

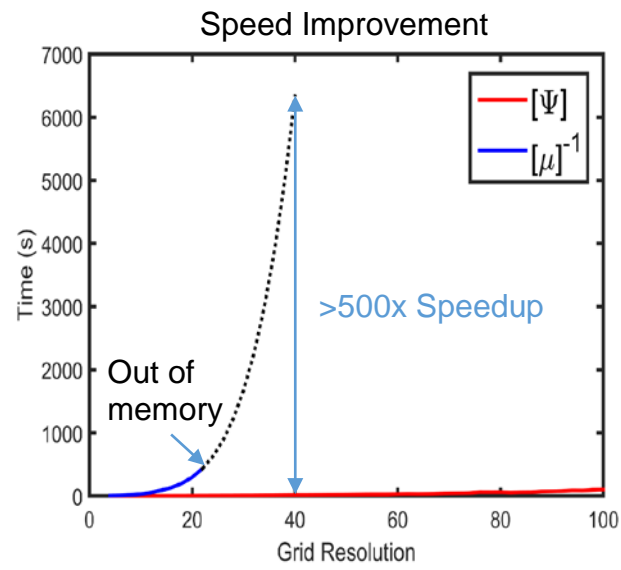


Figure 4.2: Simulation time for AFDFD using the impermeability tensor versus the permeability tensor

Chapter 5: Design of Arbitrary Transformation Optics Devices

5.1 INTRODUCTION

Transformation optics is a design methodology that allows electromagnetic fields to be controlled through spatial transforms [1]. The most well-known example is the cylindrical electromagnetic cloak described in Ref. [18]. Their device used a closed-form expression for the spatial transform, but closed-form expressions are highly limited in the range of geometries they can describe. In order to design an arbitrarily shaped device using TO, a fully numerical method is necessary to perform the coordinate transformation and to calculate the resulting material properties for the device. This chapter presents a fully numerical technique based on the finite-difference method to generate and simulate arbitrary TO devices. The arbitrary spatial transforms are generated numerically by solving Laplace's equation [76, 77]. The devices are confirmed through simulation using an improved *anisotropic finite-difference frequency-domain* (AFDFD) method [17] that more efficiently simulates waves in arbitrary anisotropic media. Several examples are given to demonstrate the simplicity and versatility of our approach. This is the first known description of a complete numerical toolchain for TO that is based on the finite-difference method.

Historically, methods such as quasi-conformal mapping [78] and the solution of various partial differential equations such as Laplace's equation [76, 77], Poisson's equation [79], and the Helmholtz equation [80] have been used to generate the TO material parameters numerically. The approach presented in Ref. [78] can create arbitrary dielectric waveguides using TO, but does not allow for devices such as cloaks and lenses to be designed. The techniques described in Refs. [76, 77, 79, 80] use a commercial finite element software such as COMSOL to simulate a wide assortment of devices using TO, but it is difficult or impossible to use the calculated materials in a different electromagnetic solver. In contrast, the approach discussed in this article is designed specifically to be used with custom electromagnetic methods such as the AFDFD method described in Ref. [17] and will be incorporated into a toolchain which will generate devices using the geometry generation technique discussed in Ref. [81] to synthesize spatially variant lattices of metamaterial unit cells.

5.2 NUMERICAL GRID GENERATION USING LAPLACE'S EQUATION

The following subsections detail how to generate grids for spatial transforms numerically by solving Laplace's equation using finite-differences. The discussion begins by describing the generic solution to Laplace's equation using finite-differences. Techniques are presented to enforce the boundary conditions and to isolate the solution to specific portions of a grid. The discussion ends by showing how to use this tool to generate the grids associated with the spatial transforms used in TO, but for arbitrarily shaped objects.

5.2.1 Finite-Difference Approximation of Laplace's Equation

Laplace's equation for the generic function $U(x, y, z)$ is given by

$$\nabla^2 U(x, y, z) = 0. \quad (5.1)$$

It can be expanded into Cartesian coordinates according to

$$\left(\frac{\partial^2}{\partial x^2} + \frac{\partial^2}{\partial y^2} + \frac{\partial^2}{\partial z^2} \right) U(x, y, z) = 0 \quad (5.2)$$

By setting the second-order derivatives to zero, Laplace's equation essentially dictates that the function $U(x, y, z)$ must vary linearly as a function of position. To numerically solve Eq. (5.2) using the finite-difference method, the function $U(x, y, z)$ is stored at discrete points on a grid as illustrated in Figure 5.1. This figure shows a small 3D grid and an analogous 2D grid which stores the discretized function $U_{i,j,k}$.

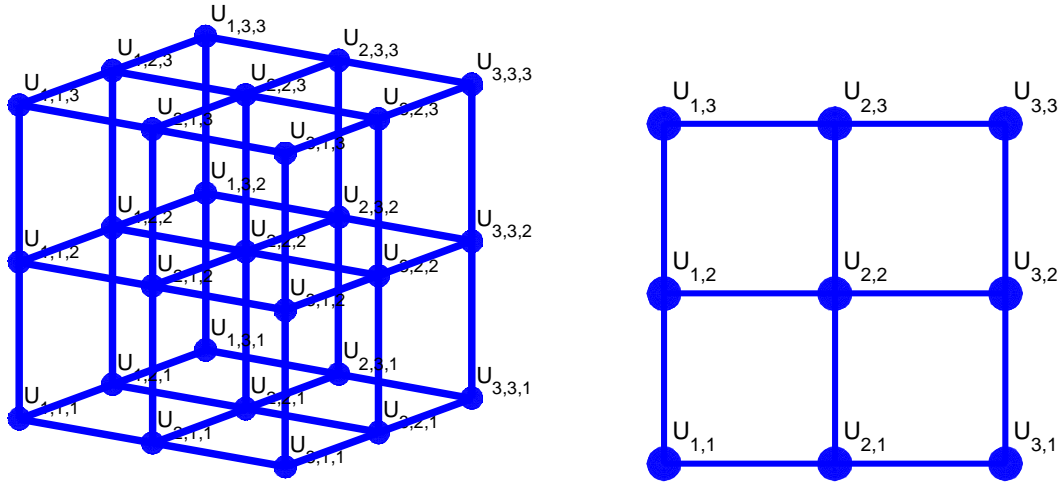


Figure 5.1: (Left) Three-dimensional grid for $U(x, y, z)$. (Right) Two-dimensional grid for $U(x, y, z)$.

This allows the second-order derivatives in Eq. (5.2) to be approximated with central finite-differences as follows.

$$\frac{U_{i+1,j,k} - 2U_{i,j,k} + U_{i-1,j,k}}{\Delta x^2} + \frac{U_{i,j+1,k} - 2U_{i,j,k} + U_{i,j-1,k}}{\Delta y^2} + \frac{U_{i,j,k+1} - 2U_{i,j,k} + U_{i,j,k-1}}{\Delta z^2} \approx 0. \quad (5.3)$$

Equation (5.3) can be interpreted as enforcing Laplace's equation on the discrete function $U_{i,j,k}$ at point (i,j,k) . To enforce Laplace's equations across the entire grid, Eq. (5.3) is written once for every point on the grid. This large set of equations can be written in matrix form as

$$\mathbf{L}\mathbf{u} = \mathbf{0}. \quad (5.4)$$

In Eq. (5.4), the term \mathbf{u} contains all of the unknown values of $U_{i,j,k}$ throughout the entire grid reshaped into a one-dimensional column vector. The square matrix \mathbf{L} operates on \mathbf{u} to calculate its scalar Laplacian ∇^2 . It is a banded matrix where the rows of \mathbf{L} are populated using Eq. (5.3), but an easier and more powerful approach for constructing \mathbf{L} and incorporating boundary conditions is described in the next subsection. The term $\mathbf{0}$ is a column vector the same size as \mathbf{u} but contains all zeros.

5.2.2 Matrix Operator Approach

Given a discrete function $U_{i,j,k}$ stored in a column vector \mathbf{u} , it is always possible to construct a square matrix \mathbf{L} that performs any linear operation on \mathbf{u} including derivatives [82, 83], discrete Fourier transforms [84, 85], convolutions [85], and more. Linearity makes it possible to breakdown complex linear operations into combinations of simpler linear operations. From Eq. (5.2), it is possible to express the Laplacian operation \mathbf{L} as the sum of three derivative operations \mathbf{D}_x^2 , \mathbf{D}_y^2 , and \mathbf{D}_z^2 to get Eq. (5.5).

$$\mathbf{L} = \mathbf{D}_x^2 + \mathbf{D}_y^2 + \mathbf{D}_z^2 \quad (5.5)$$

The terms \mathbf{D}_x^2 , \mathbf{D}_y^2 , and \mathbf{D}_z^2 are square banded matrices the same size as \mathbf{L} that calculate second-order derivatives of the function \mathbf{u} across the entire grid. These are simpler to construct than \mathbf{L} and easier to verify if they are correct, so it is often advantageous to construct these first and then calculate \mathbf{L} from them using Eq. (5.5).

As an example, the matrix Laplacian \mathbf{L} will be constructed for the two-dimensional 3×3 point grid shown in Figure 5.1. First, suppose we wish to calculate the second-order derivative of $U_{i,j,k}$ in the x direction. The finite-difference approximation for this can be written as

$$\frac{\partial^2 U_{i,j}}{\partial x^2} \approx \frac{U_{i+1,j} - 2U_{i,j} + U_{i-1,j}}{\Delta x^2}. \quad (5.6)$$

This equation is written once for every point on the grid and the large set of equations is collected into a single matrix equation. The matrix equation is expressed as a square matrix operating on the column vector \mathbf{u} . The square matrix derived from this process is the matrix derivative operator \mathbf{D}_x^2 as expressed in Eq. (5.7).

$$\mathbf{D}_x^2 \mathbf{u} = \frac{1}{\Delta x^2} \begin{bmatrix} U_{2,1} - 2U_{1,1} \\ U_{3,1} - 2U_{2,1} + U_{1,1} \\ -2U_{3,1} + U_{2,1} \\ U_{2,2} - 2U_{1,2} \\ U_{3,2} - 2U_{2,2} + U_{1,2} \\ -2U_{3,2} + U_{2,2} \\ U_{2,3} - 2U_{1,3} \\ U_{3,3} - 2U_{2,3} + U_{1,3} \\ -2U_{3,3} + U_{2,3} \end{bmatrix} = \frac{1}{\Delta x^2} \begin{bmatrix} -2 & 1 & & & & & & & \\ & 1 & -2 & 1 & & & & & \\ & & 1 & -2 & 0 & & & & \\ & & & 0 & -2 & 1 & & & \\ & & & & 1 & -2 & 1 & & \\ & & & & & 1 & -2 & 0 & \\ & & & & & & 0 & -2 & 1 \\ & & & & & & & 1 & -2 & 1 \\ & & & & & & & & 1 & -2 \end{bmatrix} \begin{bmatrix} U_{1,1} \\ U_{2,1} \\ U_{3,1} \\ U_{1,2} \\ U_{2,2} \\ U_{3,2} \\ U_{1,3} \\ U_{2,3} \\ U_{3,3} \end{bmatrix}. \quad (5.7)$$

A problem arises when writing Eq. (5.6) at both the left and right sides of the grid where values of $U_{i,j,k}$ are needed from outside of the grid. The manner in which this is handled is called a numerical boundary condition [62, 86]. To arrive at Eq. (5.7), it was assumed that all values of $U_{i,j,k}$ were zero outside of the grid. This is called the Dirichlet boundary condition [36, 87]. Second, the finite-difference approximation for the second-order derivative of $U_{i,j,k}$ in the y direction can be written as

$$\frac{\partial^2 U_{i,j}}{\partial y^2} \approx \frac{U_{i,j+1} - 2U_{i,j} + U_{i,j-1}}{\Delta y^2}. \quad (5.8)$$

This equation is also written once for every point on the grid and the large set of equations is collected into a single matrix equation expressed as a square matrix operating on the column vector \mathbf{u} . The square matrix derived from this process is the matrix derivative operator \mathbf{D}_y^2 as expressed in Eq. (5.9).

$$\mathbf{D}_y^2 \mathbf{u} = \frac{1}{\Delta y^2} \begin{bmatrix} U_{1,2} - 2U_{1,1} \\ U_{2,2} - 2U_{2,1} \\ U_{3,2} - 2U_{3,1} \\ U_{1,3} - 2U_{1,2} + U_{1,1} \\ U_{2,3} - 2U_{2,2} + U_{2,1} \\ U_{3,3} - 2U_{3,2} + U_{3,1} \\ -2U_{1,3} + U_{1,2} \\ -2U_{2,3} + U_{2,2} \\ -2U_{3,3} + U_{3,2} \end{bmatrix} = \frac{1}{\Delta y^2} \begin{bmatrix} -2 & & & 1 & & & & & \\ & -2 & & & 1 & & & & \\ & & -2 & & & 1 & & & \\ 1 & & & -2 & & & 1 & & \\ & 1 & & & -2 & & & 1 & \\ & & 1 & & & -2 & & & 1 \\ & & & 1 & & & -2 & & \\ & & & & 1 & & & -2 & \\ & & & & & 1 & & & -2 \end{bmatrix} \begin{bmatrix} U_{1,1} \\ U_{2,1} \\ U_{3,1} \\ U_{1,2} \\ U_{2,2} \\ U_{3,2} \\ U_{1,3} \\ U_{2,3} \\ U_{3,3} \end{bmatrix}. \quad (5.9)$$

Dirichlet boundary conditions were used again here at the top and bottom boundaries of the grid. Third, the Laplacian matrix \mathbf{L} for two dimensions is calculated by summing the above two derivative matrices.

$$\mathbf{L} = \mathbf{D}_x^2 + \mathbf{D}_y^2 \quad (5.10)$$

5.2.3 Enforcing Physical Boundary Conditions

At this point, our matrix equation has the form $\mathbf{L}\mathbf{u} = \mathbf{0}$. If this was solved for \mathbf{u} only a trivial solution would be obtained. The matrix equation can be written in a solvable form $\mathbf{L}\mathbf{u} = \mathbf{b}$ when the physical boundary conditions are incorporated. To do this, at least some values of $U_{i,j,k}$ on the grid must be known. Each known point is incorporated into the matrix equation by: (1) replacing the entire row in the matrix equation corresponding to that point with all 0's, (2) placing a 1 in the diagonal position in \mathbf{L} , and (3) placing the known value of $U_{i,j,k}$ into that same row of \mathbf{b} .

All of this can be accomplished in a more straightforward manner as follows. First, a force matrix \mathbf{F} is constructed. This is a diagonal matrix with 1's placed in the positions along diagonal that correspond to points with known values of $U_{i,j,k}$. Second, a force function $U_{F,i,j,k}$ is constructed that contains all of the known values placed at the correct points on the grid. The force function is reshaped into a one-dimensional column vector \mathbf{u}_F called the force vector. It may seem tedious or more complicated to construct these functions and matrices, but they need to be constructed anyway to describe arbitrary devices. Given the force matrix \mathbf{F} and the force vector \mathbf{u}_F , the matrix equation incorporating these physical boundary conditions is

$$\mathbf{L}'\mathbf{u} = \mathbf{b} \quad (5.11)$$

where

$$\mathbf{L}' = \mathbf{F} + (\mathbf{I} - \mathbf{F})\mathbf{L} \quad (5.12)$$

$$\mathbf{b} = \mathbf{F}\mathbf{u}_F. \quad (5.13)$$

The term \mathbf{I} is the identity matrix. A solution to Eq. (5.11) is calculated as $\mathbf{u} = \mathbf{L}^{-1}\mathbf{b}$. An example for a 13×13 point grid is provided in Figure 5.2. At left is the empty grid highlighting the known points, or physical boundary conditions. At right is the function $U_{i,j,k}$ after solving Laplace's equations with these boundary conditions. From this, we see that Laplace's equation provides a way to fill in all the other values of a function so that they vary linearly between the physical boundary conditions.

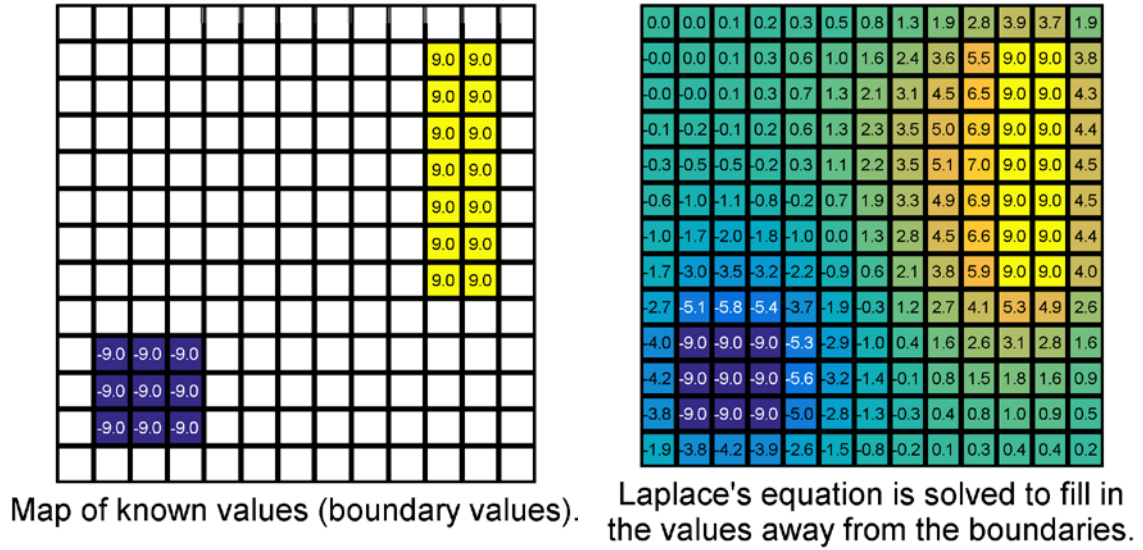


Figure 5.2. Two-dimensional grid to illustrate solution of Laplace's equation.

5.2.4 Enclosed Problems

It sometimes occurs that the physical boundary conditions completely enclose a portion of the grid and the solution to Laplace's equation is only needed within this enclosed region. It is most numerically efficient to only solve Laplace's equation within the enclosed region and not outside. This situation arises when designing devices by TO since the transform is typically contained within the volume of the device. A simple case of this concept is illustrated in Figure 5.3 where an arbitrary region of the grid is enclosed by the physical boundary conditions. The solution to Laplace's equation fills in the values inside the enclosed region, but no solution is obtained outside of the enclosed region.

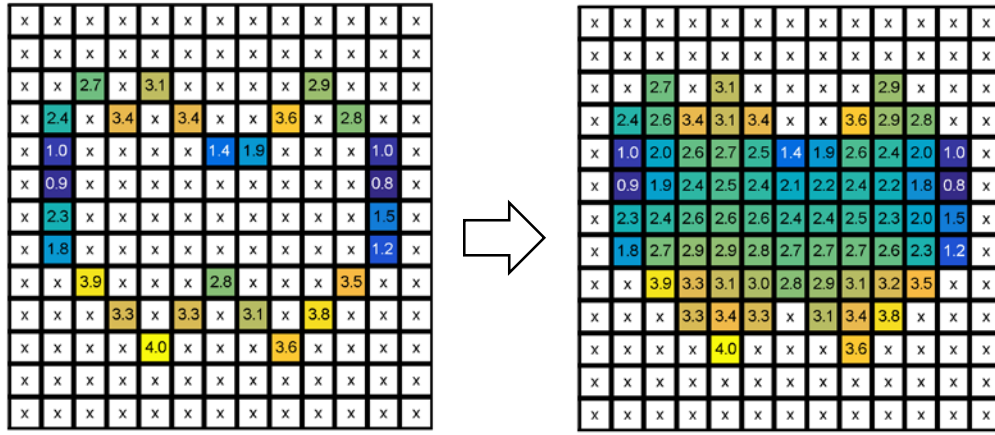


Figure 5.3. (Left) Physical boundary conditions enclose a portion of the grid. (Right) Solution to Laplace's equations obtained only in the enclosed portion of the grid.

The procedure to reduce Laplace's equation is simple. All of the points on the grid are identified where a solution to Laplace's equation is needed. The rows and columns corresponding to all other points are dropped from the matrix equation. The reduced matrix equation can be written as

$$\mathbf{L}''\mathbf{u}'' = \mathbf{b}''. \quad (5.14)$$

The concept of reducing the matrix equation is illustrated in Figure 5.4. To the remaining equations, the eliminated points have values of zero. However, this has no numerical effect because the unknown values are completely enclosed by the known points (i.e. physical boundary conditions) and not the eliminated points. After obtaining a solution to $\mathbf{u}'' = \mathbf{L}''^{-1}\mathbf{b}''$, the values from \mathbf{u}'' must be inserted into the correct positions in the full-size column vector \mathbf{u} . Values outside of the enclosed region can be set to anything because they are not of interest. Values of zero are a convenient choice.

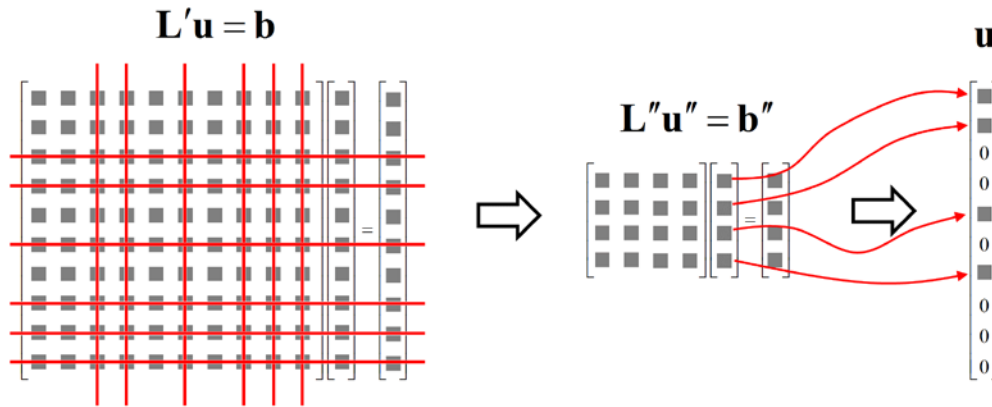


Figure 5.4. (Left) Matrix equation $\mathbf{L}'\mathbf{u} = \mathbf{b}$ for entire grid. (Middle) Reduced Laplace's equation.

5.2.5 Numerical Grid Generation

Numerical grid generation is used in fields such as oceanography [88], computational fluid dynamics [89-91], and conformal mapping in electromagnetics [78]. The approach allows complex geometries to be handled by mapping an arbitrary grid to a Cartesian grid. The most common approach is based on solving Laplace's equation [90, 92] for the transformed coordinates because it generates coordinates that vary linearly. Given the boundary conditions for an arbitrary coordinate transformation from $\{x, y, z\}$ to $\{x', y', z'\}$, Laplace's equation can be used to solve for the transformed coordinates using the following equations.

$$\nabla^2 x' = \left(\frac{\partial^2}{\partial^2 x} + \frac{\partial^2}{\partial^2 y} + \frac{\partial^2}{\partial^2 z} \right) x' = 0 \quad (5.15)$$

$$\nabla^2 y' = \left(\frac{\partial^2}{\partial^2 x} + \frac{\partial^2}{\partial^2 y} + \frac{\partial^2}{\partial^2 z} \right) y' = 0 \quad (5.16)$$

$$\nabla^2 z' = \left(\frac{\partial^2}{\partial^2 x} + \frac{\partial^2}{\partial^2 y} + \frac{\partial^2}{\partial^2 z} \right) z' = 0 \quad (5.17)$$

Occasionally, the backward coordinate transformation is advantageous. Examples of such cases will be discussed later. In the case where the backward coordinate transformation is favored, Laplace's equation can be solved for the backward transformation according to

$$\nabla^2 x = \left(\frac{\partial^2}{\partial^2 x'} + \frac{\partial^2}{\partial^2 y'} + \frac{\partial^2}{\partial^2 z'} \right) x = 0 \quad (5.18)$$

$$\nabla^2 y = \left(\frac{\partial^2}{\partial^2 x'} + \frac{\partial^2}{\partial^2 y'} + \frac{\partial^2}{\partial^2 z'} \right) y = 0 \quad (5.19)$$

$$\nabla^2 z = \left(\frac{\partial^2}{\partial^2 x'} + \frac{\partial^2}{\partial^2 y'} + \frac{\partial^2}{\partial^2 z'} \right) z = 0. \quad (5.20)$$

The solutions of Eq. (5.15) - (5.20) yields only the trivial solution until the boundary conditions are enforced. Consider the two arbitrary boundaries shown in Figure 5.5. The boundary conditions along the outer boundary Γ'_1 and the inner boundary Γ'_2 are given by

$$U(x', y')|_{\Gamma'_1(x, y)} = U(x, y)|_{\Gamma_1(x, y)} \quad (5.21)$$

$$U(x', y')|_{\Gamma'_2(x, y)} = U(x, y)|_{\Gamma_2(x, y)} \quad (5.22)$$

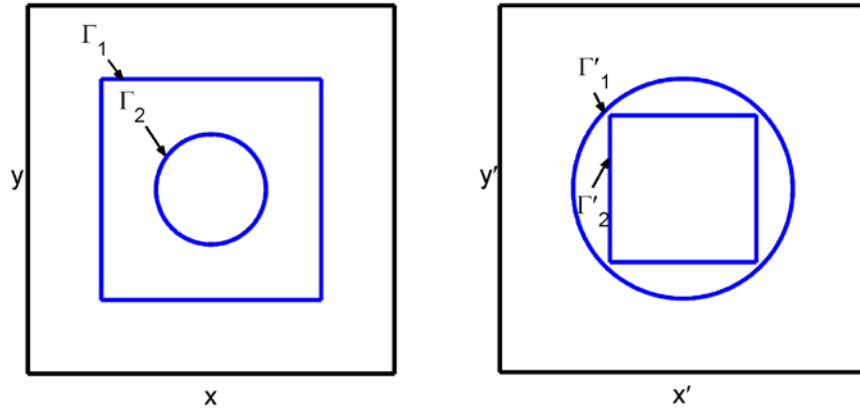


Figure 5.5. Boundary conditions for the coordinate transformation in equations (5.21) and (5.22). (Left) original coordinate system. (Right) Transformed coordinate system.

The force matrix and force vector are used to incorporate the boundary conditions into Eqs. (5.21) and (5.22). The force matrix \mathbf{F} contains 1's along the diagonal in the positions that correspond to the boundaries of the device which have known coordinate values. The force vector \mathbf{u}_F is a column vector containing the values of $U(x, y)$ at the boundaries. Given these two terms, the matrix equation can be put into a solvable form consistent with Eqs. (5.11)-(5.13). The matrix equation is further reduced to the form of Eq. (5.14) by dropping all rows and columns for points outside of the enclosed region being solved. This final equation can be solved using any standard algorithm such as an optimized LU decomposition algorithm for sparse linear systems [74] or an iterative solver such as the conjugate gradient method [75].

As the boundary problem shown in Figure 5.5 is only defined on the x - y plane, the z coordinate is not necessary and can be omitted from the Laplace's equations leaving just the following two equations to solve

$$\nabla^2 x' = \left(\frac{\partial^2}{\partial x^2} + \frac{\partial^2}{\partial y^2} \right) x' = 0 \quad (5.23)$$

$$\nabla^2 y' = \left(\frac{\partial^2}{\partial x^2} + \frac{\partial^2}{\partial y^2} \right) y' = 0. \quad (5.24)$$

Equations (5.23) and (5.24) are approximated with finite-differences and put into matrix form. The boundary conditions are applied using the force matrix \mathbf{F} and two force vector $\mathbf{u}_{x,F}$ and $\mathbf{u}_{y,F}$. The force

vectors $\mathbf{u}_{x,F}$ and $\mathbf{u}_{y,F}$ contain the x coordinates and y coordinates respectively defined by the boundary conditions. The boundary conditions are applied using the \mathbf{b}_x'' and \mathbf{b}_y'' vectors which have been reduced according to the method presented in the previous section. The matrix equation is then reduced by eliminating the rows and columns corresponding to points outside of the outer boundary. This gives two matrix equations to be solved within the region being transformed

$$\mathbf{L}''\mathbf{x}'' = \mathbf{b}_x'' \quad (5.25)$$

$$\mathbf{L}''\mathbf{y}'' = \mathbf{b}_y''. \quad (5.26)$$

These are solved according to

$$\mathbf{x}'' = \mathbf{A}''^{-1}\mathbf{b}_x'' \quad (5.27)$$

$$\mathbf{y}'' = \mathbf{A}''^{-1}\mathbf{b}_y''. \quad (5.28)$$

Figure 5.6 displays the result of solving the boundary value problem for the coordinate transformation from $\{x, y\} \rightarrow \{x', y'\}$.

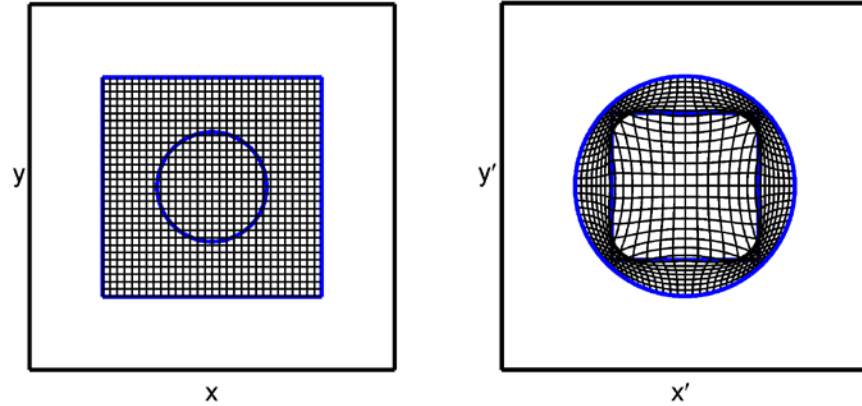


Figure 5.6. Coordinate transformation boundary value problem shown in Figure 5.5. The figure on the left is the original Cartesian coordinate system within the transformation boundaries. The figure on the right is the transformed coordinate system determined using the boundaries shown in Figure 5.5 and defined in Eqs. (5.21) and (5.22).

5.3 CALCULATING THE PERMITTIVITY AND PERMEABILITY FUNCTIONS

The permittivity function $[\varepsilon_r']$ and permeability function $[\mu_r']$ of the final device are calculated via TO from the background permittivity tensor $[\varepsilon_r]$, background permeability tensor $[\mu_r]$, and the spatial transforms discussed above. This reduces to calculating the following two equations at each point the grid [1]

$$[\varepsilon'_r] = \frac{\Lambda[\varepsilon_r]\Lambda^T}{\det \Lambda} \quad (5.29)$$

$$[\mu'_r] = \frac{\Lambda[\mu_r]\Lambda}{\det \Lambda} . \quad (5.30)$$

These equations come from a forward coordinate transform so they involve the Jacobian matrix Λ defined by

$$\Lambda = \begin{bmatrix} \Lambda_{xx} & \Lambda_{xy} & \Lambda_{xz} \\ \Lambda_{yx} & \Lambda_{yy} & \Lambda_{yz} \\ \Lambda_{zx} & \Lambda_{zy} & \Lambda_{zz} \end{bmatrix} = \begin{bmatrix} \frac{\partial x'}{\partial x} & \frac{\partial x'}{\partial y} & \frac{\partial x'}{\partial z} \\ \frac{\partial y'}{\partial x} & \frac{\partial y'}{\partial y} & \frac{\partial y'}{\partial z} \\ \frac{\partial z'}{\partial x} & \frac{\partial z'}{\partial y} & \frac{\partial z'}{\partial z} \end{bmatrix} . \quad (5.31)$$

The elements of the Jacobian matrix can be computed numerically using finite-differences [17, 71] and stored as arrays as follows.

$$\Lambda_{xx}(i, j, k) = \frac{\partial x'}{\partial x} \cong \frac{x'_{i+1,j,k} - x'_{i-1,j,k}}{2\Delta x} \quad (5.32)$$

$$\Lambda_{xy}(i, j, k) = \frac{\partial x'}{\partial y} \cong \frac{x'_{i,j+1,k} - x'_{i,j-1,k}}{2\Delta y} \quad (5.33)$$

$$\Lambda_{xz}(i, j, k) = \frac{\partial x'}{\partial z} \cong \frac{x'_{i,j,k+1} - x'_{i,j,k-1}}{2\Delta z} \quad (5.34)$$

$$\Lambda_{yx}(i, j, k) = \frac{\partial y'}{\partial x} \cong \frac{y'_{i+1,j,k} - y'_{i-1,j,k}}{2\Delta x} \quad (5.35)$$

$$\Lambda_{yy}(i, j, k) = \frac{\partial y'}{\partial y} \cong \frac{y'_{i,j+1,k} - y'_{i,j-1,k}}{2\Delta y} \quad (5.36)$$

$$\Lambda_{yz}(i, j, k) = \frac{\partial y'}{\partial z} \cong \frac{y'_{i,j,k+1} - y'_{i,j,k-1}}{2\Delta z} \quad (5.37)$$

$$\Lambda_{zx}(i, j, k) = \frac{\partial z'}{\partial x} \cong \frac{z'_{i+1,j,k} - z'_{i-1,j,k}}{2\Delta x} \quad (5.38)$$

$$\Lambda_{zy}(i, j, k) = \frac{\partial z'}{\partial y} \cong \frac{z'_{i,j+1,k} - z'_{i,j-1,k}}{2\Delta y} \quad (5.39)$$

$$\Lambda_{zz}(i, j, k) = \frac{\partial z'}{\partial z} \cong \frac{z'_{i,j,k+1} - z'_{i,j,k-1}}{2\Delta z} \quad (5.40)$$

For two-dimensional devices like this that are uniform in the z -direction, it is only necessary to calculate four elements of the Jacobian, Λ_{xx} , Λ_{xy} , Λ_{yx} , and Λ_{yy} . The elements Λ_{xz} , Λ_{yz} , Λ_{zx} , and Λ_{zy} are arrays of all zeros and Λ_{zz} is an array of all ones.

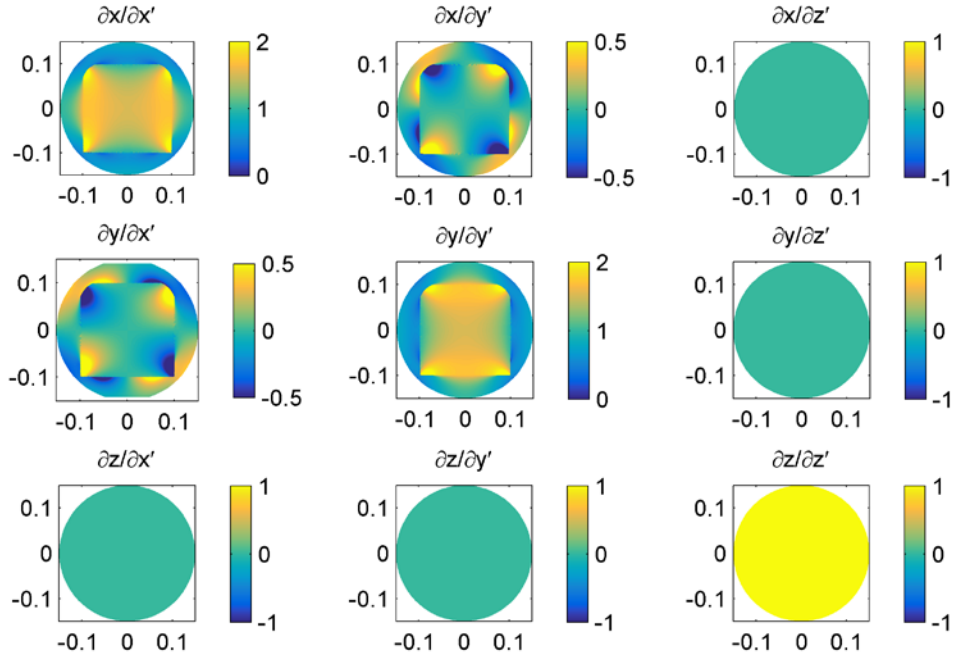


Figure 5.7. Elements composing the Jacobian matrix for the coordinate transformation shown in Figure 5.6.

Iterating through the grid point-by-point, the Jacobian matrix at each grid position is assembled according to Eq. (5.31) with the derivatives evaluated at each point. Depending on how the coordinate transformations were determined, it is sometimes necessary to calculate the Jacobian for the backward coordinate transformation according to

$$\Lambda' = \begin{bmatrix} \Lambda'_{xx} & \Lambda'_{xy} & \Lambda'_{xz} \\ \Lambda'_{yx} & \Lambda'_{yy} & \Lambda'_{yz} \\ \Lambda'_{zx} & \Lambda'_{zy} & \Lambda'_{zz} \end{bmatrix} = \begin{bmatrix} \frac{\partial x}{\partial x'} & \frac{\partial x}{\partial y'} & \frac{\partial x}{\partial z'} \\ \frac{\partial y}{\partial x'} & \frac{\partial y}{\partial y'} & \frac{\partial y}{\partial z'} \\ \frac{\partial z}{\partial x'} & \frac{\partial z}{\partial y'} & \frac{\partial z}{\partial z'} \end{bmatrix}. \quad (5.41)$$

The calculated derivatives are each stored in an array the same size as the grid as shown in Figure 5.7.

The forward Jacobian matrix can be found from the backward Jacobian matrix by calculating the inverse [46, 93, 94]. The permittivity tensor is calculated at the point i,j,k within the grid using Eq. (5.29) with the Jacobian matrix appropriate to the coordinate transformation. The permittivity tensor can be written where each element is stored as an array.

$$\left[\varepsilon'_r(i, j, k) \right] = \begin{bmatrix} \varepsilon'_{xx}(i, j, k) & \varepsilon'_{xy}(i, j, k) & \varepsilon'_{xz}(i, j, k) \\ \varepsilon'_{yx}(i, j, k) & \varepsilon'_{yy}(i, j, k) & \varepsilon'_{yz}(i, j, k) \\ \varepsilon'_{zx}(i, j, k) & \varepsilon'_{zy}(i, j, k) & \varepsilon'_{zz}(i, j, k) \end{bmatrix}. \quad (5.42)$$

Likewise, the permeability tensor can be written as

$$\left[\mu'_r(i, j, k) \right] = \begin{bmatrix} \mu'_{xx}(i, j, k) & \mu'_{xy}(i, j, k) & \mu'_{xz}(i, j, k) \\ \mu'_{yx}(i, j, k) & \mu'_{yy}(i, j, k) & \mu'_{yz}(i, j, k) \\ \mu'_{zx}(i, j, k) & \mu'_{zy}(i, j, k) & \mu'_{zz}(i, j, k) \end{bmatrix}. \quad (5.43)$$

5.4 BENCHMARK AND EXAMPLES

5.4.1 Cylindrical Electromagnetic Cloak

To benchmark our approach, we duplicated the famous cylindrical electromagnetic cloak presented in Ref. [18]. This was based on the closed form coordinate transformation given by

$$\begin{aligned} r' &= R_1 + r \frac{R_2 - R_1}{R_2} \\ \theta' &= \theta \\ z' &= z \end{aligned}, \quad (5.44)$$

where the cloak has an inner radius R_1 and outer radius R_2 . Figure 5.8 shows the outlines of the boundaries of the coordinate transformation given by Eq. (5.44).

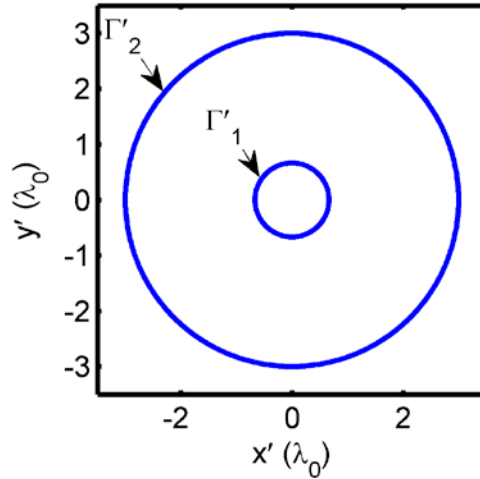


Figure 5.8. Coordinate transformation boundary conditions for a cylindrical cloak.

In order to calculate the coordinate transformation numerically, the following boundary conditions were applied

$$\Gamma'_2(x', y') = \Gamma_2(x, y) \quad (5.45)$$

$$\Gamma'_1(x', y') = 0. \quad (5.46)$$

Given Eq. (5.46), the transformation from $\{x, y, z\} \rightarrow \{x', y', z'\}$ experienced a strong singularity in the cloaked region. This was overcome by calculating the backward rather than the forward coordinate transformation. The material tensors were calculated by following the approach described previously. The resulting permittivity tensor is shown in Figure 5.9. For a cylindrical cloak in free space, the permeability tensor is identical to the permittivity tensor. All tensor components which are not visualized are equal to one for the elements along the diagonal and zeros for the off-diagonal elements. The values determined for this cloak are based on a grid resolution of $\lambda_0 / 120$. As the grid resolution is made smaller, the values of the materials required would approach infinity or zero due to the cloaked region being a singularity.

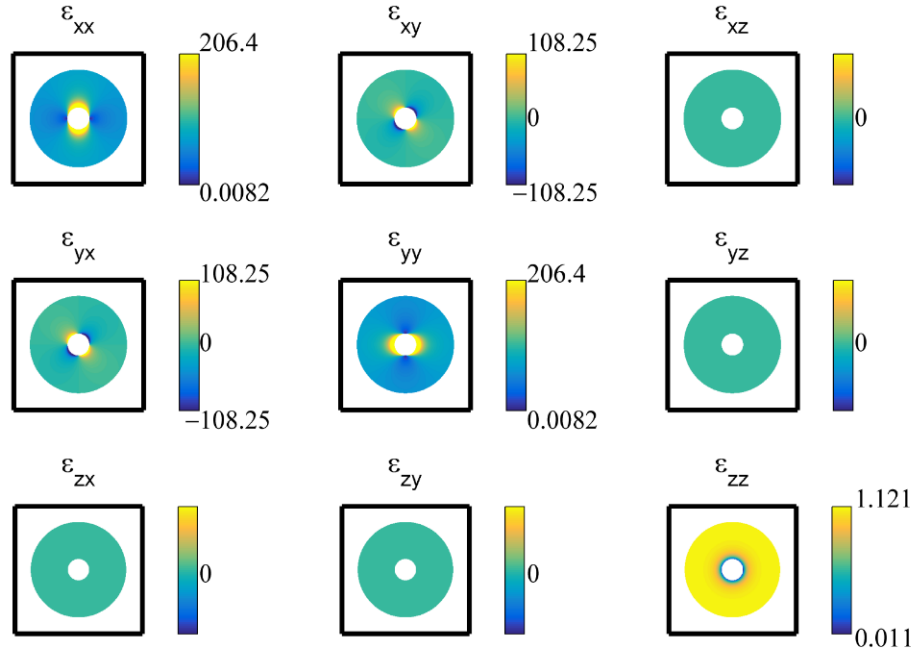


Figure 5.9. Permittivity tensor for cylindrical electromagnetic cloak.

The device was simulated using the improved AFDFD. Dirichlet boundary conditions were used for the y -axis boundaries while a UPML was used for the x -axis boundaries. The result is shown in Figure 5.10.

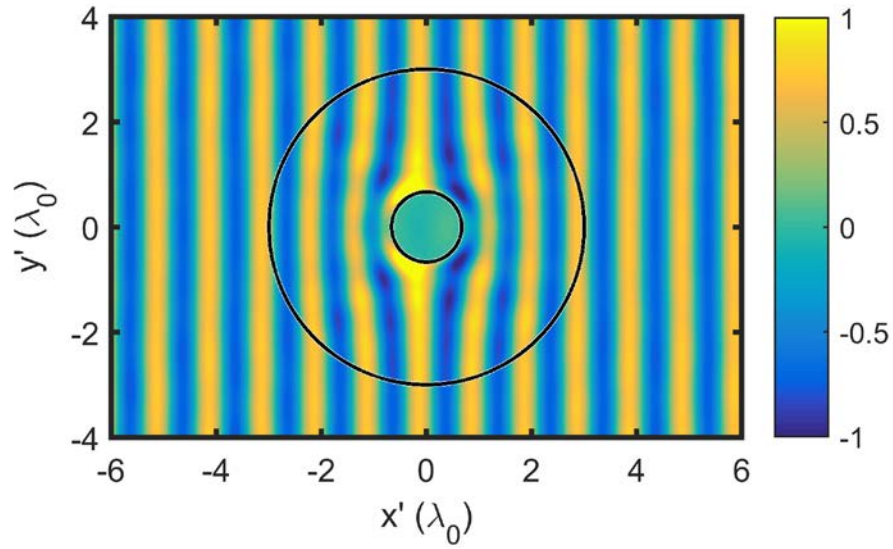


Figure 5.10. AFDFD simulation of cylindrical electromagnetic cloak.

5.4.2 Flat Lens

Figure 5.11 shows the boundary conditions necessary to design a flat lens using TO as described in Ref. [2]. By solving Laplace's equation for the boundaries

$$\begin{aligned}
 \Gamma_1 &\rightarrow \Gamma'_1 \\
 \Gamma_2 &\rightarrow \Gamma'_2 \\
 \Gamma_3 &\rightarrow \Gamma'_3 \\
 \Gamma_4 &\rightarrow \Gamma'_4
 \end{aligned}
 \tag{5.47}$$

the coordinate transformation was computed numerically.

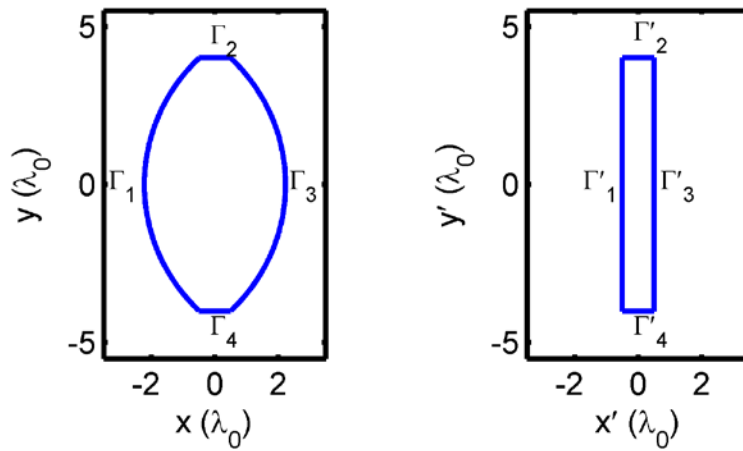


Figure 5.11. Coordinate transformation for flat transformation optics lens. The figure on the left is the original coordinate space while that on the right is the transformed space.

With the coordinates in the new system known, the Jacobian matrix was calculated using Eq. (5.31) and the material tensors determined using Eqs. (5.29) and (5.30). The resulting permittivity is shown in Figure 5.12. The permeability is identical to the permittivity in this situation because the original space is vacuum.

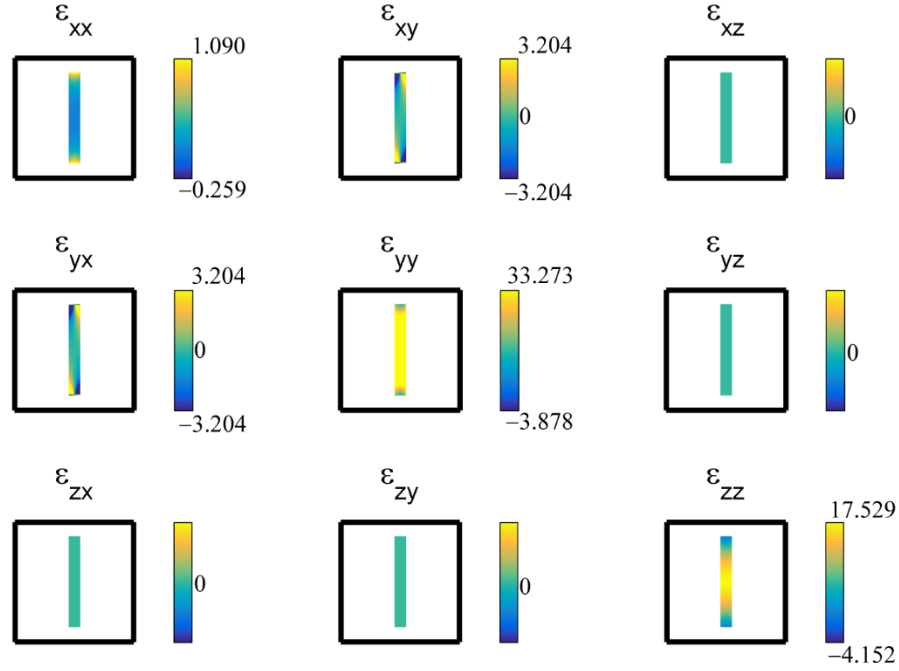


Figure 5.12. Permittivity tensors for flat transformation optics lens. The permeability tensor is identical for a bend based in free space. All tensor components which are not visualized are zero throughout the grid. The material values for this lens are for a grid resolution of $\lambda_0 / 120$

Using AFDFD, the material tensors were placed within a grid surrounded by a UPML and a cylindrical source was used. Aside from diffraction around the edges, the electric field in

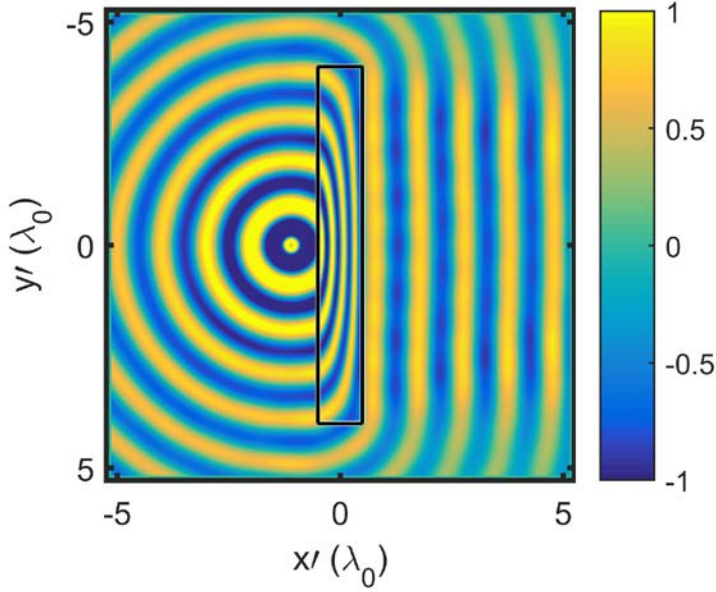


Figure 5.13 can be seen to be converted to a plane wave as would be expected from a conventional lens.

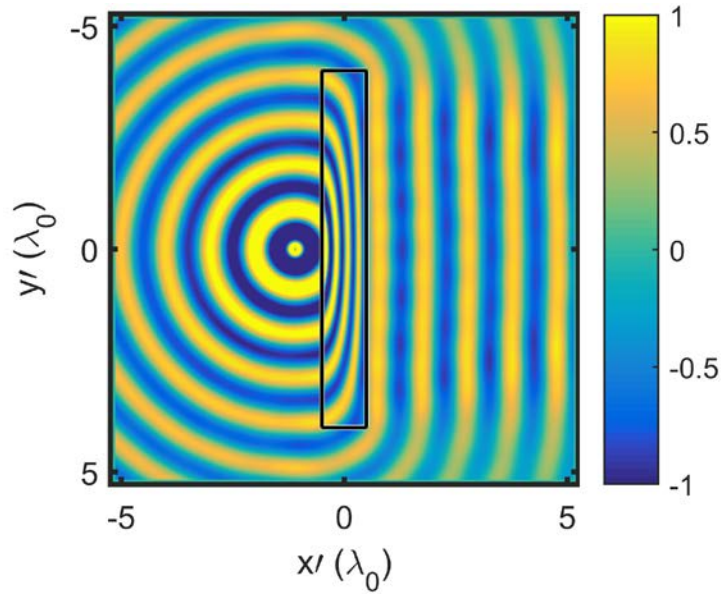


Figure 5.13. AFDFD simulation of flat TO lens.

5.4.3 Arbitrary Cloak

This section will demonstrate the method implemented above with the arbitrary metamaterial cloak shown in Figure 5.14. The pickaxe shape bounded by Γ'_1 is being cloaked by the region bounded by Γ'_2 .

In order to cloak the object, a coordinate system in which the axes wrap around the object without

penetrating the object itself must be implemented within the region between the two boundaries. In order to avoid singular Jacobian matrices in the cloaked region, the backward coordinate transformation was implemented rather than the forward transformation. The boundary conditions, which were derived from those described in Ref. [76], are given as follows.

$$\Gamma'_2(x', y') = \Gamma_2(x, y) \quad (5.48)$$

$$\Gamma'_1(x', y') = 0 \quad (5.49)$$

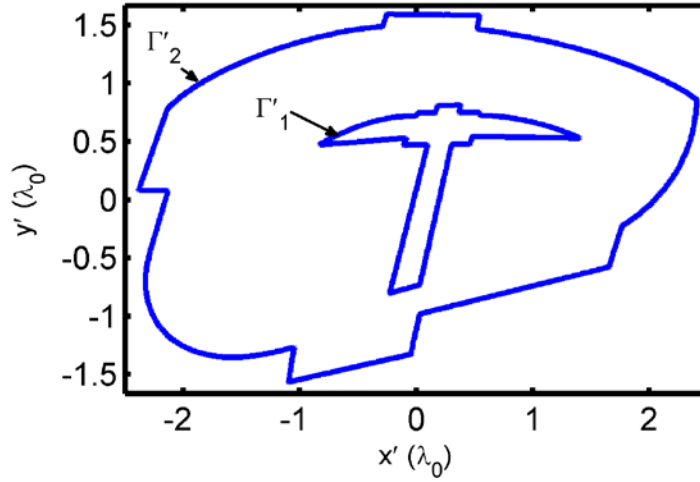


Figure 5.14. Outline of arbitrary electromagnetic cloak and object to be cloaked.

Following the procedure described in the previous sections of this chapter the material tensors were calculated. The resulting permittivity tensor is shown in Figure 5.15 with the permeability tensor being the same.

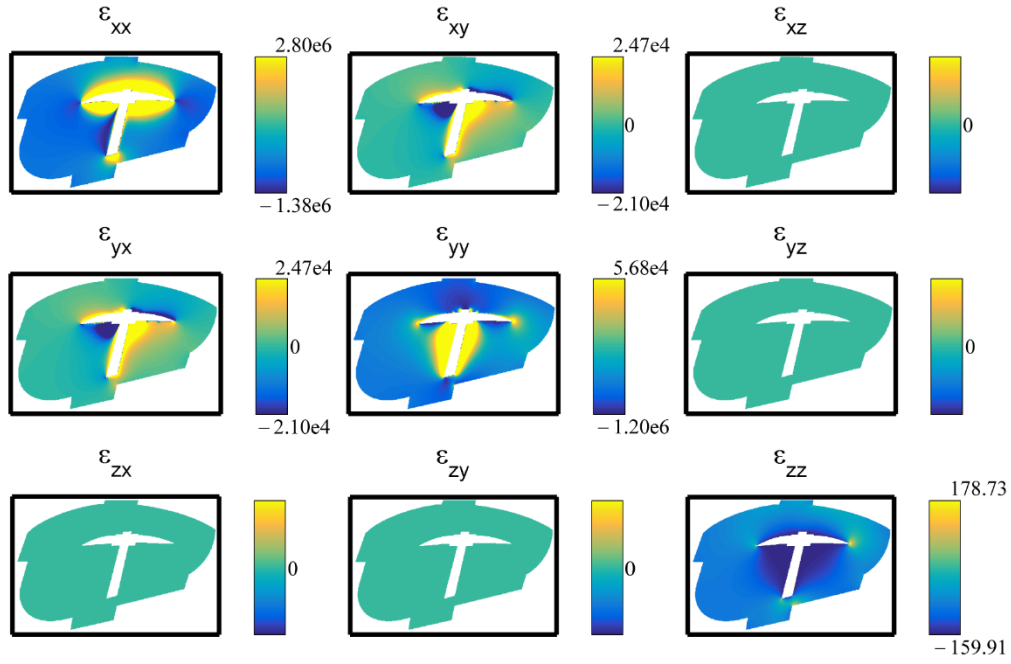


Figure 5.15. Permittivity tensor for arbitrary electromagnetic cloak. The permeability tensor is identical for a cloak based in free space. All tensor components which are not visualized are equal to one for the elements along the diagonal and zeros for the off-diagonal elements.

Using AFDFD, the TO cloak was simulated for a *transverse magnetic* (TM) polarized wave as shown in Figure 5.16. A TM polarized wave is one in which the magnetic field is polarized parallel to the plane of incidence which is the plane consisting of the incident, transmitted, and reflected wave vectors [95]. The plane of incidence is defined as the plane containing the incident, reflected, and transmitted wave vectors [96]. The material tensors for the cloak were placed between a UPML on the x -axis boundaries and Dirichlet boundary conditions, which were described in Chapter 4, on the y -axis boundaries. As can be seen, very little power is scattered and the phase of the wave is very well preserved.

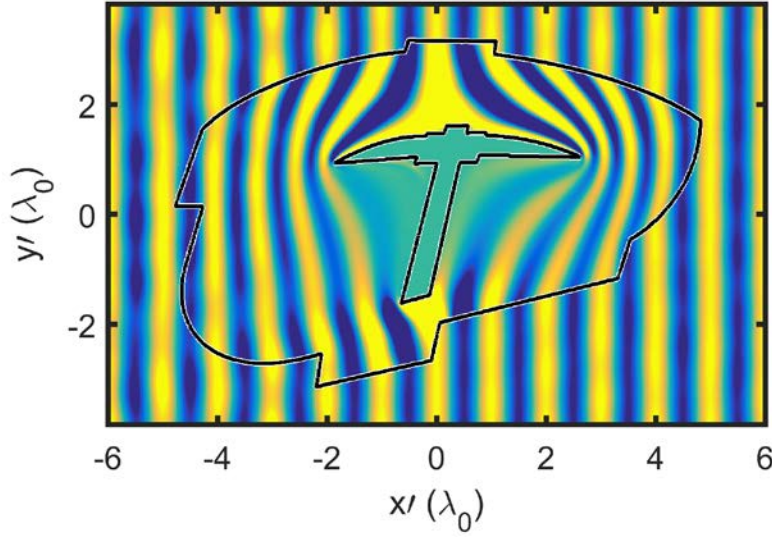


Figure 5.16. AFDFD simulation of arbitrary electromagnetic cloak.

5.4.4 Transformation Optics Bend

Creating a bend using numerical TO involves solving Laplace's equation for the boundary value problem shown in Figure 5.17. Rather than transform from $\{x, y\}$ to $\{x', y'\}$, the backward transformation was chosen because mapping the arbitrarily distorted boundaries shown on the right in Figure 5.17 to the boundaries of the original system could be done with simple analytical expressions. Solving Laplace's equation with the boundary values

$$\begin{aligned}
 \Gamma'_1 &\rightarrow \Gamma_1 \\
 \Gamma'_2 &\rightarrow \Gamma_2 \\
 \Gamma'_3 &\rightarrow \Gamma_3 \\
 \Gamma'_4 &\rightarrow \Gamma_4
 \end{aligned}
 \tag{5.50}$$

provides the coordinates of the backward coordinate transformation.

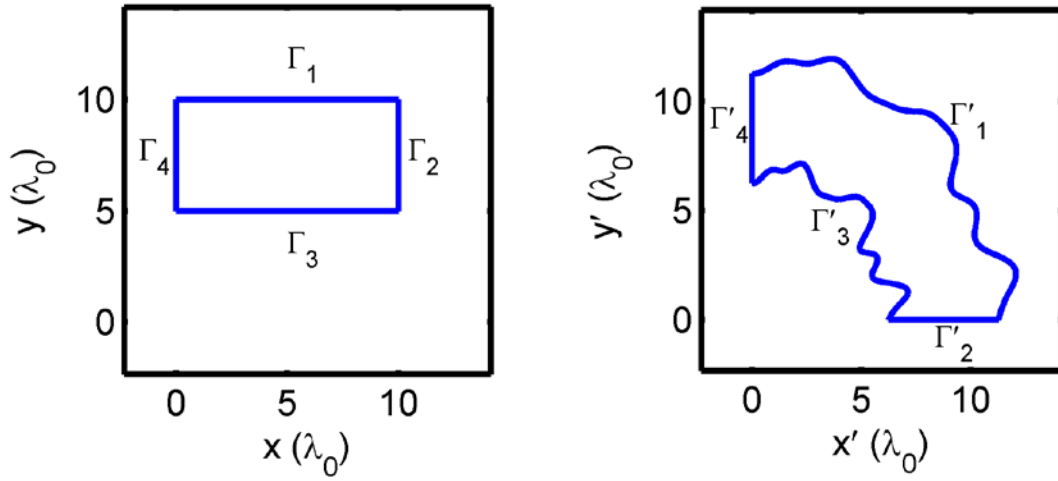


Figure 5.17. Coordinate transformation for transformation optics bend. The figure on the left is the original coordinate space while that on the right is the transformed space.

Using the procedure described above, the material tensors were calculated as shown in Figure 5.18 and placed in a grid surrounded by a UPML. This was simulated using AFDFD and the result is shown in Figure 5.19. The UPML regions are visible as areas where the wave is absorbed on all of the boundaries of the simulation domain.

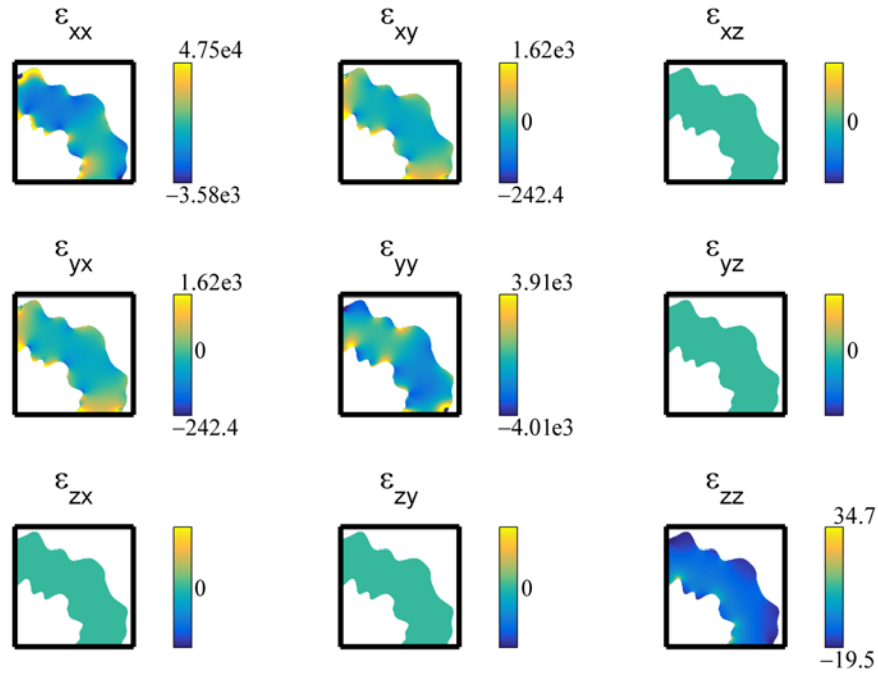


Figure 5.18. Permittivity tensors for arbitrary electromagnetic bend. The permeability tensor is identical for a bend based in free space. All tensor components which are not visualized are zero throughout the grid.

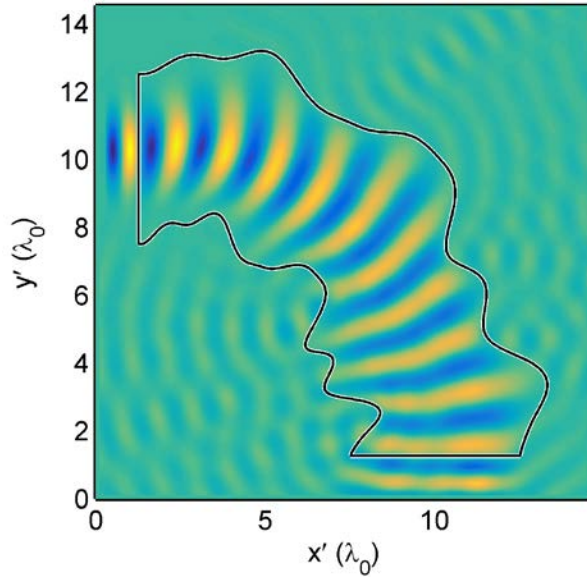


Figure 5.19. AFDFD simulation of TO electromagnetic bend.

5.5 CONCLUSIONS

A simple technique for generating and simulating TO devices with arbitrary geometry was described in this chapter. Laplace's equation was used to generate the coordinates of the spatial transforms. The method described uses a finite-difference approach so it is simple and straightforward to implement. Other approaches in the literature used commercial software such as COMSOL, making it difficult or impossible to import and export complex data. The technique described in this chapter can be implemented independent of a commercial solver and in virtually any programming environment. This allows much greater flexibility in manipulating the data and importing the generated materials into custom electromagnetic solvers such as finite-difference time-domain, finite-difference frequency-domain, beam propagation method, and more. Further, an improvement to the standard AFDFD method was outlined that greatly improves the speed and efficiency for simulating TO devices. The new approach utilized the impermeability tensor instead of the permeability tensor in the matrix wave equation.

Several examples were presented to benchmark the approach and demonstrate its versatility. The devices included the classical cylindrical cloak, an arbitrarily shaped cloak, a flat lens, and an arbitrarily shaped bend. Devices with arbitrary shapes were verified through simulation using the improved AFDFD. The simulation results showed excellent performance of the devices.

Chapter 6: Synthesis of Spatially Variant Lattices

6.1 PURPOSE

In order to create devices which affect the electromagnetic field in a meaningful way, it is necessary to introduce an inhomogeneous structure. It is also desired that any variations in the underlying structure do not perturb the field in a way which would introduce unwanted scattering or degradation of performance [81]. Consider the lattice shown in Figure 6.1a [97].

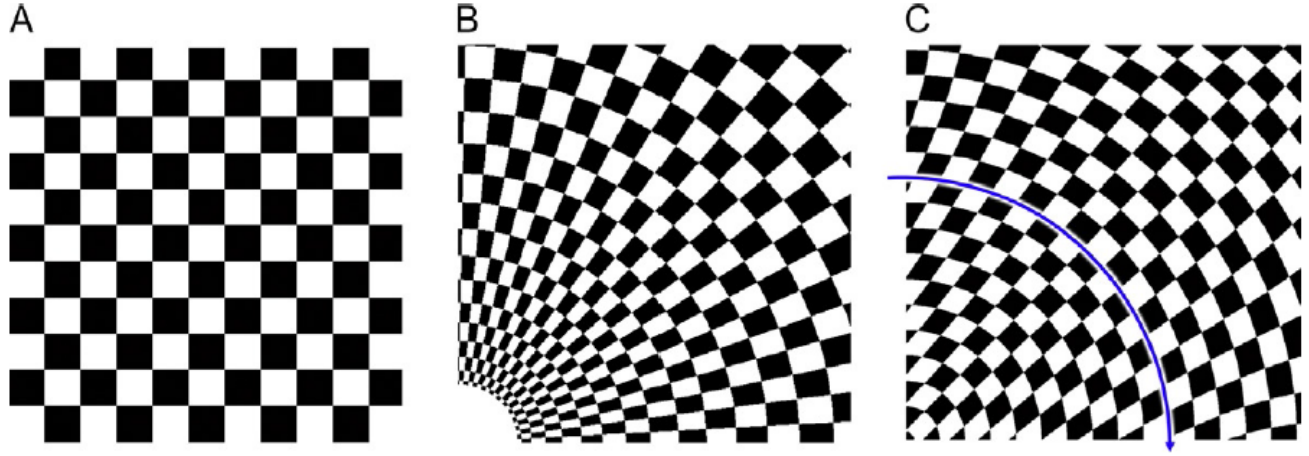


Figure 6.1: (a) Uniform lattice of periodic unit cells, (b) lattice bent 90° using conventional means, (c) lattice bent using spatially variant lattice synthesis tool [97].

If this lattice were to be bent 90° using traditional techniques the result would be as shown in Figure 6.1b. In order to preserve the size and shape of the unit cells as smooth and continuous as possible a method of spatially varying lattices has been developed [81, 97, 98]. This methodology has been used to design self-collimating photonic crystals [98-100], multi-mode waveguide bends in spatially variant band gap material [101], and to control the near-field of transmission lines embedded in a *spatially variant anisotropic metamaterial* (SVAM) [102]. The lattice of Figure 6.1a when spatially varied using the approach of Ref. [81] is shown in Figure 6.1c.

6.2 GRATING VECTORS

The dielectric function of a grating with grating vector

$$\vec{K} = K_x \hat{x} + K_y \hat{y} + K_z \hat{z} \quad (6.1)$$

having a magnitude

$$|K| = \frac{2\pi}{\Lambda} \quad (6.2)$$

is given by [97]

$$\varepsilon_r(\vec{r}) = \varepsilon_{\text{avg}} + \Delta\varepsilon \cos(\vec{K} \cdot \vec{r}) \quad (6.3)$$

where the ε_{avg} is the average permittivity, $\Delta\varepsilon$ is the dielectric contrast and \vec{r} is the position vector given by

$$\vec{r} = x\hat{x} + y\hat{y} + z\hat{z} \quad (6.4)$$

in which the terms \hat{x} , \hat{y} , and \hat{z} in Eqs. (6.1) and (6.4) are the unit vectors. For a grating vector which is a function of position Eq. (6.3) fails to create the proper grating [81, 97, 101]. An alternative to the dielectric function given in Eq. (6.3) is

$$\varepsilon_r(\vec{r}) = \varepsilon_{\text{avg}} + \Delta\varepsilon \cos(\Phi(\vec{r})) \quad (6.5)$$

where the term $\Phi(\vec{r})$ is the grating phase given by

$$\nabla\Phi(\vec{r}) = \vec{K}(\vec{r}). \quad (6.6)$$

In order to determine $\Phi(\vec{r})$ from Eq. (6.6) finite-difference are used as described in 4.3.

Writing Eq. (6.6) as

$$\begin{bmatrix} \partial/\partial x \\ \partial/\partial y \\ \partial/\partial z \end{bmatrix} \Phi(\vec{r}) = \begin{bmatrix} K_x(\vec{r}) \\ K_y(\vec{r}) \\ K_z(\vec{r}) \end{bmatrix} \quad (6.7)$$

a block matrix equation can be formed using the finite difference matrix operators described in Chapter 4 written as

$$\begin{bmatrix} \mathbf{D}_x \\ \mathbf{D}_y \\ \mathbf{D}_z \end{bmatrix} \Phi = \begin{bmatrix} \mathbf{k}_x \\ \mathbf{k}_y \\ \mathbf{k}_z \end{bmatrix}. \quad (6.8)$$

Equation (6.8) is an overdetermined system of equations since there are more equations than unknowns. As such, a best-fit method such as the method of least-squares must be used to approximate a solution [103]. Writing Eq. (6.8) in the form $\mathbf{Ax} = \mathbf{b}$ with

$$\mathbf{A} = \begin{bmatrix} \mathbf{D}_x \\ \mathbf{D}_y \\ \mathbf{D}_z \end{bmatrix} \quad (6.9)$$

$$\mathbf{x} = \Phi \quad (6.10)$$

and

$$\mathbf{b} = \begin{bmatrix} \mathbf{k}_x \\ \mathbf{k}_y \\ \mathbf{k}_z \end{bmatrix} \quad (6.11)$$

a modified system of equations utilizing least squares is given by

$$\mathbf{A}^T \mathbf{A} \mathbf{x} = \mathbf{A}^T \mathbf{b} \quad (6.12)$$

Rewriting the terms in (6.12) as

$$\mathbf{A}' = \mathbf{A}^T \mathbf{A} \quad (6.13)$$

$$\mathbf{b}' = \mathbf{A}^T \mathbf{b} \quad (6.14)$$

gives

$$\mathbf{A}' \mathbf{x} = \mathbf{b}' \quad (6.15)$$

which can be solved using

$$\mathbf{x} = (\mathbf{A}')^{-1} \mathbf{b}' \quad (6.16)$$

6.3 SPATIALLY VARYING PARAMETERS

In order to spatially vary a geometry, the grating vector is used to define the spatial variations throughout the computational grid. Expressing the grating vector in two dimensions using the form given in [97]

$$\vec{K}(\vec{r}) = \frac{2\pi}{\Lambda(\vec{r})} \{ \hat{a}_x \cos[\theta(\vec{r})] + \hat{a}_y \sin[\theta(\vec{r})] \} \quad (6.17)$$

In Eq. (6.17) several terms can be used to define the spatial variation throughout the lattice. The lattice period $\Lambda(\vec{r})$ adjusts the spacing between unit cells and the orientation in the $x - y$ plane is given by $\theta(\vec{r})$. Another term which can be used to control the spatial variation of the grid is the fill fraction.

The fill fraction is assigned according to [81] as

$$\varepsilon(\vec{r}) = \begin{cases} \varepsilon_1 & \varepsilon_r(\vec{r}) \leq \gamma(\vec{r}) \\ \varepsilon_2 & \varepsilon_r(\vec{r}) > \gamma(\vec{r}) \end{cases} \quad (6.18)$$

where

$$\gamma(\vec{r}) = \cos(\pi f) \quad (6.19)$$

with f being the fill fraction of the lattice. Figure 6.2 displays a summary of the spatial variation parameters and their effect on the grating phase and resulting dielectric function.

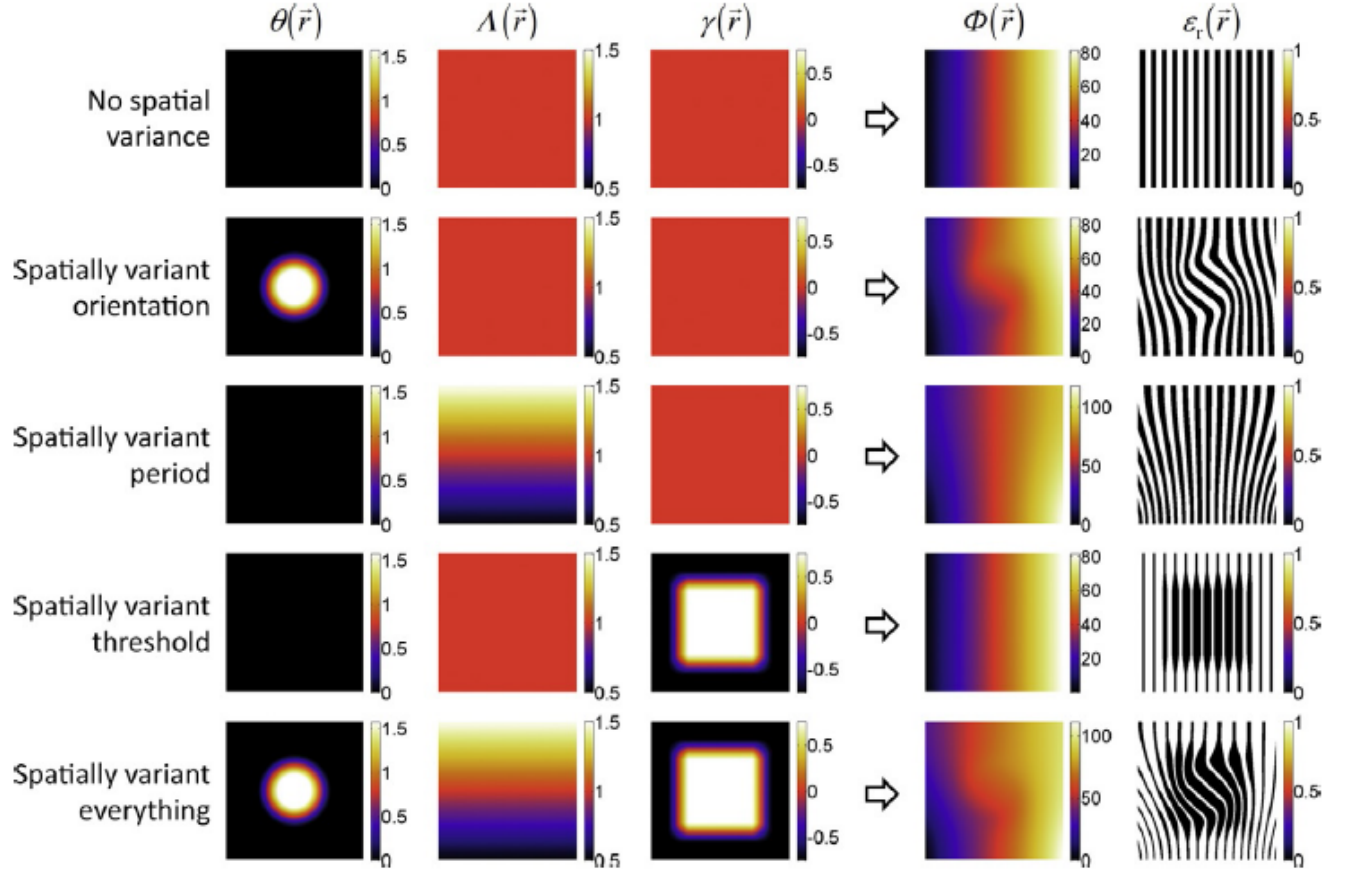


Figure 6.2: Summary of spatial variation parameters for a spatially variant grating [97].

6.4 SPATIAL HARMONICS

A unit cell with lattice periods Λ_x , Λ_y , and Λ_z comprising a lattice of periodic cells can be written using a Fourier series expansion as given by [81]

$$\varepsilon_{uc}(\vec{r}) = \sum_{m=1}^M a_m \exp(j\vec{K}_m \cdot \vec{r}) \quad (6.20)$$

where a_m is the complex amplitude of the m^{th} harmonic, \vec{r} is the position vector, and

$$\vec{K}_m = \frac{2\pi p}{\Lambda_x} \hat{x} + \frac{2\pi q}{\Lambda_y} \hat{y} + \frac{2\pi r}{\Lambda_z} \hat{z} \quad (6.21)$$

is the grating vector of the m^{th} harmonic.

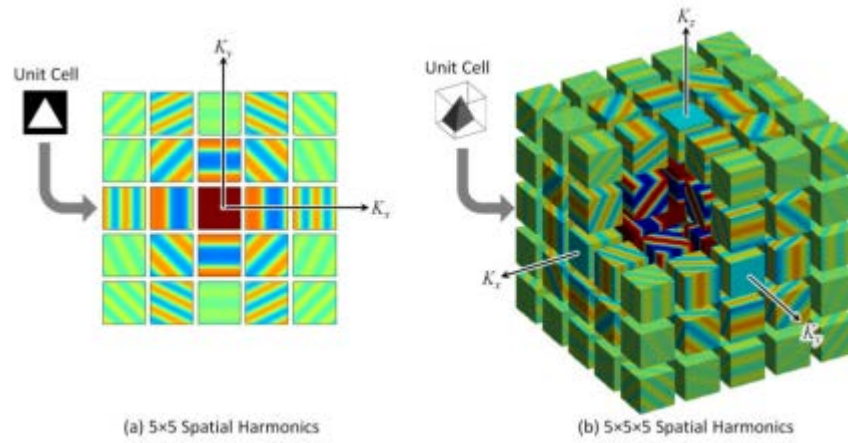


Figure 6.3: Spatial harmonics for 2D and 3D unit cell arranged in an infinitely periodic lattice [81].

The unit cell shown in Figure 6.3a is a two dimensional unit cell decomposed into 5×5 spatial harmonics. Likewise, the unit cell shown in Figure 6.3b is a three dimensional cell decomposed into $5 \times 5 \times 5$ spatial harmonics.

In order to adequately reconstruct the unit cell a sufficient number of spatial harmonics must be used. In particular, unit cells with very sharp features require more harmonics in order to resolve the features of the structure. Figure 6.4 shows the effect of increasing spatial harmonics on the resolution of a triangular unit cell. In addition to resolving the edges and vertices more clearly, the increased number of spatial harmonics also reduces the blur at the edges of the unit cell.

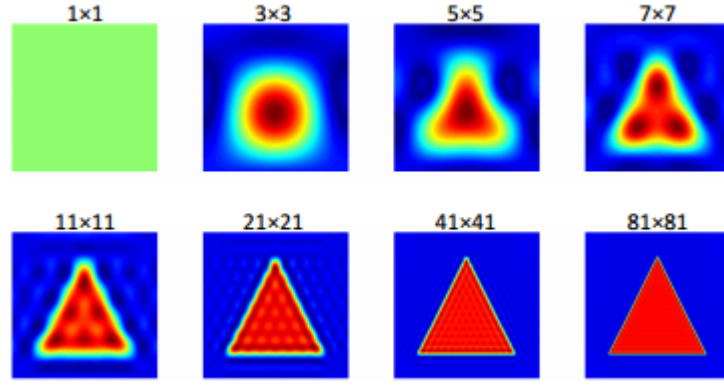


Figure 6.4: Effect of number of spatial harmonics in the reconstruction of a unit cell [104]

Another concept important for the reconstruction of fine featured unit cells is Gibb's phenomenon. Gibb's phenomenon is a concept from Fourier analysis which describes the reconstruction of a signal containing discontinuities. As the signal is an infinite summation of sinusoidal basis functions, a discontinuity requires an infinite number of Fourier components in order to resolve. A finite number of Fourier terms yields spikes at the edges of the discontinuity as shown in Figure 6.5 which in Fourier space leads to spikes at sharp edges of a unit cell when reconstructed.

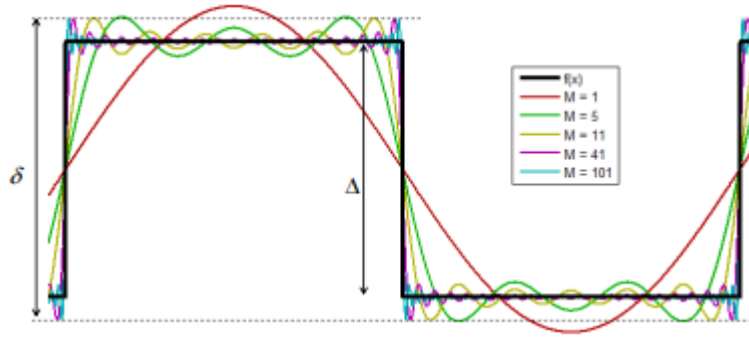


Figure 6.5: Illustration of Gibbs Phenomenon for a continuous time signal. The application to Fourier space is similar [105].

6.5 CONSTRUCTION OF LATTICE

With the spatial harmonics determined for the unit cell, an overall lattice can be constructed. Using the grating phase concept introduced in Eq. (6.6) the lattice can be built by calculating the Fourier series with the spatially variant parameters given by Eqs. (6.17) and (6.18). The dielectric function for the

overall grating is the Fourier series reconstruction for each of the spatial harmonics modified by the spatial variance parameters.

Creating a loop over each spatial harmonic, the modified grating vectors are formed by assigning the spatial harmonic uniformly throughout the grid, adding the angle of the orientation spatial variance parameter $\theta(\vec{r})$ to the angle of the and dividing by the period spatial variance parameter $\Lambda(\vec{r})$. Figure 6.6 shows a graphical representation of this process.

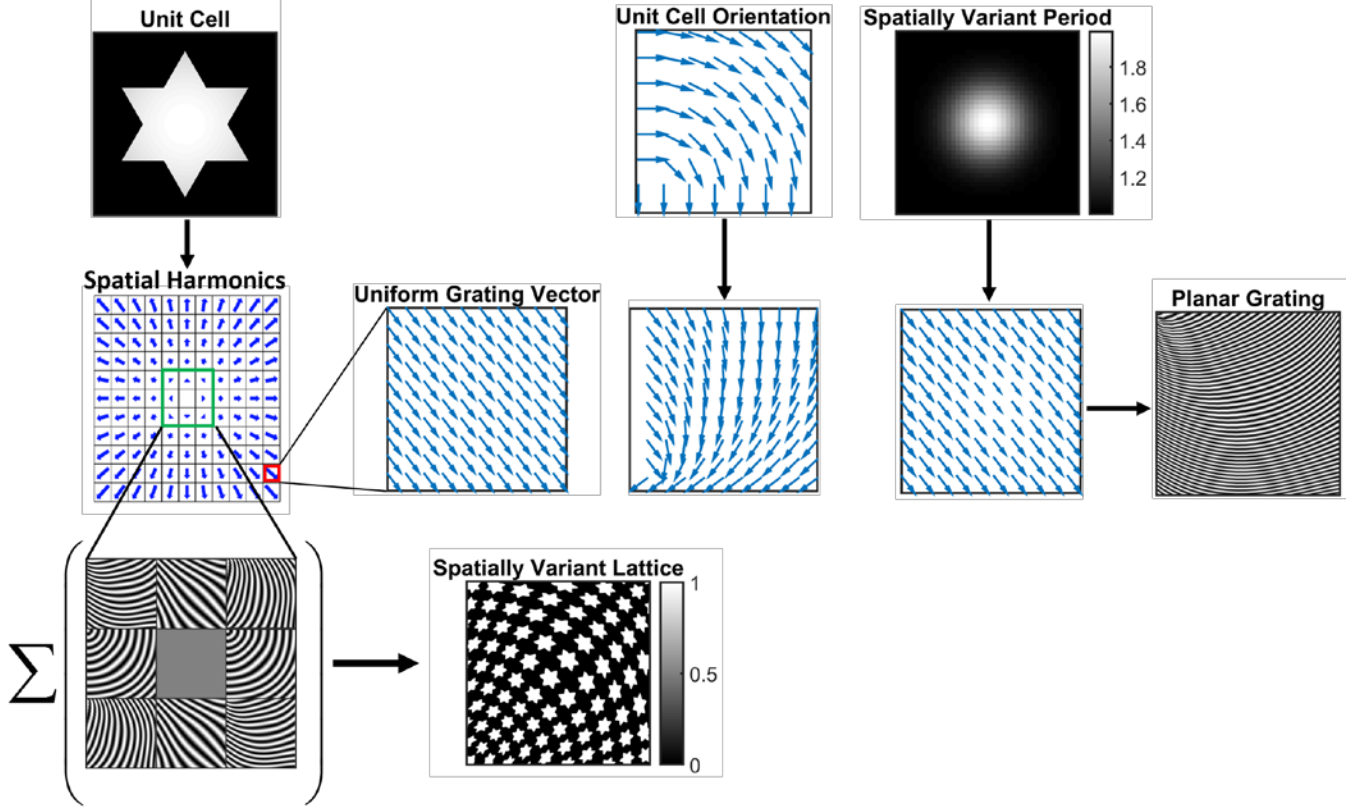


Figure 6.6: Graphical representation of method for determining spatially variant lattice grating vectors.

To construct the lattice, the grating phase must be calculated for each grating vector and reconstructed to form an overall lattice permittivity function given by

$$\varepsilon_{pq}(x_2, y_2) = a_{pq} \exp[j\Phi_{2,pq}(x_2, y_2)] \quad (6.22)$$

$$\varepsilon_{\text{analog}}(x_2, y_2) = \varepsilon_{\text{analog}}(x_2, y_2) + \text{Re}[\varepsilon_{pq}(x_2, y_2)]. \quad (6.23)$$

6.6 OPTIMIZATION OF THE ALGORITHM

6.6.1 Truncation of Spatial Harmonics by Magnitude

Fundamentally, the majority of energy in a signal which has been decomposed into its Fourier coefficient is contained within a minority of the infinite combination of harmonics. Limiting the reconstruction of a lattice to only those Fourier components which are above a threshold greatly reduces the time involved to synthesize a spatially variant lattice. Figure 6.7 shows an example of the real parts of the spatial harmonics for a unit cell. As can be seen on the left side of the figure, the majority of the spatial harmonics have negligible amplitude. Assigning a threshold in order to limit the number of harmonics used for the lattice construction leads to the result shown on the right. The overall number of spatial harmonics is dramatically reduced using this method and the time required to construct the lattice is reduced considerably.

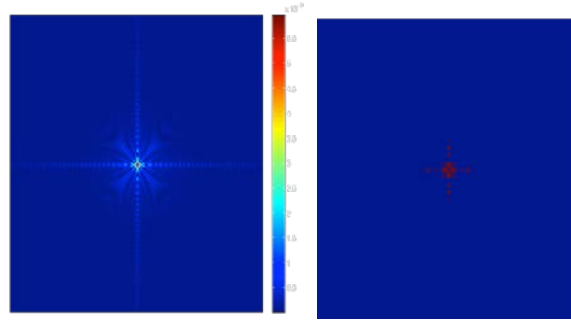


Figure 6.7: The left plot of this figure displays the real part of the spatial harmonics for a unit cell. On the right a threshold was set to eliminate all harmonics which exceeded this threshold.

6.6.2 Reduction by Collinear Spatial Harmonics

The spatial harmonics calculated for a unit cell contain amplitude and orientation information for all of the planar gratings composing the truncated Fourier series for that unit cell as shown in the left plot of Figure 6.8. Considering Eq. (6.20), the grating vector and the amplitude of each spatial harmonic must be used to assemble the unit cell using the Fourier series. Likewise, the grating phase and amplitude terms in Eq. (6.22) must be used to assemble the entire lattice. As the grating phase computation given by Eqs. (6.6) - (6.16) consider only the grating vector, the number of computationally expensive linear algebra operations and interpolations to the high resolution grid necessary can be reduced to only the minimal set of grating vectors by eliminating the collinear terms while retaining the amplitude information. With the

grating phase known, the lattice construction can use the phase calculated and simply apply the amplitude calculation for each of the reduced terms.

Reduce collinear

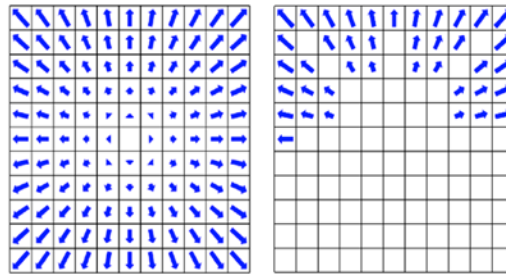


Figure 6.8: Spatial harmonics of a unit cell reduced to the minimum number of unique orientations by eliminating all collinear components.

Chapter 7: Demonstration of Transformation Optics and Spatially Variant Lattice Toolchain

7.1 COORDINATE TRANSFORMATION

The device chosen to be explored with this tool chain is the arbitrary electromagnetic cloak shown in Figure 7.1. To achieve cloaking a coordinate transformation must be employed which bends the coordinate axes around the object being cloaked. According to [19, 76, 77] this coordinate transformation can be achieved by stretching the center of the cloak to the boundary of the object being cloaked. The outer boundary of cloak remains the same in both coordinate systems.

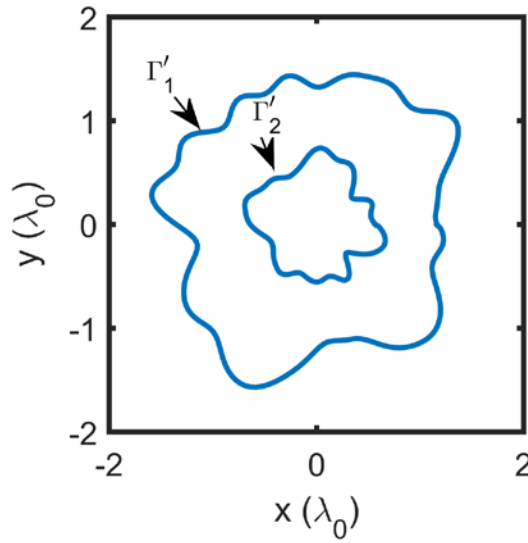


Figure 7.1: Boundaries of arbitrary electromagnetic cloak.

Due to the existence of singularities of the Jacobian matrix within the cloaked region, the reverse coordinate transformation of that described above was used. The boundary conditions to implement this reverse coordinate transformation are given by

$$\Gamma'_1(x, y) = \Gamma_1(x, y) \quad (7.1)$$

$$\Gamma'_2 = 0 \quad (7.2)$$

Following method described in Chapter 5 the coordinates x and y can be determined by solving Laplace's equation with the boundaries Γ'_1 and Γ'_2 . The forcing matrix \mathbf{F} which consists of 1's at those points where the boundaries exist and 0's elsewhere is defined for the boundary conditions (7.1) and (7.2). The two forcing vectors \mathbf{u}_x and \mathbf{u}_y contain the x and y coordinate, respectively, of each position

on the grid where the boundary is defined and are reshaped into column vectors. Using the second order centered finite-difference matrix operators given in Eq. (5.7) Laplace's equation can be written as shown in Eq. (5.10). Implementing Eqs. (5.11) - (5.13) using \mathbf{F} , \mathbf{u}_x , and \mathbf{u}_y leads to

$$\mathbf{L}'\mathbf{x} = \mathbf{b}_x \quad (7.3)$$

$$\mathbf{L}'\mathbf{y} = \mathbf{b}_y \quad (7.4)$$

where \mathbf{L}' is given in Eq. (5.12) and

$$\mathbf{b}_x = \mathbf{F}\mathbf{u}_x \quad (7.5)$$

$$\mathbf{b}_y = \mathbf{F}\mathbf{u}_y \quad (7.6)$$

Restricting the solution of Laplace's equation to the cloaking region, the modified form of Eqs. (7.3) and (7.4) are

$$\mathbf{L}''\mathbf{x}'' = \mathbf{b}_x'' \quad (7.7)$$

$$\mathbf{L}''\mathbf{y}'' = \mathbf{b}_y'' \quad (7.8)$$

Solving for \mathbf{x}'' and \mathbf{y}'' in Eqs. (7.7) and (7.8) leads to a column vector which was reshaped and used to replace the x and y coordinates in the original Cartesian grid. The resulting coordinate transformation is shown in Figure 7.2. Rather than the coordinate axes being directed around the cloaked object, the axes focus toward the center of the grid. This is due to the reverse coordinate transformation being used rather than the forward coordinate transformation.

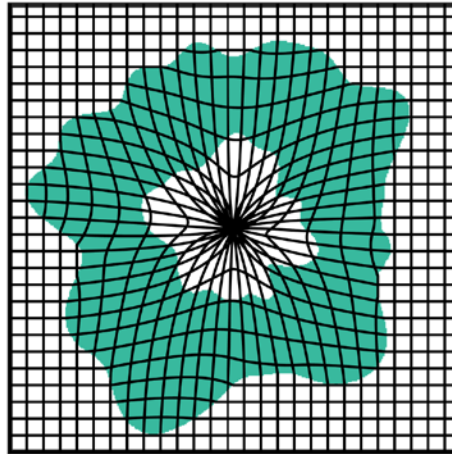


Figure 7.2: Coordinate axes for the reverse electromagnetic cloak coordinate transformation.

7.1.2 Jacobian Matrix

To calculate the Jacobian matrix for the coordinate transformation a numerical method for calculating the partial derivatives must be used. Referring to Eqs. (5.31) - (5.40), the partial derivatives can be expressed as finite-difference calculations. Using the matrix derivative operators $\mathbf{D}_{x'}$ and $\mathbf{D}_{y'}$, as described in Chapter 4, the partial derivatives required to calculate the Jacobian matrix can be determined and placed into arrays which contain the derivative values as shown in Figure 7.3.

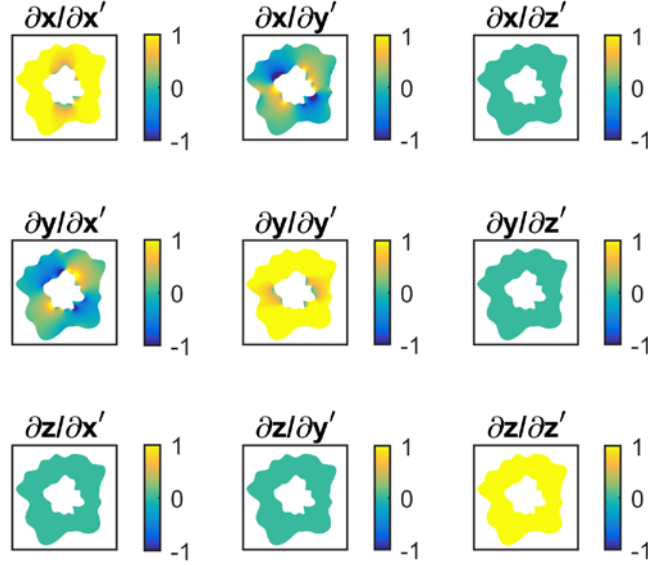


Figure 7.3: Derivatives of x and y coordinates calculated using Laplace's equation.

7.2 MATERIAL PARAMETERS

Using the Jacobian matrix, the permittivity and permeability tensors necessary for the electromagnetic cloak can be calculated using the equations of transformation optics [1, 2, 19, 20] according to

$$[\epsilon'_r] = \frac{\Lambda [\epsilon_r] \Lambda^T}{\det \Lambda} \quad (7.9)$$

$$[\mu'_r] = \frac{\Lambda [\mu_r] \Lambda^T}{\det \Lambda} \quad (7.10)$$

where $[\epsilon_r]$ and $[\mu_r]$ are the permittivity and permeability tensors of the physical space in the original coordinate system, Λ is the Jacobian matrix of the coordinate transformation, and Λ^T is the transpose of the Jacobian matrix. Iterating throughout the entire grid point by point, the Jacobian matrix is formed at each position in the grid using the derivative arrays shown in Figure 7.3. For the electromagnetic cloak

described in this chapter, the coordinate transformation was the opposite of that which is required for proper electromagnetic cloaking. As such, the inverse of the Jacobian matrix is necessary to compute the necessary material tensors. Using the matrix inverse of the Jacobian matrix at each point in the grid, the permittivity and permeability tensors are found according to Eqs. (7.9) and (7.10). Figure 7.4 shows the permittivity tensor of the cloak. Each element of the tensor is an array the size of the grid. From the Eqs. (7.9) and (7.10), the permeability for a device in free space is equal to the permittivity.

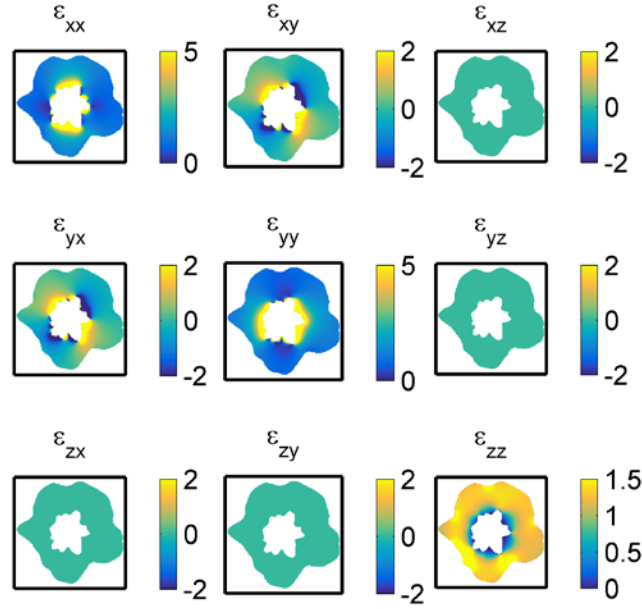


Figure 7.4: Arrays of permittivity tensor elements for the arbitrary electromagnetic cloak shown in Figure 7.1. The permeability will be identical to the permittivity.

7.3 DECOMPOSITION OF MATERIALS TO PRINCIPAL AXES

Based on the symmetry of the permittivity and permeability tensors [106] a coordinate system can be found in which the tensor is diagonal [106]. The diagonalized tensor is found by solving the eigenvalue problem

$$[\epsilon_r] \mathbf{P}_i = [\epsilon_d]_i \mathbf{P}_i \quad (7.11)$$

where \mathbf{P}_i is the eigenvector for the eigenvalue $[\epsilon_d]_i$. The orientations of the eigenvectors of Eq. (7.11) are known as the principal axes of the tensor [41].

For the permittivity and permeability tensors determined using Eq. (7.9) and (7.10) the tensor components and principal axes are shown in Figure 7.6. The permittivity value ϵ_c in the \hat{c} direction

becomes infinitely large approaching the center due to the existence of a singularity within the cloaked region. A convergence study was performed for the cloak to determine the optimal grid resolution such that the reflectance and transmittance of the device do not vary appreciably as a function of grid resolution. The cloak with parameters shown in Figure 7.6 was simulated using AFDFD with a grid resolution of $\lambda_0 / 100$. The results of this simulation are shown in Figure 7.7.

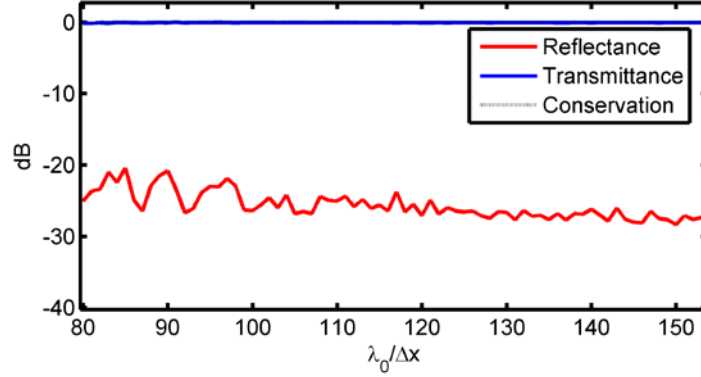


Figure 7.5: Convergence sweep of electromagnetic cloak. A value of $N_{RES} = \Delta x / \lambda_0$ above 100 is seen to be well converged.

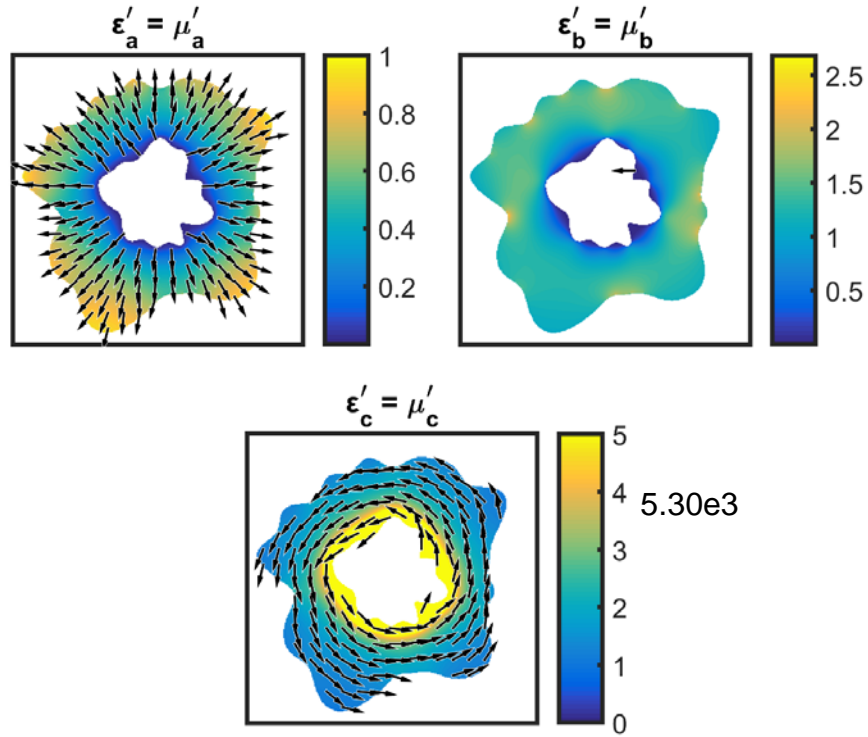


Figure 7.6: Principal axes and diagonalized permittivity tensor values along principal axes. The permittivity values ϵ_c in the direction of \hat{c} approach infinity near the center of the cloaking region.

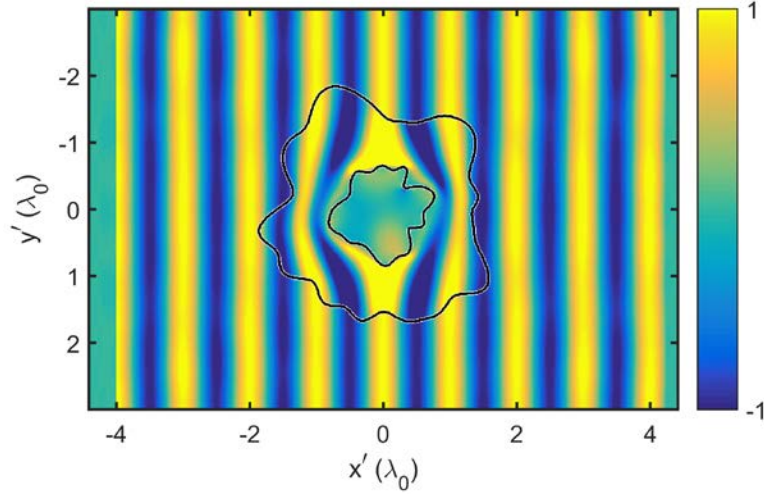


Figure 7.7: Result of AFDFD simulation of the cloak with the material tensors shown in Figure 7.6. This simulation was performed with a grid resolution of $\lambda_0/100$.

In order to design a physically realizable cloak, the values of the material parameters must be within the range of currently available metamaterial unit cells. The material parameters determined for this device require a six terms in order to fully implement it. By choosing a fixed electric field polarization the material terms can be reduced to a set of values with only two material values which vary with position as described in [18]. Consider an electric field vector in cylindrical coordinates polarized in the z direction as given in Eq. (7.12) and a magnetic field vector as given in Eq. (7.13)

$$\vec{E}(r, \phi) = E_z(r, \phi) \hat{z} \quad (7.12)$$

$$\vec{H}(r, \phi) = H_r(r, \phi) \hat{r} + H_\phi(r, \phi) \hat{\phi} \quad (7.13)$$

Taking the curl of Eqs.(7.12) and (7.13) leads to

$$\nabla \times \vec{E} = \frac{1}{r} \frac{\partial E}{\partial \phi} \hat{r} - \frac{\partial E}{\partial r} \hat{\phi} \quad (7.14)$$

$$\nabla \times \vec{H} = \left[\frac{1}{r} \frac{\partial}{\partial r} (r H_\phi) - \frac{1}{r} \frac{\partial H_r}{\partial \phi} \right] \hat{z} \quad (7.15)$$

Maxwell's curl equation for the electric field can be written as

$$\frac{1}{r} \frac{\partial E}{\partial \phi} \hat{r} - \frac{\partial E}{\partial r} \hat{\phi} = j\omega[\mu] \vec{H} = j\omega(\mu_r H_r \hat{r} + \mu_\phi H_\phi \hat{\phi}) \quad (7.16)$$

Solving for the components of \vec{H} from Eq. (7.16) yields

$$H_r = \frac{1}{j\omega\mu_r r} \frac{\partial E}{\partial \phi} \quad (7.17)$$

$$H_\phi = -\frac{1}{j\omega\mu_\phi} \frac{\partial E}{\partial r} \quad (7.18)$$

Likewise, Maxwell's curl equation for the magnetic field can be written

$$\left[\frac{1}{r} \frac{\partial}{\partial r} (r H_\phi) - \frac{1}{r} \frac{\partial H_r}{\partial \phi} \right] \hat{z} = -j\omega[\varepsilon] \vec{E} = -j\omega\varepsilon_z E_z \hat{z} \quad (7.19)$$

Substituting Eqs. (7.17) and (7.18) into Eq. (7.19) leads to

$$\left[\frac{1}{r} \frac{\partial}{\partial r} \left(-r \frac{1}{j\omega\mu_\phi} \frac{\partial E}{\partial r} \right) - \frac{1}{r} \frac{\partial}{\partial \phi} \left(\frac{1}{j\omega\mu_r r} \frac{\partial E}{\partial \phi} \right) \right] = -j\omega\varepsilon_z E \quad (7.20)$$

which can be simplified to yield the wave equation in terms of E as

$$\frac{1}{\mu_\phi \varepsilon_z} \frac{1}{r} \frac{\partial}{\partial r} \left(r \frac{\partial E}{\partial r} \right) + \frac{1}{\mu_r \varepsilon_z} \frac{1}{r^2} \frac{\partial^2 E}{\partial \phi^2} + \omega^2 E = 0 \quad (7.21)$$

Using the justification in [18] a set of parameters satisfying Eq. (7.21) can be found.

For a cylindrical cloak, the material parameters are given as

$$\begin{aligned} \varepsilon_z = \mu_z &= \left(\frac{b}{b-a} \right)^2 \frac{r-a}{r} \\ \varepsilon_r = \mu_r &= \frac{r-a}{r} \\ \varepsilon_\phi = \mu_\phi &= \frac{r}{r-a} \end{aligned} \quad (7.22)$$

According to [18], the following set of material parameters will satisfy the wave equation for the electric field polarized in the z direction.

$$\begin{aligned} \varepsilon'_z &= \left(\frac{b}{b-a} \right)^2 \\ \mu'_r &= \left(\frac{r-a}{r} \right)^2 \\ \mu'_\phi &= 1 \end{aligned} \quad (7.23)$$

Comparing Eqs. (7.22) and (7.23) one can see that

$$\begin{aligned} \varepsilon'_z &= \varepsilon_z \mu_\phi \\ \mu'_r &= \mu_r \mu_r \\ \mu'_\phi &= \mu_\phi \mu_r \end{aligned} \quad (7.24)$$

Following a similar approach, another set of parameters can be found similar to those in (7.24).

$$\begin{aligned}\varepsilon'_z &= \varepsilon_z \mu_r \\ \mu'_r &= \mu_r \mu_\phi \\ \mu'_\phi &= \mu_\phi \mu_\phi\end{aligned}\tag{7.25}$$

which for a cylindrical cloak are

$$\begin{aligned}\varepsilon'_z &= \left(\frac{b}{b-a}\right)^2 \left(\frac{r-a}{r}\right)^2 \\ \mu'_r &= 1 \\ \mu'_\phi &= \left(\frac{r}{r-a}\right)^2\end{aligned}\tag{7.26}$$

Applying the relations in Eq. (7.25) to the diagonalized material parameters shown in Figure 7.6 leads to the parameters shown in Figure 7.8. Of note is the range of values shown for the μ_ϕ parameter. For a grid with infinitely small cells, the material values approach infinity. A realistic upper limit must be found in order to physically realize this device.

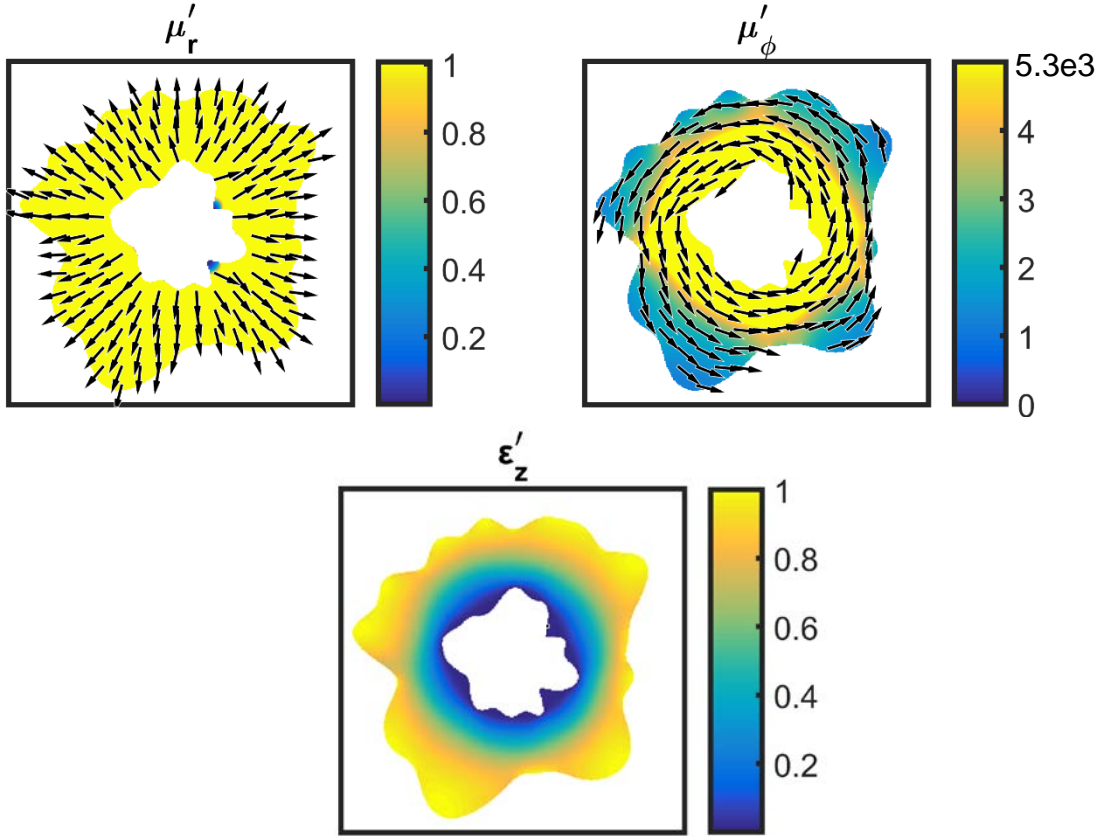


Figure 7.8: Simplified material parameters for metamaterial cloak.

A study was performed on the effect limiting the upper bounds of values in the permittivity and permeability tensors. By limiting the maximum value of the material values to 5, a cloak with performance comparable to the cloak without limitations was able to be simulated. Rotating the tensors using the reduced elements shown in Figure 7.8 according to [107]

$$[\varepsilon_r] = R[\varepsilon_d]R^{-1} \quad (7.27)$$

where R is the rotation matrix composed of the principal axes as given by

$$R = \begin{bmatrix} a_x & b_x & c_x \\ a_y & b_y & c_y \\ a_z & b_z & c_z \end{bmatrix} \quad (7.28)$$

leads to a cloak which when simulated using AFDFD is shown in Figure 7.9.

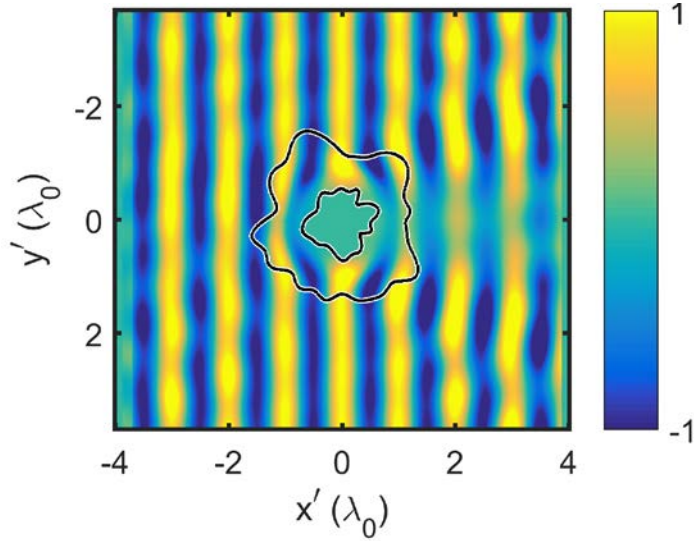


Figure 7.9: Cloak constructed using reduced permittivity and permeability values as shown in Figure 7.8 simulated using AFDFD with a grid resolution of $\lambda_0 / 80$

7.4 METAMATERIAL MAPPING

Using the constrained tensor elements described in the previous section and shown in Figure 7.8, metamaterials engineered to the proper material value at each point in the grid are selected to construct the device. After a study of several metamaterial unit cells, it was determined that the *magnetic-electric LC* (MELC) structure presented in [108] provided the widest range of values applicable to this device. This structure, shown in Figure 7.10, provides a wide range of material values for two structures

oriented in a mirrored arrangement as shown on the right side of Figure 7.10. The effective material parameters for the MELC structure with both scale1 and scale2 equal to 1 is shown in Figure 7.11 as a function of frequency.

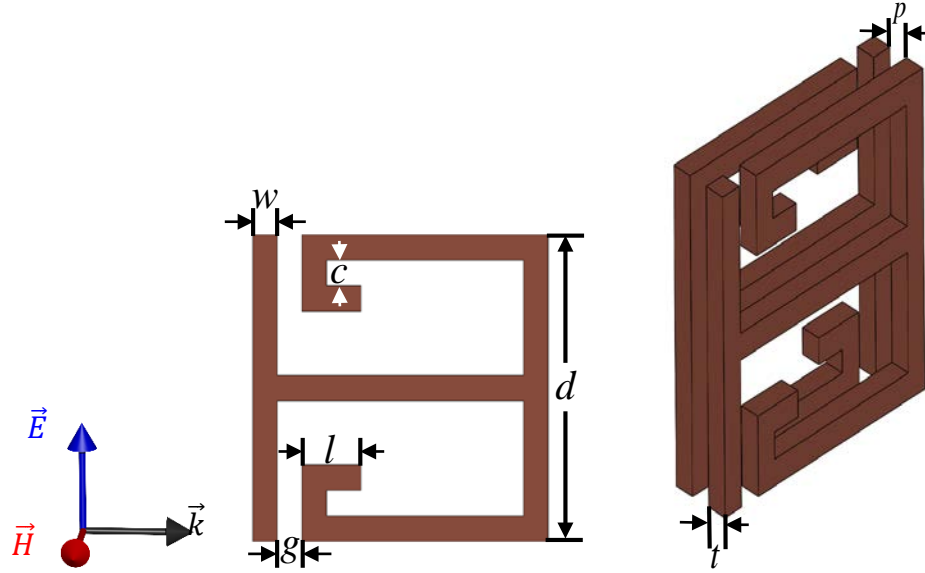


Figure 7.10: MELC unit cell with the dimensions $d = 3.0 \text{ mm}$, $w = 0.25 \text{ mm}$, $g = 0.25 \text{ mm}$, $l = 0.6 \text{ mm}$, $c = 0.25 \text{ mm}$. The spacing between structures is $p = 0.25 \text{ mm}$ and the conductor thickness is $t = 0.25 \text{ mm}$.

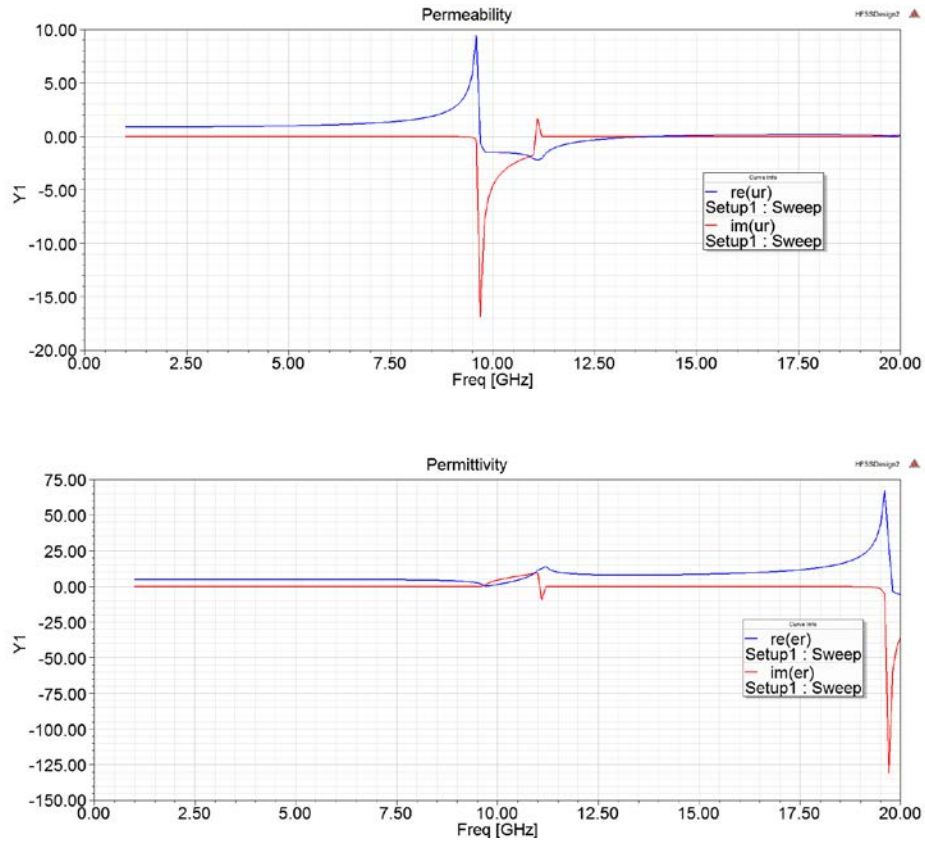


Figure 7.11: Effective material parameter sweeps for the MELC structure shown in Figure 7.10.

In order to fully characterize the MELC metamaterial element a parameter sweep was performed by scaling the x and z dimensions of both of the mirrored elements from 0.01 times the nominal dimensions to 1.0 times the nominal values in 0.01 increments using Ansys HFSS [30]. The sweeps resulted in a two dimensional map of the permittivity and permeability values retrieved for the metamaterial cell as a function of scale1 and scale2. The real part of this parameter sweep is shown in Figure 7.12 while the imaginary part of the sweep is shown in Figure 7.13.

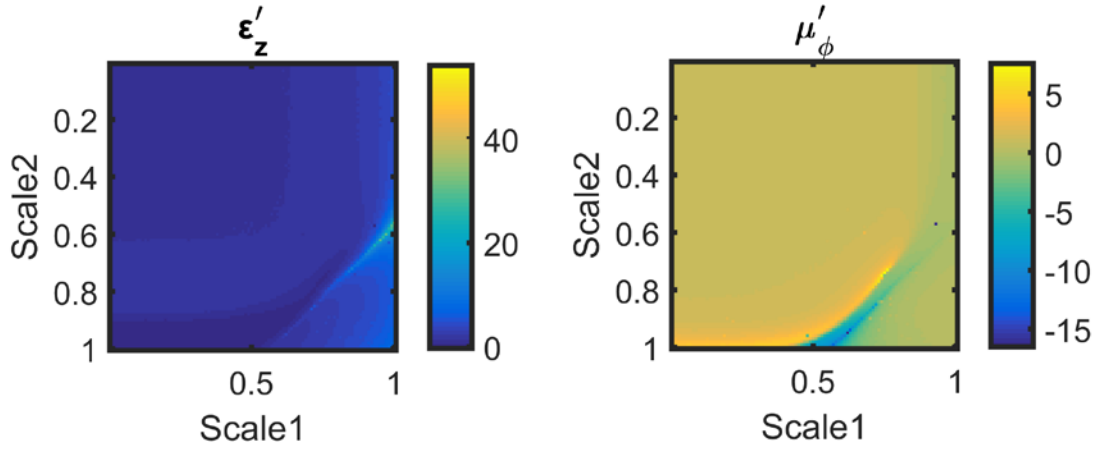


Figure 7.12: Real part of the material parameters from the scaling sweep for the MELC metamaterial unit cell.

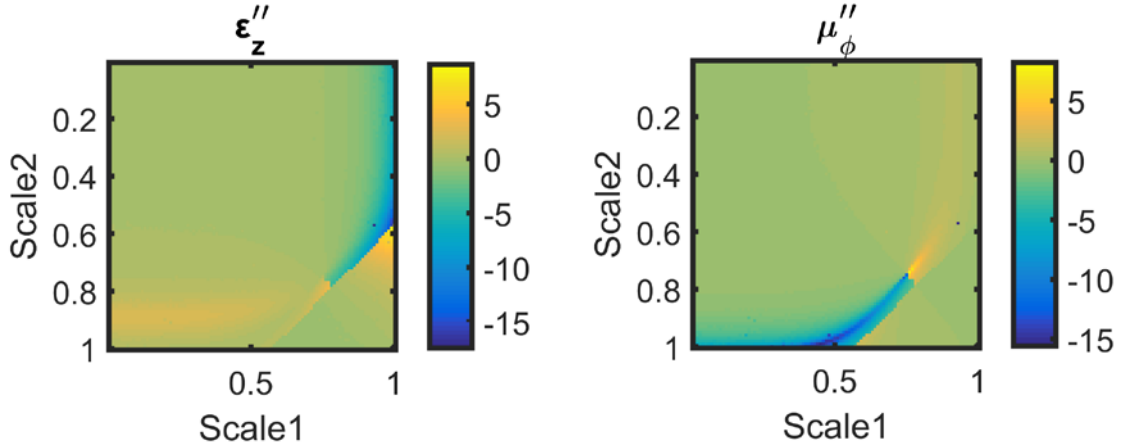


Figure 7.13: Imaginary part of the material parameters from the scaling sweep for the MELC metamaterial unit cell.

The scaling for each position within the device is determined by first calculating the absolute difference between the permittivity or permeability value at that position and the material values for the metamaterial which will be implemented for that material as given in Eqs. (7.29) and (7.30).

$$\Delta \varepsilon_z(i, j) = \left| \varepsilon_z(i, j) - \varepsilon'_{\text{map}} \right| \quad (7.29)$$

$$\Delta \mu_\phi(i, j) = \left| \mu_\phi(i, j) - \mu'_{\text{map}} \right| \quad (7.30)$$

The differences are added together and the scales corresponding to the minimum are stored for each position in the device.

Consider the map of the material parameters of the device evaluated at the point (0.016, 0.048) as shown in Figure 7.14. The value of ε_z at this position is 0.9817 and that of μ_ϕ is 1.983. Applying

Eqs. (7.29) and (7.30) leads to the difference terms shown in Figure 7.15. The sum of these difference terms is shown on the left in Figure 7.16 and on the right this term is plotted logarithmically to graphically show the minimum scales of $\text{scale1} = 0.59$ and $\text{scale2} = 0.84$. These scale values correspond to a value of 0.986 for ϵ_z and 1.983 for μ_ϕ .

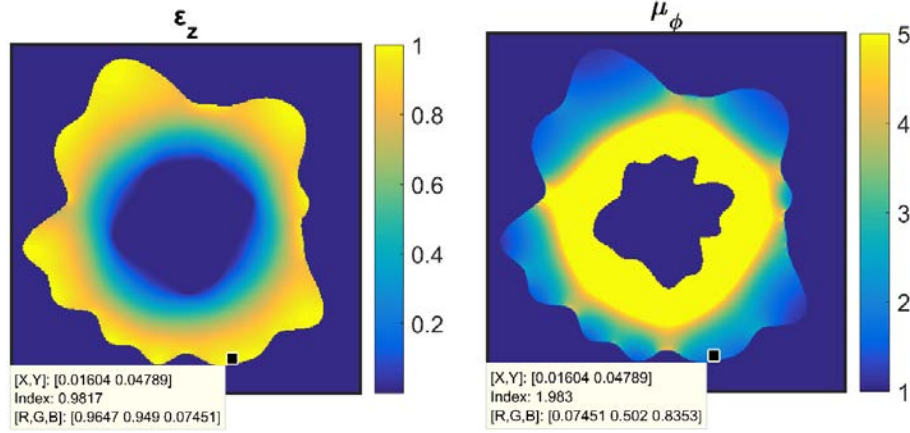


Figure 7.14: Plot of the device material parameters with a cursor at the position $(0.016, 0.048)$.

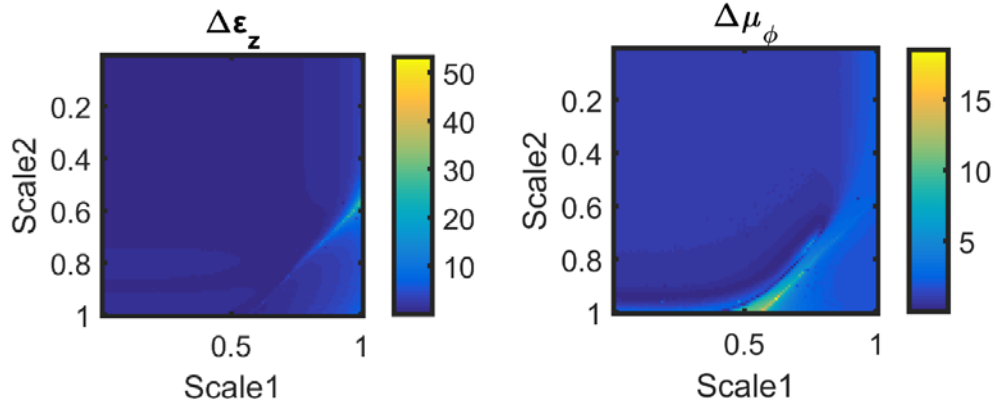


Figure 7.15: Difference terms for the material values for the position $(0.016, 0.048)$ in the device.

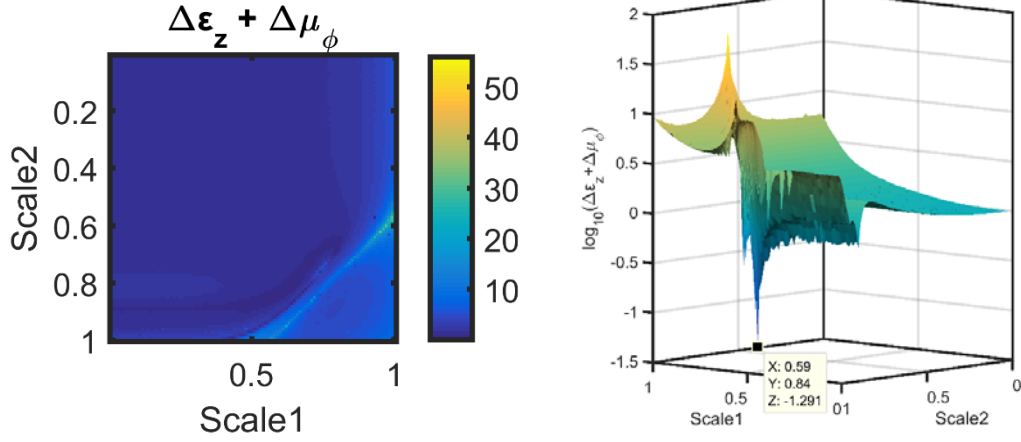


Figure 7.16: Combined material differences shown on the left. On the right the combined differences are plotted on a logarithmic scale and the minimum scale values are shown with a data cursor.

Mapping the material parameters to each point in the grid the scale factors for the MELC structures were determined. Figure 7.17 shows the final mapping used for the electromagnetic cloak. The terms labeled “Fit μ_ϕ ” and “Fit ϵ_z ” are the material parameter values for the scales which were determined to be the closest match to those necessary for the cloak. Figure 7.18 shows the AFDFD simulation for using only the real part of the material parameters. Comparing this simulation to the reduced parameter model of the electromagnetic cloak presented in [18] shown in Figure 7.19 demonstrates that the reduced material model for the arbitrary electromagnetic cloak with the fit material values is a very good approximation.

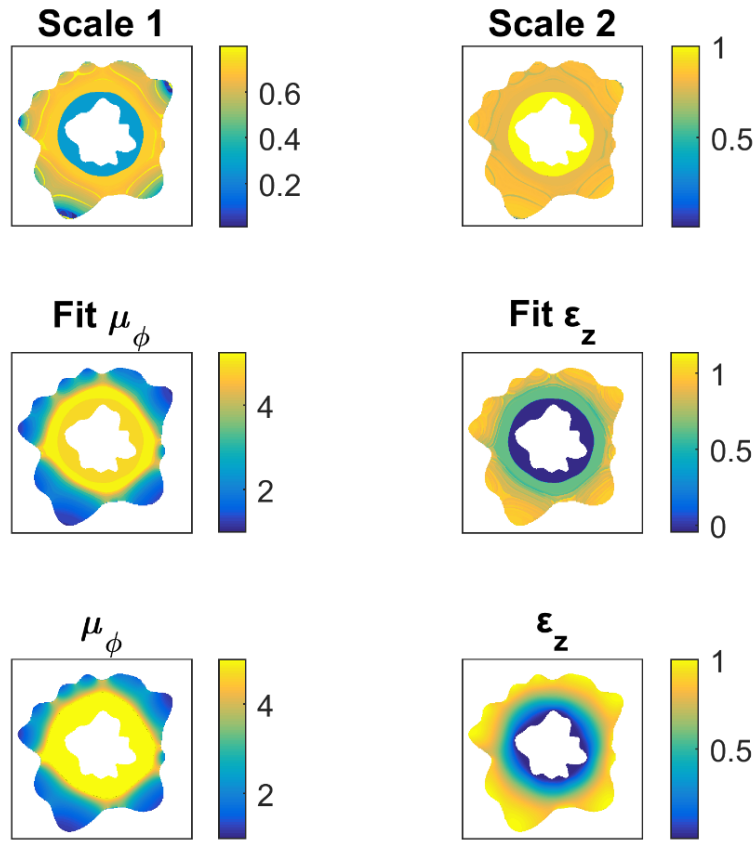


Figure 7.17: Metamaterial mapping for the electromagnetic cloak.

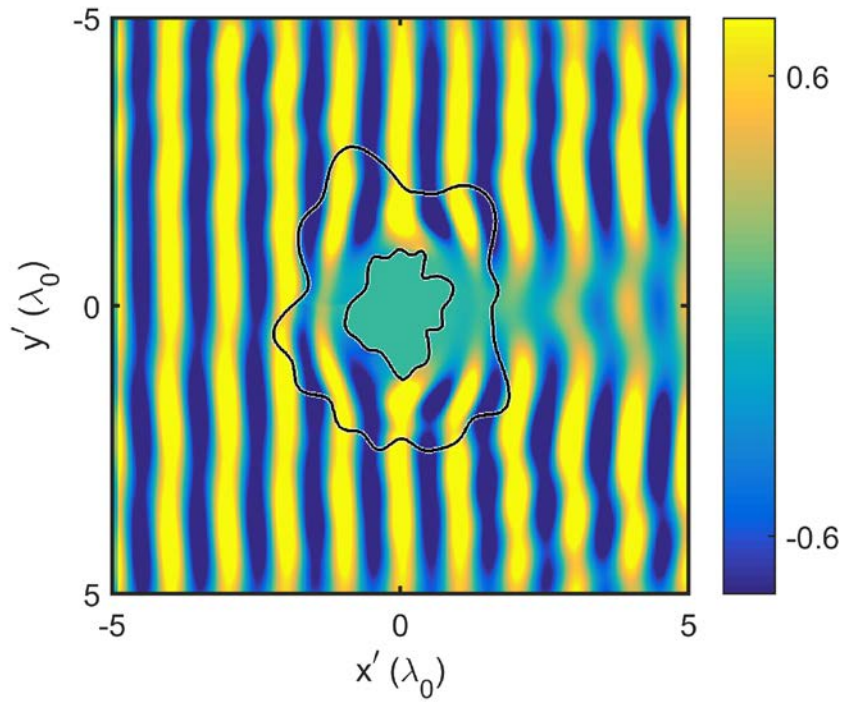


Figure 7.18: AFDFD simulation of electromagnetic cloak with only the real part of the material parameters used.

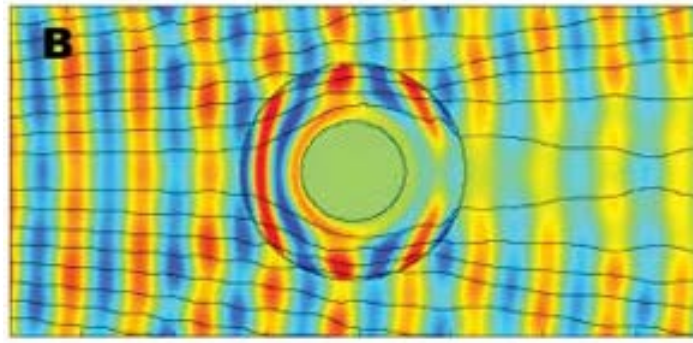


Figure 7.19: Reduced material model for electromagnetic cloak described in [18].

7.5 SPATIALLY VARIANT METHOD FOR NON-UNIFORM AND CIRCULATING GRIDS

With the metamaterial scaling and orientations determined, the placement of the elements was implemented. Using the spatially variant lattice synthesis tool described in Chapter 6 as well as in Refs. [81, 97, 99, 101] the metamaterial elements were smoothly and continuously placed according the unit cell period and orientation derived previously. The traditional spatially variant algorithm decomposes the unit cells into spatial harmonics which are then spatially varied and reconstructed. The metamaterial element used for this research would require thousands of spatial harmonics to resolve the very fine features of the unit cell, due to the existence of Gibb's phenomenon as discussed previously in Chapter 6. Rather than use this approach, an alternative method of distributing the metamaterial elements was formulated. This approach used three grating vectors composed of the principal axes of the transformation media tensors to create a spatially variant lattice. The spatially variant lattice formed by using the traditional spatially variant algorithm presented in Chapter 6 led to a lattice with a considerable amount of divergence due to the circulating nature of the principal axes. Designing a circulating grid with non-uniform grid spacing, as shown in Figure 7.20, minimized the divergence of the unit cells.

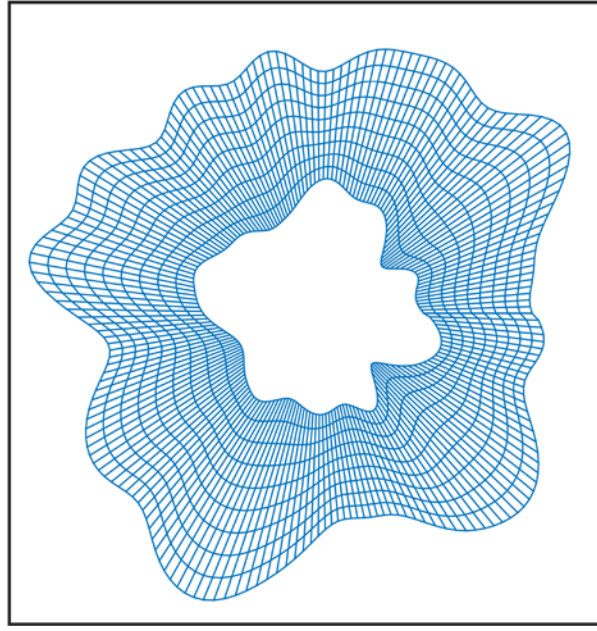


Figure 7.20: Implementation of the Spatially Variant algorithm on a non-uniform grid.

To construct the spatially variant lattice, the principal axes of the material tensors, shown in Figure 7.8, were used to construct the spatially varying grating vectors. These grating vectors were used to calculate the grating phase according to

$$\nabla\Phi(\vec{r}) = \vec{K}(\vec{r}) \quad (7.31)$$

which, referring to Chapter 6, can be written using finite-difference operators to be

$$\begin{bmatrix} \mathbf{D}_x \\ \mathbf{D}_y \end{bmatrix} \Phi = \begin{bmatrix} \mathbf{k}_x \\ \mathbf{k}_y \end{bmatrix} \quad (7.32)$$

for a two-dimensional device. However, on a non-uniform grid the finite-difference operators \mathbf{D}_x and \mathbf{D}_y must be calculated differently than previously described for a uniform Cartesian grid because the Δx and Δy values are constant for the Cartesian derivative operator and varying for the non-uniform grid.

Considering the cutaway section shown in Figure 7.21, for each point in the grid a curve-fitting approximation is made such that

$$\Phi_i(x, y) \approx ax + by + c. \quad (7.33)$$

Taking the first derivative of Eq. (7.33) with respect to x leads to

$$\frac{\partial \Phi_i(x, y)}{\partial x} = a \quad (7.34)$$

and the first derivative with respect to y yields

$$\frac{\partial \Phi_i(x, y)}{\partial y} = b. \quad (7.35)$$

Referring to Figure 7.21, At each grid position a system of equations is constructed using Eq. (7.33) evaluated for the position being evaluated and the points on the grid adjacent to the point being evaluated. This system of equation is written as a matrix equation given by

$$\begin{bmatrix} \Phi_1 \\ \Phi_2 \\ \vdots \\ \Phi_n \end{bmatrix} = \begin{bmatrix} x_1 & y_1 & 1 \\ x_2 & y_2 & 1 \\ & \vdots & \\ x_n & y_n & 1 \end{bmatrix} \begin{bmatrix} a \\ b \\ c \end{bmatrix} \quad (7.36)$$

The positions on the grid that do not have neighboring points existing on the grid, such as the point labeled Φ_2 in Figure 7.21, require boundary conditions to be applied. In the case of this implementation Neumann boundaries [73] are applied in order to maintain a smooth and continuous boundary.

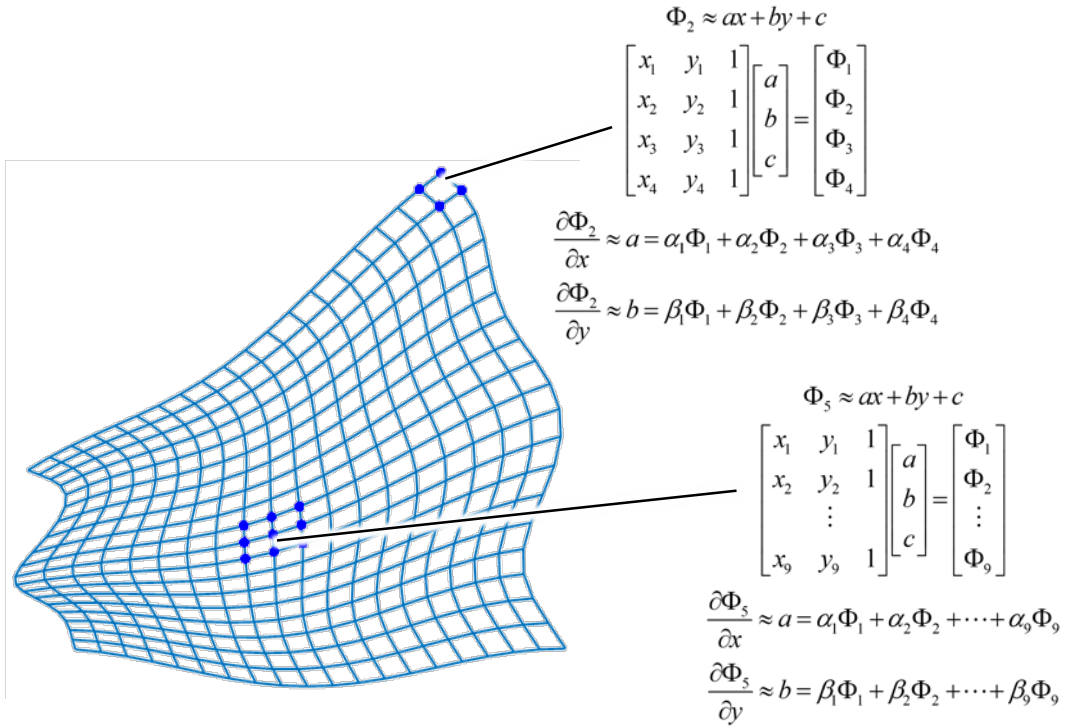


Figure 7.21: Expanded view of a section of the non-uniform grid shown in Figure 7.20.

Rewriting Eq. (7.36) using the Moore-Penrose pseudoinverse [109] leads to

$$\begin{bmatrix} x_1 & y_1 & 1 \\ x_2 & y_2 & 1 \\ & \vdots & \\ x_n & y_n & 1 \end{bmatrix}^{-1} \begin{bmatrix} \Phi_1 \\ \Phi_2 \\ \vdots \\ \Phi_n \end{bmatrix} = \begin{bmatrix} a \\ b \\ c \end{bmatrix} \quad (7.37)$$

Comparing Eq. (7.37) with Eqs. (7.34) and (7.35) the following relations can be made

$$\frac{\partial \Phi_i(x, y)}{\partial x} \approx a = \alpha_1 \Phi_1 + \alpha_2 \Phi_2 + \dots + \alpha_n \Phi_n \quad (7.38)$$

$$\frac{\partial \Phi_i(x, y)}{\partial y} \approx b = \beta_1 \Phi_1 + \beta_2 \Phi_2 + \dots + \beta_n \Phi_n \quad (7.39)$$

where the components α_j and β_k are the components of the first and second rows respectively of the pseudoinverse matrix. The finite-difference matrices are constructed by placing the values of α_j and β_k in the i^{th} row in the columns belonging to the positions Φ_j and Φ_k .

With the finite-differences calculated, the spatially variant tool was implemented as described in Chapter 6. Two spatially variant planar gratings were calculated as shown in Figure 7.22 using the principal axes of the material tensors as the grating vectors for each planar grating. The two planar gratings were added together to calculate the spatially variant lattice shown in Figure 7.23. From this lattice, the metamaterial element positions were determined.

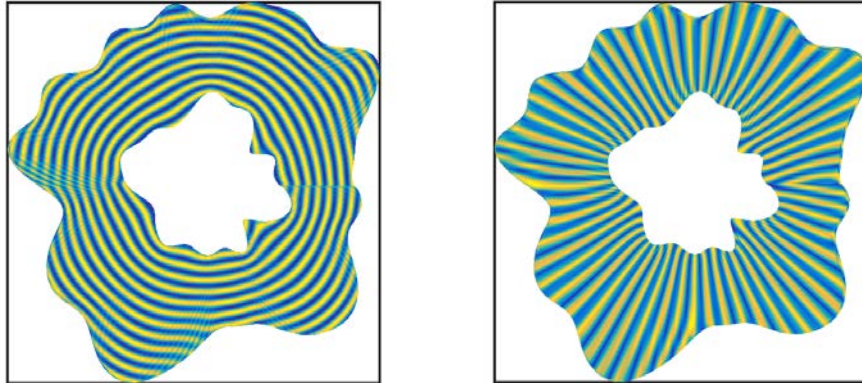


Figure 7.22: Grating vectors derived using spatially variant planar gratings with principal axes as the grating vectors.

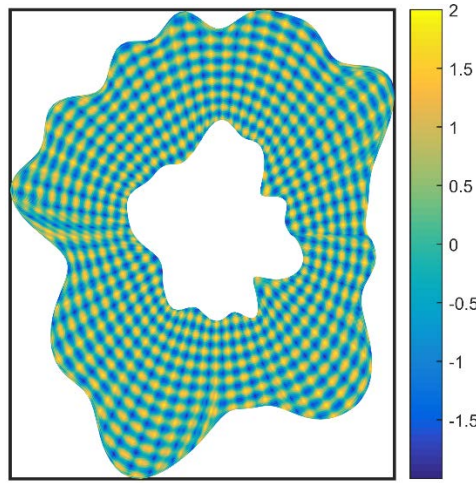


Figure 7.23: Sum of the planar gratings shown in Figure 7.22.

7.6 HYBRIDIZATION OF TRANSFORMATION OPTICS AND SPATIALLY VARIANT LATTICES

With the construction of the spatially variant planar lattice as described in the previous section, the metamaterial elements which were required to implement the transformation optics media could be placed within the device. By applying a threshold function to the spatially variant lattice shown in Figure 7.23 a binary lattice was created. The threshold function provided a value of 1 for every position with a value greater than the threshold of 1.0 and 0 for each position less than the threshold value. The resulting binary lattice is shown in Figure 7.24.

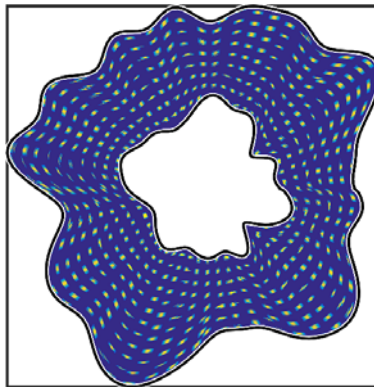


Figure 7.24: Intersection of planar gratings shown in Figure 7.23 determined using a threshold of 1.0.

To determine the position, orientation, and scaling of the metamaterial elements in the device, the values of 1 in the binary lattice were iterated through. For each position the cells adjacent to the position being evaluated were checked to determine if their values were also 1. This process continued

until a grouping of cells was obtained with no adjacent cells containing a value of 1 as shown in Figure 7.25. The center of this group of cells was determined and the position of the center was designated as the position where the center of a metamaterial element would be placed. The orientation of the metamaterial element was determined by interpolating the angle of principal axes at the position where the element will be placed. Likewise, the scaling for the metamaterial element is calculated by interpolating the scales resulting from the material mapping to the position where the metamaterial element will be positioned.

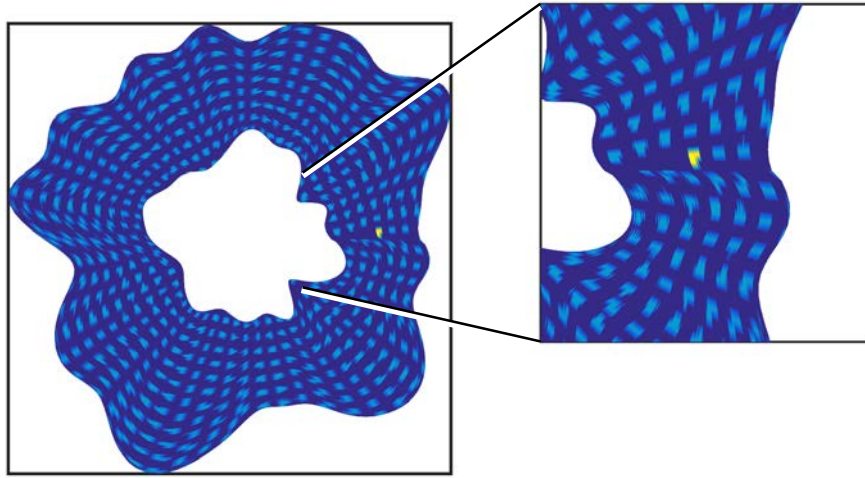


Figure 7.25: Cut out of grating intersection grid showing cell grouping.

Using the center positions, orientation, and scale values, the metamaterial unit cells were distributed throughout the device. The geometry for the metamaterial elements were stored in *Standard Tessellation Language* (STL) format for each half of the mirrored MELC unit cell. An STL file stores the information about the object as a series of faces and vertices. The faces and vertices for both elements were loaded into MATLAB and positioned appropriately for a nominal unit cell configuration. For each position identified on the spatially variant lattice, each of the mirrored halves of the metamaterial element was scaled per the scaling at the position where the elements were placed. Next, a rotation matrix was formed using the orientation at the location and the vertices were rotated using a rotational transformation. Finally, the vertices were translated to the position and the resulting faces and vertices were stored in a global array containing the faces and vertices of each element in the device.

Once all the positions of intersection in the spatially variant lattice had been evaluated this global array was written to an STL file. The final device with all the elements positioned properly is shown in Figure 7.26.

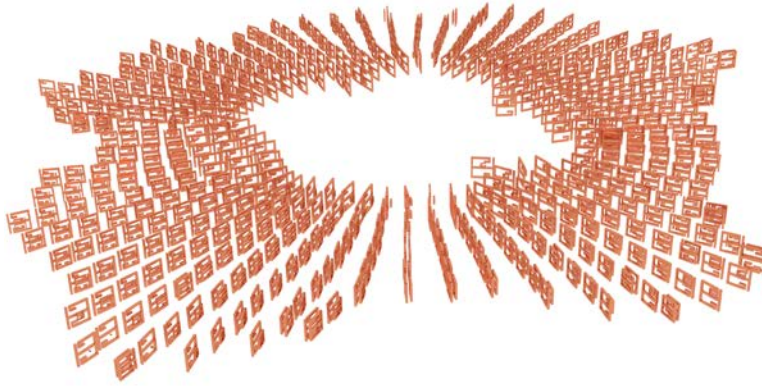


Figure 7.26: Final cloak designed using transformation optics hybridized with spatially variant metamaterials.

To illustrate the benefit of using a spatially variant lattice on a non-uniform and circulating grid, the device designed above was implemented using a Cartesian grid. First, a uniform lattice of points spaced with the lattice spacing of the nominal MELC unit cell (3.333 mm) was created as shown in Figure 7.27. This uniform lattice was masked with the outline of the cloaking device shown in Figure 7.1. The resulting lattice is shown in Figure 7.28.

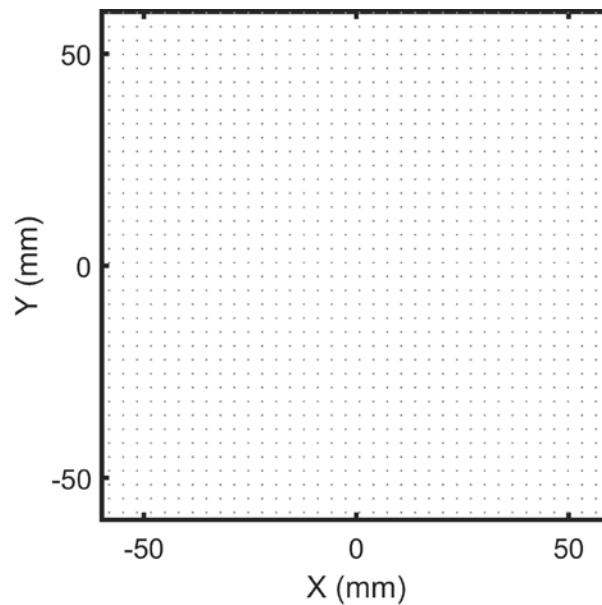


Figure 7.27: Uniform lattice with lattice spacing of MELC element described in Section 7.4.

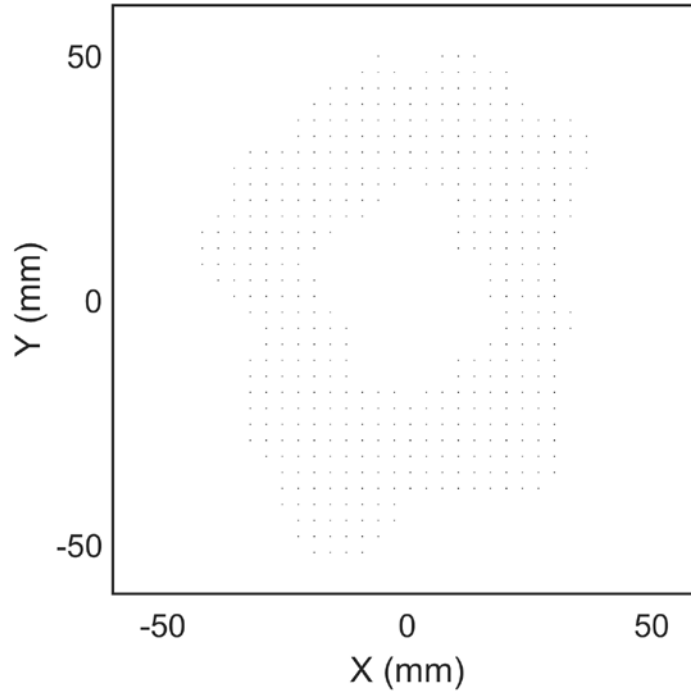


Figure 7.28: Cartesian lattice of metamaterial positions for transformation optics cloak boundaries shown in Figure 7.1.

Using the algorithm described previously in this chapter, the position, orientation, and scaling were determined using the Cartesian lattice in Figure 7.28. The metamaterial elements were placed using the method described for the spatially variant lattice previously and the resulting device is shown in Figure 7.29. The Cartesian cloak has several deficiencies when compared to the device designed using the spatially variant lattice. Firstly, the boundaries are abrupt due to the device being fixed to a Cartesian grid. The spatially variant device conforms to the boundaries of the cloak, whereas the Cartesian cloak has very sharp features because of the rectangular grid on which the materials are placed. Another drawback of the Cartesian device is that the effective material properties of the metamaterial elements are dilute when they undergo a rotation. This is because the Cartesian grid does not compensate for the rotation of the unit cell, but only the material elements. The rotation of the metamaterial unit cells is used in the construction of the grating vectors for the spatially variant lattice, therefore the overall device designed using the spatially variant lattice does not exhibit the dilution of the material properties. Finally, the Cartesian lattice cannot accommodate a spatially variant lattice

spacing. Like the rotation of the unit cells mentioned previously, the lattice spacing is a component of the grating vectors used to construct the spatially variant lattice.

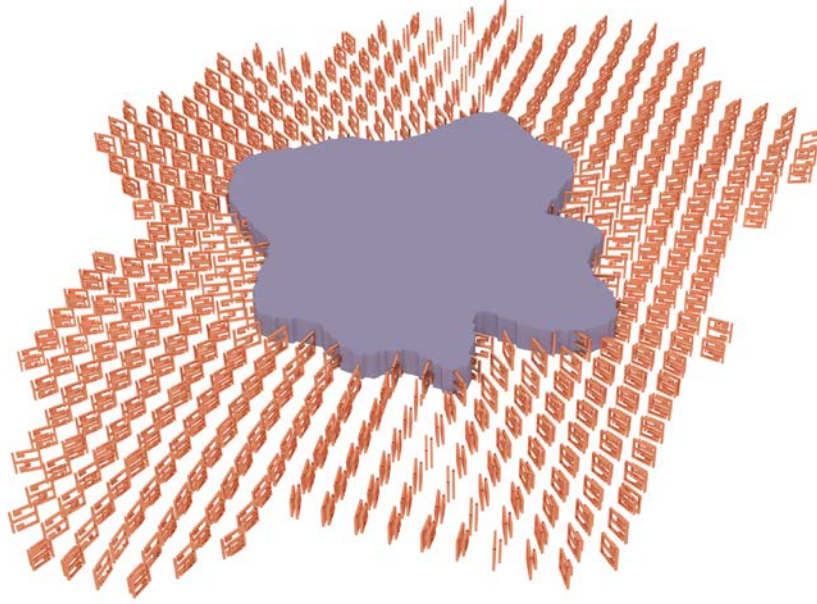


Figure 7.29: Transformation optics cloak with metamaterial elements arranged according to the Cartesian lattice shown in Figure 7.28.

7.7 METAMATERIAL DEVICE SIMULATION

To verify the effectiveness of the metamaterial cloak shown in Figure 7.26 a means of simulating of the entire structure is necessary. FDTD chosen because the memory required for this method scales for large grids better than other methods such as *Finite Element Method* (FEM) and FDFD [110]. VORPAL VSim particle simulation software from Tech-X [111] was used to perform the simulation of the discrete element cloak shown in Figure 7.26. The STL file created for the device was imported into VSim with uniaxial perfectly matched layer boundary conditions on all sides. The result of the simulation shown in Figure 7.30 does not perform as cleanly as the effective media cloak due to the losses inherent in the metamaterial unit cells. Comparing the cloak designed in this work with that presented in Ref. [18] the limitations of currently existing metamaterial elements is evident. With advances in metamaterial research the devices which can be realized will become more effective and a greater variety of devices will be able to be designed.

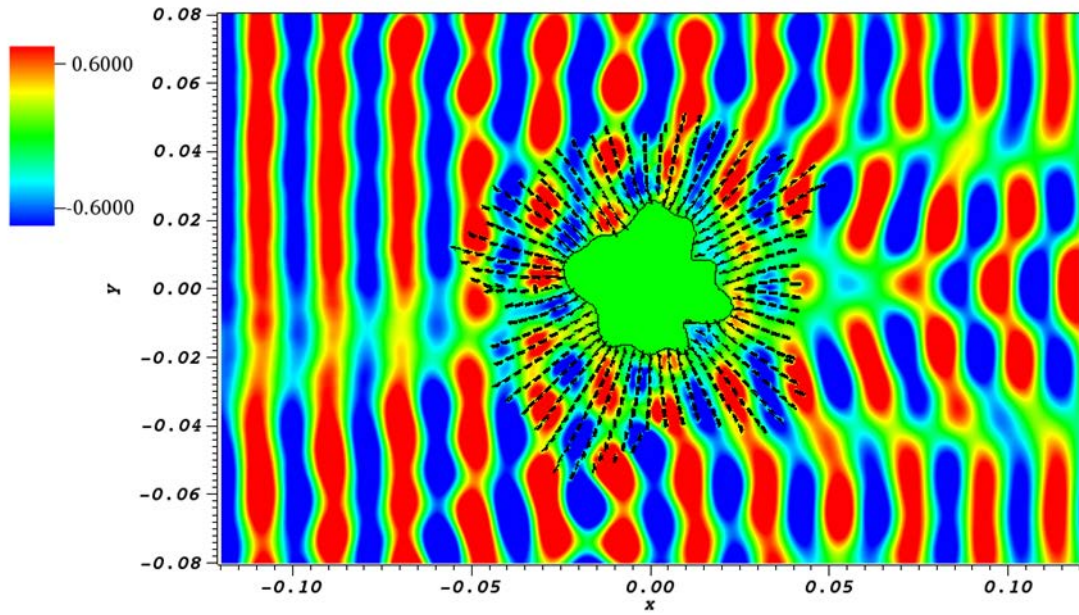


Figure 7.30: FDTD simulation of cloak shown in Figure 7.26 performed using VSim from Tech-X Corp.

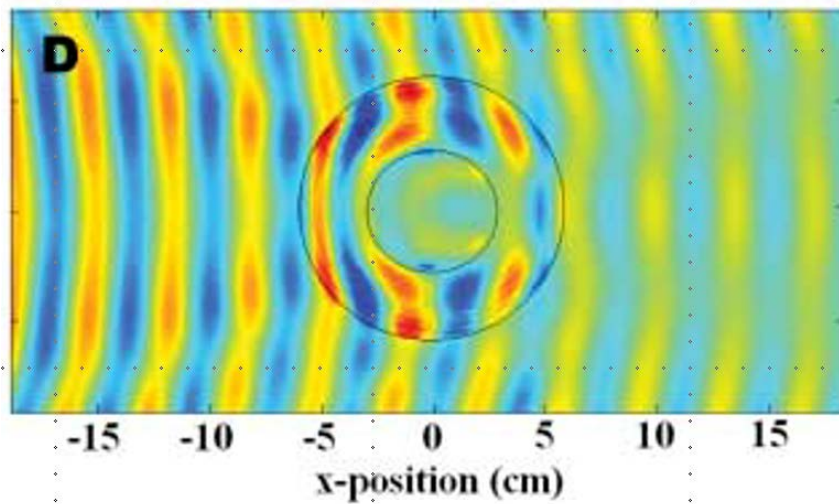


Figure 7.31: Discrete element experimental result of cloak designed in Ref. [18]

Chapter 8: Conclusion

The ability to spatially vary metamaterials to implement transformation electromagnetic devices will allow devices to be designed that are currently not realizable. A technique to generate transformation optics devices numerically using a simple finite-difference method was presented. By generating transformation media using a fully numerical approach, it is possible to design devices with arbitrary geometries defined only by the device boundaries. Additionally, the tools to simulate the effective media models using the Finite Difference Time Domain and the Anisotropic Finite Difference Frequency Domain methods is presented. An improvement to the AFDFD method was presented which reduces the amount of memory required to execute the simulation while also greatly reducing the time necessary to simulate a device. A discussion of metamaterial characterization was also presented. The process of simulating the material as well as extracting the material parameters from the scattering parameters. By scaling the metamaterials, the resonant frequency will shift and allow for a wide range of response at a single frequency.

A method of determining the scaling for each metamaterial element corresponding to the material parameter to be represented was presented. Spatially variant lattices were discussed as a method of placing the discrete metamaterial elements within the grid. A process of determining spatially variant planar gratings on a circulating non-uniform grid was used discussed. This technique allows devices to be constructed using grid sizes which vary throughout the grid. Identifying the intersections of the planar gratings created determines the positions that the metamaterial elements will be assigned within the device. The orientation and scale of the elements is calculated by interpolating the values found by the mapping operation and principal axes to the position identified by the intersection of the gratings. The final device designed using this method is then simulated in a full-wave solver such as FDTD.

The comparison between the effective media model and the discrete element device was made and a discussion of the results was presented. While the method presented in this research will produce a device based on the material parameters determined through transformation optics, the effectiveness of

such a device is limited by the metamaterials which are available to implement it. As metamaterials are designed with more bandwidth and lower loss, the devices which will be possible will expand.

References

- [1] J. B. Pendry, D. Schurig, and D. R. Smith, "Controlling electromagnetic fields," *science*, vol. 312, pp. 1780-1782, 2006.
- [2] D.-H. Kwon and D. H. Werner, "Transformation electromagnetics: an overview of the theory and applications," *Antennas and Propagation Magazine, IEEE*, vol. 52, pp. 24-46, 2010.
- [3] U. Leonhardt and T. G. Philbin, "Transformation optics and the geometry of light," *Progress in Optics*, vol. 53, pp. 69-152, 2009.
- [4] J. Valentine, J. Li, T. Zentgraf, G. Bartal, and X. Zhang, "An optical cloak made of dielectrics," *Nat Mater*, vol. 8, pp. 568-571, 07//print 2009.
- [5] T. Ergin, N. Stenger, P. Brenner, J. B. Pendry, and M. Wegener, "Three-dimensional invisibility cloak at optical wavelengths," *Science*, vol. 328, pp. 337-339, 2010.
- [6] L. H. Gabrielli, J. Cardenas, C. B. Poitras, and M. Lipson, "Silicon nanostructure cloak operating at optical frequencies," *Nat Photon*, vol. 3, pp. 461-463, 08//print 2009.
- [7] R. Liu, C. Ji, J. Mock, J. Chin, T. Cui, and D. Smith, "Broadband ground-plane cloak," *Science*, vol. 323, pp. 366-369, 2009.
- [8] M. Rahm, D. Schurig, D. A. Roberts, S. A. Cummer, D. R. Smith, and J. B. Pendry, "Design of electromagnetic cloaks and concentrators using form-invariant coordinate transformations of Maxwell's equations," *Photonics and Nanostructures-fundamentals and Applications*, vol. 6, pp. 87-95, 2008.
- [9] J. Li and J. Pendry, "Hiding under the carpet: a new strategy for cloaking," *Physical Review Letters*, vol. 101, p. 203901, 2008.
- [10] H. F. Ma and T. J. Cui, "Three-dimensional broadband and broad-angle transformation-optics lens," *Nat Commun*, vol. 1, p. 124, 11/23/online 2010.
- [11] D. A. Roberts, N. Kundtz, and D. R. Smith, "Optical lens compression via transformation optics," *Optics Express*, vol. 17, pp. 16535-16542, 2009/09/14 2009.
- [12] M. Rahm, D. A. Roberts, J. B. Pendry, and D. R. Smith, "Transformation-optical design of adaptive beam bends and beam expanders," *Optics Express*, vol. 16, pp. 11555-11567, 2008/07/21 2008.
- [13] M. Rahm, S. A. Cummer, D. Schurig, J. B. Pendry, and D. R. Smith, "Optical design of reflectionless complex media by finite embedded coordinate transformations," *Physical Review Letters*, vol. 100, p. 063903, 2008.
- [14] D.-H. Kwon and D. H. Werner, "Polarization splitter and polarization rotator designs based on transformation optics," *Optics Express*, vol. 16, pp. 18731-18738, 2008.
- [15] W. X. Jiang, T. J. Cui, Q. Cheng, J. Y. Chin, X. M. Yang, R. Liu, *et al.*, "Design of arbitrarily shaped concentrators based on conformally optical transformation of nonuniform rational B-spline surfaces," *Applied Physics Letters*, vol. 92, p. 264101, 2008.
- [16] J. Yang, M. Huang, C. Yang, Z. Xiao, and J. Peng, "Metamaterial electromagnetic concentrators with arbitrary geometries," *Optics Express*, vol. 17, pp. 19656-19661, 2009/10/26 2009.
- [17] R. C. Rumpf, C. R. Garcia, E. A. Berry, and J. H. Barton, "Finite-Difference Frequency-Domain Algorithm for Modeling Electromagnetic Scattering from General Anisotropic Objects," *Progress In Electromagnetics Research B*, vol. 61, pp. 55-67, 2014.
- [18] D. Schurig, J. Mock, B. Justice, S. A. Cummer, J. B. Pendry, A. Starr, *et al.*, "Metamaterial electromagnetic cloak at microwave frequencies," *Science*, vol. 314, pp. 977-980, 2006.
- [19] E. A. Berry, R. C. Rumpf, and J. Gutierrez, "Design and Simulation of Arbitrarily-Shaped Transformation Optic Devices Using a Simple Finite-Difference Method," *Progress in Electromagnetics Research B*, vol. TBD, 2016 submitted for publication.

- [20] N. B. Kundtz, R. Smith, and J. B. Pendry, "Electromagnetic design with transformation optics," *Proceedings of the IEEE*, vol. 99, pp. 1622-1633, 2011.
- [21] H. Chen, C. Chan, and P. Sheng, "Transformation optics and metamaterials," *Nature materials*, vol. 9, pp. 387-396, 2010.
- [22] G. L. Pedrola, *Beam Propagation Method for Design of Optical Waveguide Devices*: John Wiley & Sons, 2015.
- [23] P. J. Basser, J. Mattiello, and D. LeBihan, "MR diffusion tensor spectroscopy and imaging," *Biophysical journal*, vol. 66, p. 259, 1994.
- [24] J. F. Nye, *Physical properties of crystals: their representation by tensors and matrices*: Oxford university press, 1985.
- [25] B. Kuprel and A. Grbic, "Anisotropic inhomogeneous metamaterials using nonuniform transmission-line grids aligned with the principal axes," *Antennas and Wireless Propagation Letters, IEEE*, vol. 11, pp. 358-361, 2012.
- [26] Z.-L. Mei, J. Bai, T. M. Niu, and T.-J. Cui, "A planar focusing antenna design with the quasi-conformal mapping," *Progress In Electromagnetics Research M*, vol. 13, pp. 261-273, 2010.
- [27] J. B. Pendry, A. J. Holden, D. J. Robbins, and W. J. Stewart, "Magnetism from conductors and enhanced nonlinear phenomena," *Microwave Theory and Techniques, IEEE Transactions on*, vol. 47, pp. 2075-2084, 1999.
- [28] J. Pendry, A. Holden, W. Stewart, and I. Youngs, "Extremely low frequency plasmons in metallic mesostructures," *Physical review letters*, vol. 76, p. 4773, 1996.
- [29] D. Schurig, J. J. Mock, and D. R. Smith, "Electric-field-coupled resonators for negative permittivity metamaterials," *Applied Physics Letters*, vol. 88, p. 041109, 2006.
- [30] H. Ansys, "v15," *ANSYS Corporation Software, Pittsburgh, PA, USA*, 2014.
- [31] J. D. Jackson, *Classical Electrodynamics, 3rd ed.*: Wiley, 1999.
- [32] I. B. o. W. a. Measures., "The International System of Units (SI)," p. 112, 2006.
- [33] M. Sadiku, *Elements of electromagnetics (the oxford series in electrical and computer engineering)*: Oxford University Press, USA, 2014.
- [34] J. C. Maxwell, *A treatise on electricity and magnetism* vol. 1: Clarendon press, 1881.
- [35] A. Eroglu, *Wave propagation and radiation in gyrotropic and anisotropic media*: Springer Science & Business Media, 2010.
- [36] G. Arfken and H. Weber, *Mathematical Methods For Physicists 6th edn (New York: Academic)*, 2005.
- [37] E. Kreyszig, *Advanced engineering mathematics*: John Wiley & Sons, 1988.
- [38] R. C. Rumpf. (2016). *Transformation Electromagnetics*.
- [39] E. Kreyszig, *Differential Geometry*. New York: Dover, 1991.
- [40] A. Jeffrey, *Advanced engineering mathematics*: Academic Press, 2001.
- [41] H. Goldstein, C. P. Poole, and J. L. Safko, *Classical mechanics*, 3rd ed. San Francisco: Addison Wesley, 2002.
- [42] A. Einstein, "The foundation of the general theory of relativity," *The Principle of Relativity. Dover Books on Physics. June 1, 1952. 240 pages. 0486600815, p. 109-164*, vol. 1, pp. 109-164, 1952.
- [43] E. J. Post, *Formal structure of electromagnetics: general covariance and electromagnetics*: Courier Corporation, 1997.
- [44] J. A. Schouten, *Tensor analysis for physicists*: Courier Corporation, 1954.
- [45] A. DeBenedictis, "Integration in general relativity," *arXiv preprint physics/9802027*, 1998.
- [46] B. Schutz, *A first course in general relativity*: Cambridge university press, 2009.
- [47] S. Weinberg, *Gravitation and cosmology: principles and applications of the general theory of relativity*: John Wiley & Sons, 2004.

- [48] D. Schurig, J. Pendry, and D. R. Smith, "Calculation of material properties and ray tracing in transformation media," *Optics Express*, vol. 14, pp. 9794-9804, 2006.
- [49] P. H. Tsao, "Derivation and implications of the symmetry property of the permittivity tensor," *American Journal of Physics*, vol. 61, pp. 823-825, 1993.
- [50] D. M. Pozar, *Microwave engineering*: John Wiley & Sons, 2009.
- [51] R. C. Rumpf, "Homogenization and Parameter Retrieval," in *21st Century Electromagnetics*, ed. UTEP EM Lab, 2015.
- [52] X. Chen, T. M. Grzegorzczuk, B.-I. Wu, J. Pacheco Jr, and J. A. Kong, "Robust method to retrieve the constitutive effective parameters of metamaterials," *Physical Review E*, vol. 70, p. 016608, 2004.
- [53] Y. Hao and R. Mittra, *FDTD modeling of metamaterials: Theory and applications*: Artech house, 2008.
- [54] H.-R. Chuang and L.-C. Kuo, "3-D FDTD design analysis of a 2.4-GHz polarization-diversity printed dipole antenna with integrated balun and polarization-switching circuit for WLAN and wireless communication applications," *Microwave Theory and Techniques, IEEE Transactions on*, vol. 51, pp. 374-381, 2003.
- [55] N. Jin and Y. Rahmat-Samii, "Parallel particle swarm optimization and finite-difference time-domain (PSO/FDTD) algorithm for multiband and wide-band patch antenna designs," *Antennas and Propagation, IEEE Transactions on*, vol. 53, pp. 3459-3468, 2005.
- [56] Z. Sun and H. K. Kim, "Refractive transmission of light and beam shaping with metallic nano-optic lenses," *Applied Physics Letters*, vol. 85, pp. 642-644, 2004.
- [57] J. J. Chen, T. M. Grzegorzczuk, B.-I. Wu, and J. A. Kong, "Limitation of FDTD in simulation of a perfect lens imaging system," *Optics Express*, vol. 13, pp. 10840-10845, 2005/12/26 2005.
- [58] F. S. Roux and I. De Leon, "Planar photonic crystal gradient index lens, simulated with a finite difference time domain method," *Physical Review B*, vol. 74, p. 113103, 2006.
- [59] J. P. Verboncoeur, "Particle simulation of plasmas: review and advances," *Plasma Physics and Controlled Fusion*, vol. 47, p. A231, 2005.
- [60] G. Cerri, F. Moglie, R. Montesi, P. Russo, and E. Vecchioni, "FDTD solution of the Maxwell-Boltzmann system for electromagnetic wave propagation in a plasma," *Antennas and Propagation, IEEE Transactions on*, vol. 56, pp. 2584-2588, 2008.
- [61] J. Wang, D. Zhang, C. Liu, Y. Li, Y. Wang, H. Wang, *et al.*, "UNIPIC code for simulations of high power microwave devices," *Physics of Plasmas (1994-present)*, vol. 16, p. 033108, 2009.
- [62] S. C. Chapra and R. P. Canale, *Numerical methods for engineers* vol. 2: McGraw-Hill, 2012.
- [63] R. C. Rumpf, Ed., *3D FDTD (Electromagnetic Analysis Using Finite-Difference Time-Domain)*. UTEP EM Lab, 2014, p. ^pp. Pages.
- [64] Z. S. Sacks, D. M. Kingsland, R. Lee, and J.-F. Lee, "A perfectly matched anisotropic absorber for use as an absorbing boundary condition," *Antennas and Propagation, IEEE Transactions on*, vol. 43, pp. 1460-1463, 1995.
- [65] J.-P. Bérenger, "Perfectly matched layer (PML) for computational electromagnetics," *Synthesis Lectures on Computational Electromagnetics*, vol. 2, pp. 1-117, 2007.
- [66] J.-P. Berenger, "A perfectly matched layer for the absorption of electromagnetic waves," *Journal of computational physics*, vol. 114, pp. 185-200, 1994.
- [67] R. C. Rumpf, Ed., *The Perfectly Matched Layer (Electromagnetic Analysis Using Finite-Difference Time-Domain)*. UTEP EM Lab, 2014, p. ^pp. Pages.
- [68] K. S. Yee, "Numerical solution of initial boundary value problems involving Maxwell's equations in isotropic media," *IEEE Trans. Antennas Propag*, vol. 14, pp. 302-307, 1966.
- [69] R. C. Rumpf. (2016). *Formulation of 1D FDTD*.
- [70] A. Taflove and S. C. Hagness, *Computational electrodynamics*: Artech house publishers, 2000.

- [71] R. C. Rumpf, "Simple implementation of arbitrarily shaped total-field/scattered-field regions in finite-difference frequency-domain," *Progress In Electromagnetics Research B*, vol. 36, pp. 221-248, 2012.
- [72] S. Mazumder, *Numerical Methods for Partial Differential Equations: Finite Difference and Finite Volume Methods*: Elsevier Science, 2015.
- [73] R. C. Rumpf. (2015). *Finite Difference Method*.
- [74] T. A. Davis, "Algorithm 832: UMFPACK V4. 3---an unsymmetric-pattern multifrontal method," *ACM Transactions on Mathematical Software (TOMS)*, vol. 30, pp. 196-199, 2004.
- [75] C. C. Paige and M. A. Saunders, "Solution of sparse indefinite systems of linear equations," *SIAM journal on numerical analysis*, vol. 12, pp. 617-629, 1975.
- [76] J. Hu, X. Zhou, and G. Hu, "Design method for electromagnetic cloak with arbitrary shapes based on Laplace's equation," *Optics express*, vol. 17, pp. 1308-1320, 2009.
- [77] Z. Chang, X. Zhou, J. Hu, and G. Hu, "Design method for quasi-isotropic transformation materials based on inverse Laplace's equation with sliding boundaries," *Optics express*, vol. 18, pp. 6089-6096, 2010.
- [78] N. I. Landy and W. J. Padilla, "Guiding light with conformal transformations," *Optics express*, vol. 17, pp. 14872-14879, 2009.
- [79] J.-J. Ma, X.-Y. Cao, K.-M. Yu, and T. Liu, "Determination the material parameters for arbitrary cloak based on Poisson's equation," *Progress In Electromagnetics Research M*, vol. 9, pp. 177-184, 2009.
- [80] X. Chen, Y. Fu, and N. Yuan, "Invisible cloak design with controlled constitutive parameters and arbitrary shaped boundaries through Helmholtz's equation," *Optics Express*, vol. 17, pp. 3581-3586, 2009/03/02 2009.
- [81] R. C. Rumpf and J. Pazos, "Synthesis of spatially variant lattices," *Optics express*, vol. 20, pp. 15263-15274, 2012.
- [82] G. D. Smith, *Numerical solution of partial differential equations: finite difference methods*: Oxford university press, 1985.
- [83] R. J. LeVeque, "Finite difference methods for differential equations," *Draft version for use in AMath*, vol. 585, 1998.
- [84] G. H. Golub and C. F. Van Loan, *Matrix computations* vol. 3: JHU Press, 2012.
- [85] H. Johnson and C. S. Burrus, "On the structure of efficient DFT algorithms," *Acoustics, Speech and Signal Processing, IEEE Transactions on*, vol. 33, pp. 248-254, 1985.
- [86] A. Iserles, *A first course in the numerical analysis of differential equations*: Cambridge University Press, 2009.
- [87] M. A. Morgan, *Finite element and finite difference methods in electromagnetic scattering*: Elsevier, 2013.
- [88] P. Luong, "A mathematical coastal ocean circulation system with breaking waves and numerical grid generation," *Applied Mathematical Modelling*, vol. 21, pp. 633-641, 1997.
- [89] P. R. Eiseman, "Grid generation for fluid mechanics computations," *Annual Review of Fluid Mechanics*, vol. 17, pp. 487-522, 1985.
- [90] J. F. Thompson, Z. U. Warsi, and C. W. Mastin, *Numerical grid generation: foundations and applications* vol. 45: North-holland Amsterdam, 1985.
- [91] E. Sanmiguel-Rojas, J. Ortega-Casanova, C. del Pino, and R. Fernandez-Feria, "A Cartesian grid finite-difference method for 2D incompressible viscous flows in irregular geometries," *Journal of Computational Physics*, vol. 204, pp. 302-318, 2005.
- [92] V. Akcelik, B. Jaramaz, and O. Ghattas, "Nearly orthogonal two-dimensional grid generation with aspect ratio control," *Journal of Computational Physics*, vol. 171, pp. 805-821, 2001.

- [93] M. P. Hobson, G. P. Efstathiou, and A. N. Lasenby, *General relativity: an introduction for physicists*: Cambridge University Press, 2006.
- [94] V. Liseikin, "Coordinate Transformations," in *Grid Generation Methods*, ed: Springer Netherlands, 2010, pp. 31-66.
- [95] R. C. Rumpf. (2015). *Preliminary Topics*.
- [96] D. J. Griffiths and R. College, *Introduction to electrodynamics* vol. 3: prentice Hall Upper Saddle River, NJ, 1999.
- [97] R. C. Rumpf, "Engineering the Dispersion and Anisotropy of Periodic Electromagnetic Structures," *Solid State Physics*, 2015.
- [98] J. L. Digaum, J. J. Pazos, J. Chiles, J. D'Archangel, G. Padilla, A. Tatulian, *et al.*, "Tight control of light beams in photonic crystals with spatially-variant lattice orientation," *Optics express*, vol. 22, pp. 25788-25804, 2014.
- [99] R. C. Rumpf, J. Pazos, C. R. Garcia, L. Ochoa, and R. Wicker, "3D printed lattices with spatially variant self-collimation," *Progress in Electromagnetics Research*, vol. 139, pp. 1-14, 2013.
- [100] R. C. Rumpf and J. J. Pazos, "Optimization of planar self-collimating photonic crystals," *JOSA A*, vol. 30, pp. 1297-1304, 2013.
- [101] R. C. Rumpf, J. J. Pazos, J. L. Digaum, and S. M. Kuebler, "Spatially variant periodic structures in electromagnetics," *Phil. Trans. R. Soc. A*, vol. 373, p. 20140359, 2015.
- [102] R. C. Rumpf, C. R. Garcia, H. H. Tsang, J. E. Padilla, and M. D. Irwin, "Electromagnetic isolation of a microstrip by embedding in a spatially variant anisotropic metamaterial," *Progress In Electromagnetics Research*, vol. 142, pp. 243-260, 2013.
- [103] G. Williams, "Overdetermined systems of linear equations," *American Mathematical Monthly*, pp. 511-513, 1990.
- [104] R. C. Rumpf, Ed., *Maxwell's Equations in Fourier Space* (Computational Electromagnetics. UTEP EM Lab, 2015, p.^pp. Pages.
- [105] E. W. Weisstein, "Gibbs phenomenon," 2003.
- [106] R. P. Feynman, R. B. Leighton, and M. L. Sands, *The Feynman lectures on physics*. Reading, Mass.: Addison-Wesley Pub. Co., 1963.
- [107] R. C. Rumpf, Ed., *Electromagnetic Properties of Materials - Part 2: Nonlinear and Anisotropic Materials* (21st Century Electromagnetics. UTEP EM Lab, 2015, p.^pp. Pages.
- [108] T. A. Lam, D. C. Vier, J. A. Nielsen, C. G. Parazzoli, and M. H. Tanielian, "Steering phased array antenna beams to the horizon using a buckyball NIM lens," *Proceedings of the IEEE*, vol. 99, pp. 1755-1767, 2011.
- [109] T. Greville, "Some applications of the pseudoinverse of a matrix," *SIAM review*, vol. 2, pp. 15-22, 1960.
- [110] R. Rumpf. (2015). *Introduction to CEM*.
- [111] C. Nieter and J. R. Cary, "VORPAL: a versatile plasma simulation code," *Journal of Computational Physics*, vol. 196, pp. 448-473, 2004.

Vita

Eric Alan Berry graduated with a bachelor's degree in 2008 from the University of Texas at El Paso (UTEP) in electrical engineering. In 2012 he started the doctoral program in the department of electrical and computer engineering at UTEP. In December 2016, he received his doctorate in electrical and computer engineering.

In 2008 he became the lead facility engineer at the *High Power Electromagnetic* (HPEM) facilities at *White Sands Missile Range* (WSMR). As the lead facility engineer he was responsible for operation and maintenance of the *High Altitude Electromagnetic Pulse* (HEMP), *High Power Microwave* (HPM), and *Near Strike Lightning* (NSL) facilities. He has designed a data acquisition system to acquire data using oscilloscopes, network analyzers, signal generators, and spectrum analyzers to perform measurements at the HPEM facilities. In 2016 he became an experimental physicist with XL Scientific, LLC. in Albuquerque, NM. His primary role is neutron detection instrumentation for a *Dense Plasma Focus* (DPF) machine constructed for the *Directed Energy Test and Evaluation Science and Technology* (DET S&T) program for the United States Army.

Permanent address: 904 Desert Sage
Anthony TX, 79821

This thesis/dissertation was typed by Eric Alan Berry